AFRL-RB-WP-TR-2011-3025

GROUND TEST AND COMPUTATION OF BOUNDARY LAYER TRANSITION ON THE HYPERSONIC INTERNATIONAL FLIGHT RESEARCH AND EXPERIMENTATION (HIFiRE)-5 VEHICLE

Roger Kimmel, David Adamczak, and Ryan Gosse

High-speed Aerodynamic Configuration Branch
Aeronautical Sciences Division

Karen Berger and Shann Rufer

NASA LaRC

FEBRUARY 2011
Final Report

STINFO COPY

AIR FORCE RESEARCH LABORATORY
AIR VEHICLES DIRECTORATE
WRIGHT-PATTERSON AIR FORCE BASE, OH 45433-7542
AIR FORCE MATERIEL COMMAND
UNITED STATES AIR FORCE

NOTICE AND SIGNATURE PAGE

*//Signature//   //Signature//

ROGER L. KIMMEL   JAMES H. MILLER
Principal Aerospace Engineer   Chief
High-speed Aerodynamic   High-speed Aerodynamic
  Configuration Branch   Configuration Branch

//Signature//

MICHAEL ZIEGLER
Chief
Aeronautical Sciences Division
Air Vehicles Directorate

REPORT DOCUMENTATION PAGE

*Form Approved
OMB No. 0704-0188*

1. REPORT DATE *(DD-MM-YY)*	2. REPORT TYPE	3. DATES COVERED *(From - To)*
February 2011	Final	01 December 2006 – 01 December 2010

4. TITLE AND SUBTITLE

GROUND TEST AND COMPUTATION OF BOUNDARY LAYER TRANSITION ON THE HYPERSONIC INTERNATIONAL FLIGHT RESEARCH AND EXPERIMENTATION (HIFiRE)-5 VEHICLE

5a. CONTRACT NUMBER
In-house

5b. GRANT NUMBER

5c. PROGRAM ELEMENT NUMBER
61102F

6. AUTHOR(S)

Roger Kimmel, David Adamczak, and Ryan Gosse (AFRL/RBAH)
Karen Berger and Shann Rufer (NASA LaRC)

5d. PROJECT NUMBER
2307

5e. TASK NUMBER

5f. WORK UNIT NUMBER
A0C80B

7. PERFORMING ORGANIZATION NAME(S) AND ADDRESS(ES)

High-speed Aerodynamic Configuration Branch (AFRL/RBAH)   NASA LaRC
Aeronautical Sciences Division
Air Force Research Laboratory, Air Vehicles Directorate
Wright-Patterson Air Force Base, OH 45433-7542
Air Force Materiel Command, United States Air Force

8. PERFORMING ORGANIZATION REPORT NUMBER
AFRL-RB-WP-TR-2011-3025

9. SPONSORING/MONITORING AGENCY NAME(S) AND ADDRESS(ES)

Air Force Research Laboratory
Air Vehicles Directorate
Wright-Patterson Air Force Base, OH 45433-7542
Air Force Materiel Command
United States Air Force

10. SPONSORING/MONITORING AGENCY ACRONYM(S)
AFRL/RBAH

11. SPONSORING/MONITORING AGENCY REPORT NUMBER(S)
AFRL-RB-WP-TR-2011-3025

12. DISTRIBUTION/AVAILABILITY STATEMENT
Approved for public release; distribution unlimited.

13. SUPPLEMENTARY NOTES
PAO Case Number: 88ABW-2011-2036; Clearance Date: 07 April 2011.

Report contains color.

14. ABSTRACT

The HIFiRE Flight 5 payload was assessed in the NASA LaRC 20-Inch Mach 6 Air Tunnel. The primary objectives were to determine the boundary layer transition characteristics and the effectiveness trips. Boundary layer profiles were extracted from Navier-Stokes calculations of the flow field, and were used to assess trip heights in terms of typical trip correlating parameters. Leading-edge roughness was well-correlated with the R-bar-star parameter. This correlation was used to extrapolate wind tunnel data to full-scale flight conditions. Boundary layer transition was also studied using Parabolized Stability Equation (PSE) analysis. The stability analysis was conducted on the two symmetry planes of the vehicle. The leading edge planes are expected to follow second mode instability growth. The centerline cases experienced a more complicated growth that was mainly driven by second mode, but also showed higher modes. In particular for the lowest altitude case, the higher modes showed to contribute to the maximum N factor growth. This was caused by the complex boundary layer profile that was induced by a pair of vortices along the centerline of the vehicle.

15. SUBJECT TERMS
boundary layer transition, hypersonic, flight test

16. SECURITY CLASSIFICATION OF:

a. REPORT	b. ABSTRACT	c. THIS PAGE	17. LIMITATION OF ABSTRACT:	18. NUMBER OF PAGES	19a. NAME OF RESPONSIBLE PERSON (Monitor)
Unclassified	Unclassified	Unclassified	SAR	96	Roger L. Kimmel

19b. TELEPHONE NUMBER *(Include Area Code)*
N/A

Standard Form 298 (Rev. 8-98)
Prescribed by ANSI Std. Z39-18

TABLE OF CONTENTS

Section

List of Figures

List of Tables

Acknowledgments

1. Summary

This report summarizes testing and analysis of the HIFiRE Flight 5 configuration. Engineering analysis was performed to determine the vehicle aerodynamic stability and the payload thermal environment. Ground testing measured the overall boundary-layer transition pattern and heat transfer on the vehicle. Special attention was paid to the effects of roughness on transition, so that roughness tolerances could be specified to the payload manufacturers. Finally, CFD and stability analysis were performed to aid in extrapolating wind tunnel transition results to free flight conditions.

Results show that the proposed configuration is suitable for testing transition on a three-dimensional body. Transition is predicted to occur within the test window, and a design has been developed that will allow the vehicle to be manufactured within prescribed roughness tolerances. Although the payload is not axially symmetric and thus has different pitch-plane and yaw-plane aerodynamics, the entire vehicle is stable in both planes.

The HIFiRE Flight 5 payload was assessed in the Langley Research Center's 20-Inch Mach 6 Air Tunnel. The primary objectives of this test were to determine the boundary layer transition characteristics as well as the effectiveness of 2-D strip trips to simulate the joint between the nosecap and body of the vehicle and 3-D diamond shaped trips, to simulate the fasteners on a closeout panel that will be on one side of the flight vehicle. In order to accomplish this, global heat transfer images were obtained for unit Reynolds numbers of 1.1×10^6/ft to 7.0×10^6/ft, angles of attack of -4 to +4 deg and side slip angles of -4 to +4 deg, which were conditions pertinent to the flight. Heating data demonstrated that the vehicle can be expected to exhibit natural boundary layer transition on the windside surface in the absence of boundary layer trips. The primary driver of the transition at 0 deg AoA appears to be cross-flow boundary layer transition, but windward centerline transition becomes more prominent as the angle of attack is increased. On the windside surface, both the 2D and 3D trips were utilized. None of the trips used were able to induce boundary layer transition along the centerline of the windside, though some did cause a local disturbance before the flow returned to the untripped heating levels. Off centerline, the 2D trips were able to significantly influence the leading edges of the vehicle but had little effect on the rest of the vehicle. The 3D trips were much more effective at causing localized turbulent heating, especially as they were moved away from the centerline. The localized, disturbed flow resulting from the 3D trips did not spread around the leading edges of the vehicle and thus attachment hardware on the closeout side of the flight vehicle will not influence the heating on the smooth, "clean" side of the vehicle.

The heating along the leading edge was investigated and the effectiveness of both the 2D and 3D trips were determined. The natural boundary layer transition unit Reynolds number was determined and it was found that the 3D trips were much more effective on the leading edge. Because the most likely cause of premature transition in this region is from the 2D trip associated with the joint between the nose and the body, much more effort was put into determining the allowable range of trip heights. For the 2D trips at a unit Reynolds number of 5.3×10^6/ft (where natural transition occurred), the critical trip height was between 0.0090 and 0.0115 in. and for 3.0×10^6/ft (to match the Purdue Mach 6 Quiet Tunnel result) 0.0150 and 0.0185 in. The sideslip angle greatly influenced the transition onset location and increases in the angle moved the transition forward on the vehicle.

Boundary layer profiles were extracted from Navier-Stokes calculations of the flow field. These were used to assess trip heights in terms of typical trip correlating parameters. The effect of leading-edge roughness on transition is well-correlated with the $\overline{R}^*$ correlation. This correlation is used to extrapolate wind tunnel data to full-scale flight conditions and obtain allowable leading-edge roughness tolerances. Leading-edge roughness tolerances are stringent but can be achieved using a clamshell design with a one-piece leading edge.

Boundary layer transition on the HIFiRE 5 flight vehicle was studied using Parabolized Stability Equation (PSE) analysis. Four trajectory points were selected to cover the range of the flight where transition is expected to occur on the vehicle. In order to calculate the PSE, a mean flow solution was generated using a finite-volume Navier-Stokes solver. The stability analysis was then conducted on the two symmetry planes of the vehicle. It was found that the leading edge planes are expected to follow second mode instability growth. The centerline cases experienced a much more complicated growth that was mainly driven by second mode, but also showed higher growth modes. In particular for the lowest altitude case, the higher modes showed to contribute to the maximum N factor growth. This was caused by the complex boundary layer profile that was induced by a pair of vortices along the centerline of the vehicle.

2. Introduction

The Hypersonic International Flight Research Experimentation (HIFiRE) program is a hypersonic flight test program executed by the Air Force Research Laboratory (AFRL) and the Australian Defence Science and Technology Organization (DSTO).[1,2] Its purpose is to develop and validate technologies critical to next generation hypersonic aerospace systems. Candidate technology areas include, but are not limited to, propulsion, propulsion-airframe integration, aerodynamics and aerothermodynamics, high temperature materials and structures, thermal management strategies, guidance, navigation, and control, sensors, and components such as munitions, submunitions and avionics. The HIFiRE program consists of extensive ground tests and computation focused on specific hypersonic flight technologies. Each technology program culminates in a flight test. HIFiRE-5 is the second of two flights in the HIFiRE manifest focused on boundary layer transition. The HIFiRE-1 program created an extensive knowledge base regarding transition on axisymmetric bodies that has been summarized in numerous prior publications.[3,4,5,6,7,8,9,10,11,12,13,14] The HIFiRE-5 flight is devoted to measuring transition on a three-dimensional (3D) body.

Boundary-layer transition is an important parameter in hypersonic vehicle design. Transition impacts vehicle design primarily through aerodynamic heating but also skin friction drag and affects pressure drag, engine performance, and aerodynamic control.[15] Estimates for the National Aerospace Plane (NASP)[16] showed that the payload-to-gross-weight ratio would nearly double if the vehicle boundary-layer were fully laminar, compared to fully turbulent.

Boundary layer transition predictions on hypersonic lifting bodies present a challenge because several modes of transition mechanisms are present. During the mid-1990s, several researchers investigated transition phenomena on elliptic cones.[17,18,19,20,21,22,23,24] The elliptic cone embodies much of the transition phenomena seen on hypersonic glide vehicles. These phenomena include traveling first and second-mode waves, stationary and traveling cross-flow waves[25] and leading edge attachment line flows.[26] Attachment line flows contain no unique instability modes, but are characterized by thin boundary layers that are sensitive to roughness, but otherwise are generally stable. Figure 1 shows a cone with 2:1 elliptic cross-section in Arnold Engineering Development Center von Karman Facility Tunnel B. The model is essentially identical to the HFiRE-5 body, except that it has a nominally sharp tip. The cone half-angle in the minor axis is 7 deg. Nominal freestream Mach number for this test was 8, and the ratio of wall-to-stagnation temperature T_w/T_0=0.42.
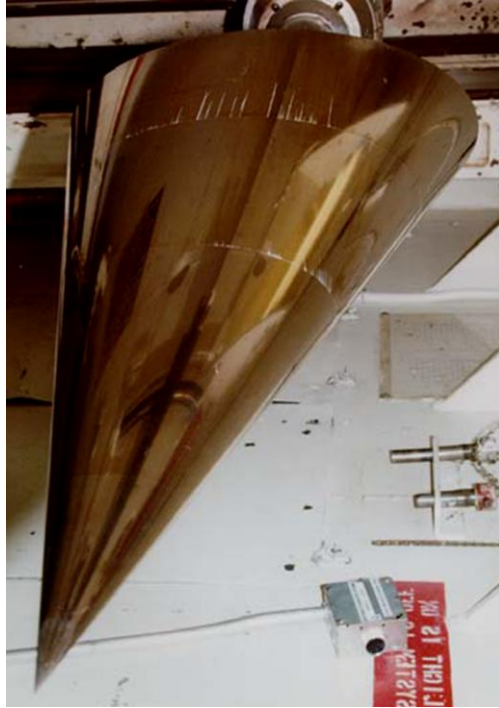
Figure 1 2:1 elliptic cone

Figure 2 shows measured heat transfer rate contours and the transition front for a shape such as the HIFiRE 5 vehicle. The plot is a composite of transition measurements made at several freestream unit Reynolds numbers and illustrates the very different stability characteristics between the centerline and leading edge. The centerline possesses a highly-inflected, unstable profile due to boundary layer fluid washing in from the higher pressure leading edges. Its transition Reynolds number is on the order of $5x10^5$ and there are no well-defined crossflow side lobes. The leading edge, however, exhibits a transition Reynolds number near $6x10^6$, or an order of magnitude larger. As a point of reference, transition on a 7-deg half-angle sharp, axisymmetric cone under the same conditions occurs at approximately $2.6x10^6$.[27]
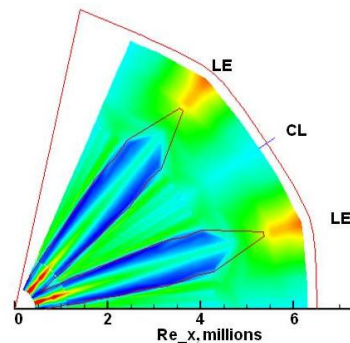
Figure 2 Heat transfer contours on unwrapped surface of elliptic cone. Red line indicates transition front.

Extended hypersonic flight with lifting configurations requires improved understanding and prediction of 3D transition. Transition on 3D configurations embodies several phenomena not encountered on axisymmetric configurations like HIFiRE-1, including leading-edge or attachment-line transition and crossflow instabilities (including crossflow interactions with other instability mechanisms shared with axisymmetric flow configurations such as first and second mode instabilities). Very limited hypersonic flight data exist for either phenomena.[28] The need for a better understanding of 3D transition motivates the HIFiRE-5 experiment. This report describes how the HIFIRE-5 overall vehicle configuration has been designed, including booster, trajectory, aerodynamic stability and aeroshell outer moldline design to meet requirements to measure 3D transition.

3. Vehicle and Trajectory

3.1. Vehicle Description

The HIFiRE-5 configuration consists of a payload mounted atop an S-30 first stage[29] and Improved Orion[30] second stage motor, shown in Figure 3. The term "payload" refers to all test equipment mounted to the second stage booster, including the instrumented test article and additional control and support sections situated between the test article and the second stage motor. The test article consists of a blunt-nosed elliptic cone of 2:1 ellipticity, 0.86 meters in length. The payload does not separate from the second-stage Orion, and remains attached to it throughout the reentry. The vehicle is spin-stabilized. Cant-angle on the first and second-stage fins causes the vehicle to spin passively. Because of this, the payload is rolling throughout the entire trajectory.

The elliptic cone configuration was chosen as the test-article geometry based on extensive previous testing and analysis on elliptic cones.[17,18,19,20,21,22,23,24,25] This prior work[17,18,19] demonstrated that the 2:1 elliptic cone would generate significant crossflow instability at the flight conditions and potentially exhibit leading-edge transition. The 2:1 elliptic cone configuration also possesses ample internal volume for sensors and instrumentation. In order to exploit this prior body of work and expedite configuration development, the 2:1 elliptical geometry was selected as the HIFiRE-5 test article. Figure 4 illustrates the elliptic cone geometry and coordinate system.

Figure 5 presents a dimensioned drawing of the payload, including nosetip detail. The half-angle of the elliptic cone test article in the minor axis (x-y) plane is seven degrees, and 13.797 degrees in the major axis. The nose tip cross-section in the minor axis is a 2.5 mm radius circular arc, tangent to the cone ray describing the minor axis, and retains a 2:1 elliptical cross-section to the stagnation point. The elliptic cone major axis diameter is 431.8 mm at the base, and the cone overhangs the 355.6 mm diameter second-stage booster in the yaw (x-z) plane. A section with minimal instrumentation blends the elliptical cone cross-section into the circular booster cross section. Small canards for material tests may be incorporated on the transition section. A cylindrical can containing GPS, antennas and other equipment resides between the transition section and the Orion booster. The vehicle is stable in yaw and pitch planes as described below, and no shroud is currently envisioned.

Figure 3 HIFiRE-5 stack.

Figure 4 Elliptic cone geometry and coordinate system.
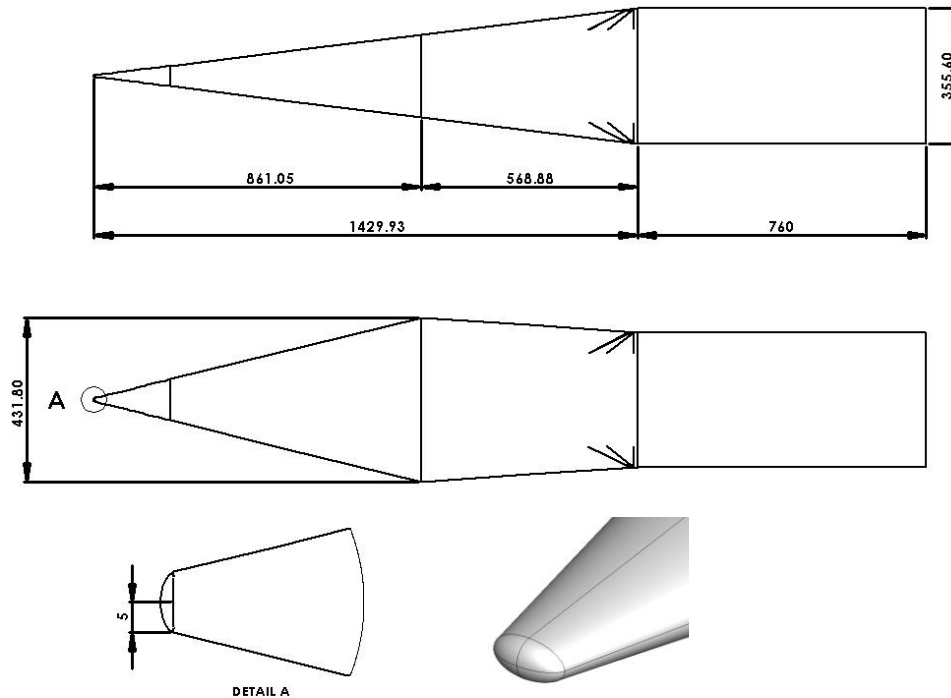
Figure 5 HIFiRE-5 payload, including nosetip detail (dimensions in mm).

3.2.   Vehicle Aerodynamics

The advantage of designing the HIFiRE 5 without a shroud over the payload was that it simplifies the payload mechanical design, reduces weight and removes the risk of shroud-deployment failure. Flight without a shroud however incurs some risk to the payload through ascent heating and exposure of the test article sensors.   The HIFiRE-0 risk-reduction flight demonstrated that flight-control sensors would withstand ascent heating[31] on the Terrier / Improved Orion stack[30] used for HIFiRE-0 and -1. Since the ascent characteristics of the S-30 first-stage booster are much more benign than the Terrier first-stage used on HIFiRE-0 and -1, thermal loads on instrumentation during ascent should be acceptable. Although the HIFiRE-5 test article produces no lift at zero angle-of-attack, the non-axisymmetric test article possesses different pitch-plane and yaw-plane aerodynamics, which was a source of concern. Because of this, the HIFiRE-5 aerodynamics were examined in detail using Missile Datcom semi-empirical methods[32,33] and the CART3D Euler solver.[34] Figure 6 illustrates the asymmetric aerodynamics of the reentry configuration. Aerodynamics were obtained with Missile Datcom, using the aerodynamics and mass properties of the reentry stack consisting of the burnt-out second stage and payload at Mach 7. Figure 6 shows the effect of roll angle on pitching moment for the two extremes, 0-deg (least stable) and 90-deg (most stable). Although windward-side pressures are less on the 0-deg roll case, the 0-deg case is less stable than the 90-deg case due to the greater lifting area it introduces at the nose.

Figure 7 compares pitching moments obtained using Datcom and CART3D for the reentry configuration. Two center-of-gravity (CG) locations are considered for each method, an aft CG

Approved for public release; distribution unlimited.

(x=3.426 m) and a more forward CG (x=2.837 m) obtained by ballasting the vehicle to make it neutrally stable at Mach 10, based on the Datcom-calculated center-of-pressure. These CGs are representative only, since the final CG will vary as the design evolves. These results are for the 0-deg (least stable) roll angle. Datcom indicates a less-stable vehicle than does CART3D over the Mach number range examined, $2 < M < 8$. Both methods indicate reduced stability as Mach number increases. Although the Euler analysis is expected to be more accurate than Datcom, which is semi-empirical, the Datcom results are more conservative and were thus used to analyze the vehicle stability. The final HIFiRE-5 design incorporates 33 kg of ballast to retain a 1.5 caliber static margin throughout ascent, based on Datcom estimates. Based on observed differences between CART3D and Datcom results, the actual static margin is expected to be 1.8-2 calibers at 0-deg roll angle. Since this is based on the least-stable roll configuration, it represents a minimum expected stability.
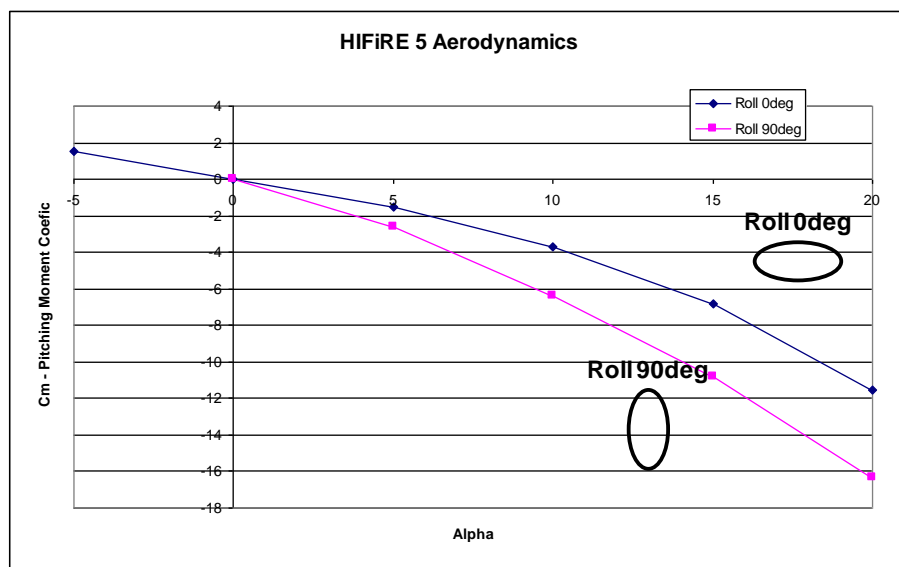
Figure 6 Pitching moment as a function of angle of attack and roll attitude.
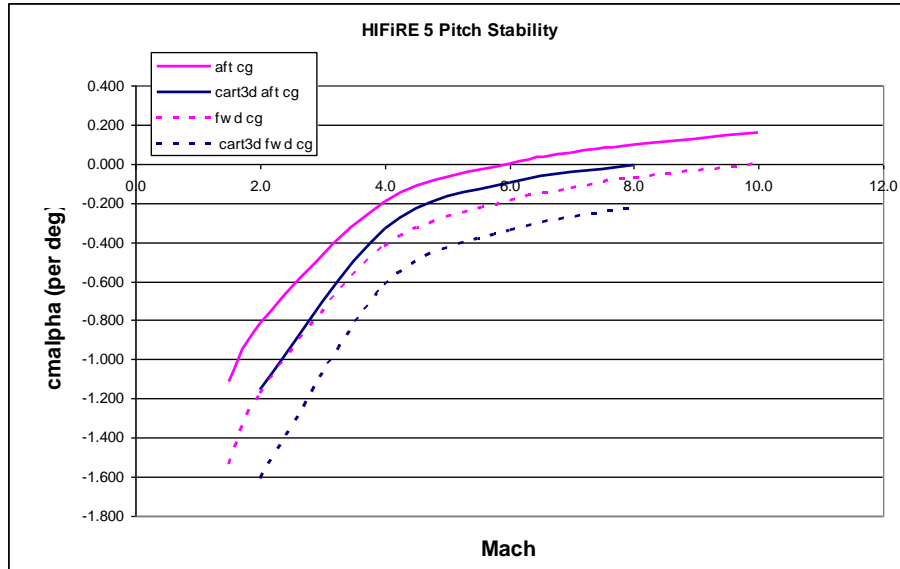
Figure 7 Comparison of predicted pitch moments for 0-deg roll angle using Datcom (purple lines) and CART3D (blue lines)

The HIFiRE-5 trajectory was simulated with the vehicle aerodynamics obtained from the Euler solver CART3D. Figure 8 illustrates the nominal trajectory for a launcher quadrant elevation (angle above horizon) of 81.65 deg. The high launch angle serves two purposes. First it constrains the range of the missile. Second, it limits the reentry exposure and heating of the test article. In this nominal trajectory, the S-30 / Orion stack boosts the test article to approximately 266 km, with a peak reentry Mach number of 7.4. The predicted second-stage impact is approximately 350 km downrange of the launcher. Total endoatmospheric flight time is less than eighty seconds.

The high launch angle also aids in transition measurement. Successful transition measurement requires that the transition occur on the instrumented region of the test article at some point during the trajectory. The high launch angle trajectories used in HIFiRE-1 and 5 are ideal for this since it creates a flight environment analogous to a wind tunnel Reynolds number sweep. Mach number varies less than +/- 0.15 during the period of expected transitional flow over the test article during reentry. Figure 9, which illustrates the Reynolds number and Mach number profiles during ascent and descent, shows the Reynolds number sweep that occurs during reentry.

10
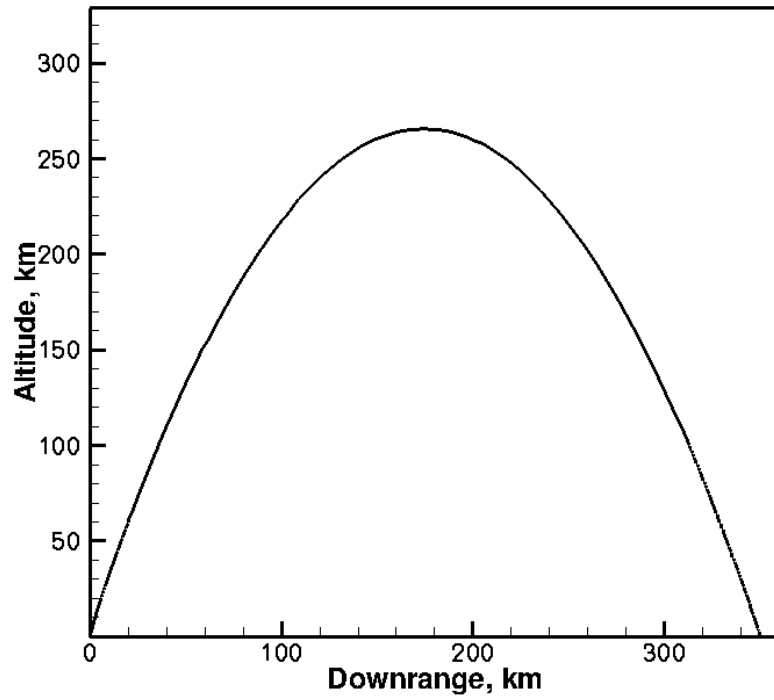
Figure 8 HIFiRE 5 trajectory
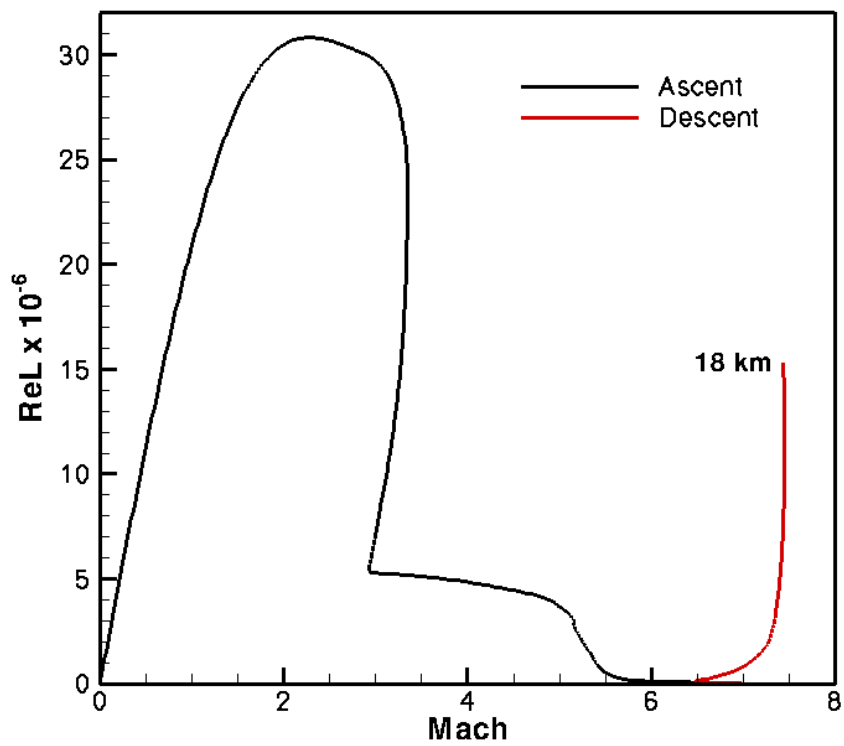
Figure 9 HIFiRE-5 Reynolds number and Mach profile

The entire reentry vehicle (payload plus second stage) is aerodynamically stable and will self-orient into a nose-first attitude during reentry upon achieving sufficient dynamic pressure, regardless of any control inputs. In general, the missile will be spinning and precessing (coning) throughout flight. In the absence of any control input, the payload will reenter the atmosphere nose high relative to the flight-path vector. When the dynamic pressure is high enough, the vehicle will orient into a low AoA attitude since it is statically stable. Figure 10 illustrates this situation. The top graph shows the flight-path angle of the vehicle center of mass (gammar, relative to the horizon) and total pitch angle (pitr, orientation of the vehicle longitudinal axis relative to the horizon). This simulation is for a case in which the mean pitch angle is 75-deg, and the coning half angle is 6-deg. Asymmetric aerodynamics due to the test article geometry are taken into account. Apogee is at 270 seconds. The vehicle's motion continues unimpeded until approximately 460 seconds, when rapidly increasing air density causes the pitch angle to rather suddenly align approximately with the flight path angle. Pitch oscillations increase and then begin to damp. Note that the flight path angle varies continuously due to the ballistic nature of the trajectory. The bottom graph of Figure 10 details pitch and yaw angle during the last 13 seconds of the trajectory and illustrates this damping. Since the vehicle is spinning, pitch and yaw are 90-deg out of phase.
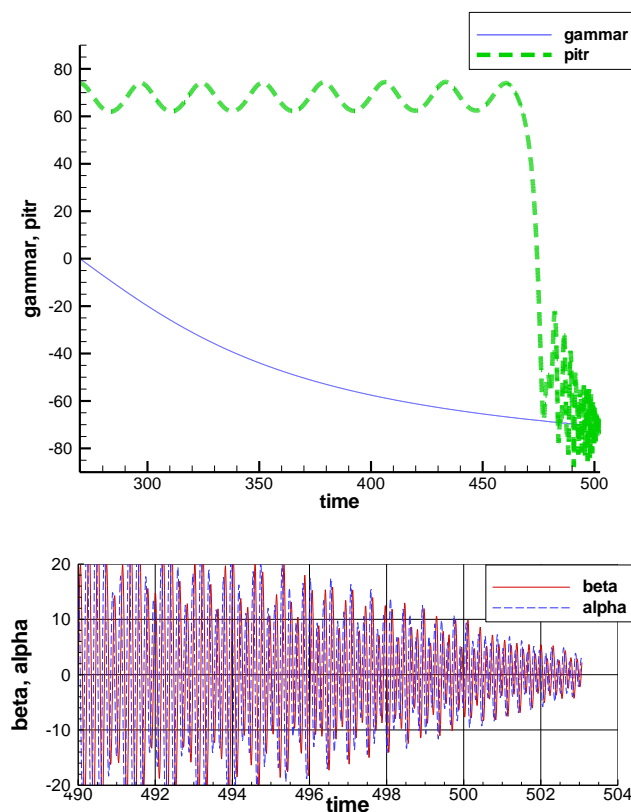
Figure 10 Flight-path angle and total pitch angle (top), and yaw and pitch (bottom) for reentry with no control inputs.

Approved for public release; distribution unlimited.

In order to achieve a low angle of attack and minimize oscillations within the atmosphere during reentry, a nitrogen-jet reaction control system will align the vehicle during exoatmospheric flight, so the vehicle longitudinal axis is approximately coincident with the reentry flight path vector, minimizing the coning angle. In the HIFiRE-0 flight, this system was capable of aligning the vehicle to within 5.1 deg of the flight path angle and zero coning angle.[31] The maximum allowable angle of attack when transitional flow occurs on the test article sets requirements on the pointing accuracy of the exoatmospheric cold-gas thruster maneuver. The primary variables of concern are the residual coning (or precession) angle and the pitch angle at the end of the cold-gas thruster maneuver. In order to determine the pitch and coning angle required to minimize total AoA during testing, residual pitch angle and coning angle were varied parametrically over a range of expected values, and used as initial conditions for 6DOF simulations.

Numerous 6DOF simulations showed that best results were obtained at zero coning angle, and that the optimum pitch angle was near the flight path angle that occurs near the atmospheric interface (approximately –70-deg at 460 seconds for this trajectory). Figure 11 shows an example for a pitch angle of -70-deg and a coning angle of half-cone two degrees. Since the pitch angle is near the flight path angle at atmospheric interface, and the cone angle is small, AoA oscillations are small and have damped to less than +/- 1 deg by 490 seconds. A 6-DOF simulation for pitch angle of -70-deg but 6-deg coning half-angle, yielded AoA oscillations of +/- 2 deg. These results are in contrast to expected AoA oscillations greater than 20-deg for no thruster control (Figure 10). It should be noted that even for the case of no control inputs, oscillations have damped to less than +/- 5 deg by 502 seconds.
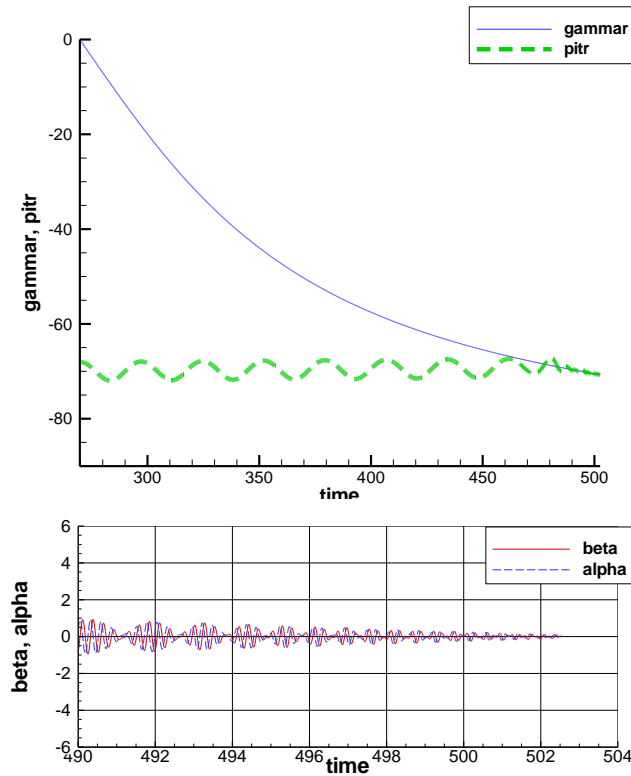
Figure 11 Flight-path angle and total pitch angle (top), and yaw and pitch (bottom) for reentry with pitch angle -70 deg and 2-deg coning half-angle.

3.3.   Thermal Analysis

The design tools MINIVER[35], HEAT-TK[36] and TOPAZ3D were used to develop the vehicle heat transfer and temperature profiles. MINIVER employs analytical and semi-empirical engineering methods to determine heat transfer throughout the trajectory. TOPAZ3D is a three-dimensional, finite-element solver for unsteady conduction problems. TOPAZ3D was used to provide higher fidelity results for the conduction analysis rather than MINIVER, which contains a 1D conduction solver. The MINIVER conduction analyses provided spot checks of the TOPAZ3D results where lateral conduction was not significant. Detailed thermal analysis was performed by porting the MINIVER heat transfer coefficients to TOPAZ3D, and then using TOPAZ3D to determine the payload temperature field as a function of time using a convection boundary condition on the vehicle exterior and adiabatic interior wall. Boundary-layer transition was taken into account using Re_θ/M_e correlation, with Re_θ/M_e =150 corresponding to the beginning of transition, and Re_θ/M_e =212 corresponding to the end of transition. The Re_θ/M_e correlation is well-known for having a large uncertainty, even for simple axisymmetric configurations (see for example Ref. 5), but it provides a simple means to account for transition during the preliminary design of HIFiRE-5, since thermal margins are not critical for this vehicle.

Figure 12 shows outer surface temperature at six x-stations on the ϕ=0 plane for HIFiRE-5 as a function of time during ascent. This temperature profile was calculated for a TZM nosetip 80 mm long followed by two steel frusta (150 mm total length) to insulate the body from the

nosetip, all followed by a 20 mm thick aluminum shell. Temperatures at the stagnation point and the bluntness / frustum juncture at 2.5 mm peak initially at first-stage burnout at about 22 seconds, then drop as heat is conducted away by the rest of the tip during coast phase. After the second stage ignites at approximately 30 seconds, the stagnation point temperature climbs to its ascent peak of approximately 750 K. Temperature at the end of the TZM nosetip however, only reaches 450 K. Peak temperature at the end of the steel isolator sections is less than 400 K, and temperatures on the aluminum frustum reach only 375 K, and are relatively uniform.

Figure 13 shows descent heating to the test article. During descent, nosetip stagnation point temperatures are predicted to peak at about 1750 K shortly after the vehicle passes through 18 km (502.7 sec). Temperatures on the aluminum frustum remain near 400 K throughout descent until about 24 km, when transition is expected to occur, based on the simple Re_θ/M_e prediction. At this point, temperatures rise rapidly but remain less than 500 K through 18 km.
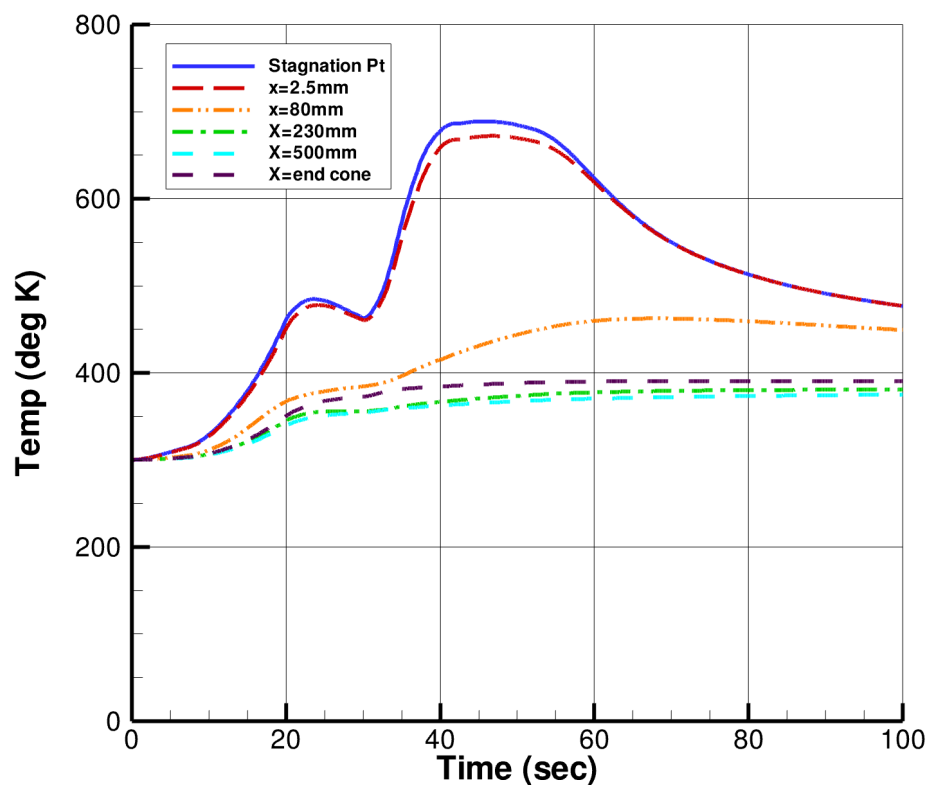
Figure 12 Ascent heating for HIFiRE-5
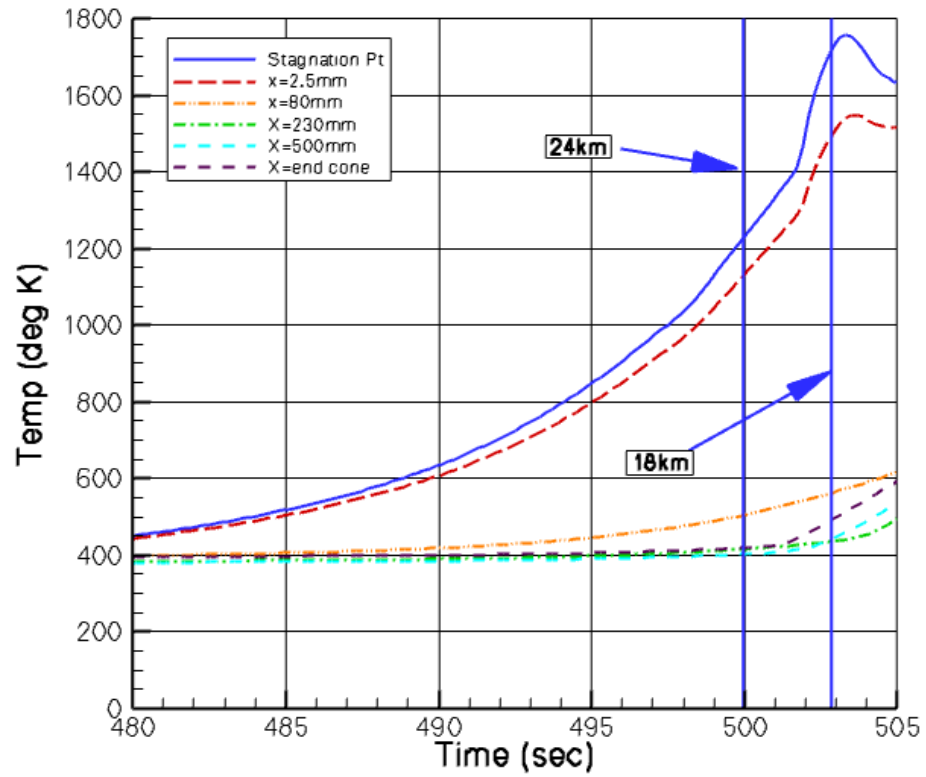
Figure 13 HIFiRE-5 descent heating.

4. NASA LaRC Wind Tunnel Testing

4.1. Experimental Methods

4.1.1. Model/Support Hardware

The HIFiRE Flight 5 Payload Outer Mold Line (OML) is a 2-1 elliptical cone with a 7 deg half angle on the minor axis, shown in Figure 5. The elliptic cone overhangs the second-stage booster in the major axis. An elliptical-to-circular transition section joins the elliptic cone test article to the cylindrical booster. All LaRC wind tunnel models were 15 in. long. The elliptic cone section as well as a portion of the transition section was modeled for the test. The flight vehicle elliptic cone will be 861 mm long, and at a model scale of 38.1%, the elliptic cone has a model length of 328 mm. Two different model configurations were fabricated for this test, each with a different nose shape. The first model will be referred to as the Baseline model and utilized the primary flight configuration for the nose. The nose tip cross-section in the minor axis describes a 2.5 mm radius circular arc, tangent to the cone ray describing the minor axis, and retains a 2:1 elliptical cross-section to the tip. The other configuration, referred to as the Nose 1 model and is an alternate flight nose cap shape generated from tangent circular arcs in the major and minor axes. The second nose tip yielded results that were not substantially different from the baseline shape and will not be discussed further.

The cast ceramic models used in the Mach 6 test series were manufactured from molds created from rapid prototyped resin patterns. Standard methods, materials, and equipment developed at NASA LaRC were used in fabricating the ceramic aeroheating test models.[37] All models were supported by 1-in. diameter cylindrical stainless steel straight stings mounted through the axis of symmetry. Fiducial marks were applied to the model surface using a coordinate measuring machine. The reference marks on the model surface were used to align the model in the tunnel for testing and to aid in data reduction using the phosphor thermography system.

Two boundary layer trip configurations were utilized in order to simulate the effects due to fasteners on the closeout panel (3-D "diamond" shaped trip) and the joint between the nose and body of the vehicle (2-D "strip" trip). The trip shapes are shown in Figure 14. Trip heights were 64 μm to 470 μm for the 3D trips and 89 to 554 μm for the 2D trips. All trips were fabricated from kapton tape. The 2D trips were 1.3 mm wide. The diamond shaped trips were 1.3 mm squares. Except for a limited number of runs, all trips were placed at an x/L location of 0.2 in order to represent the joint location. A small number of runs utilized trips at x/L = 0.5.
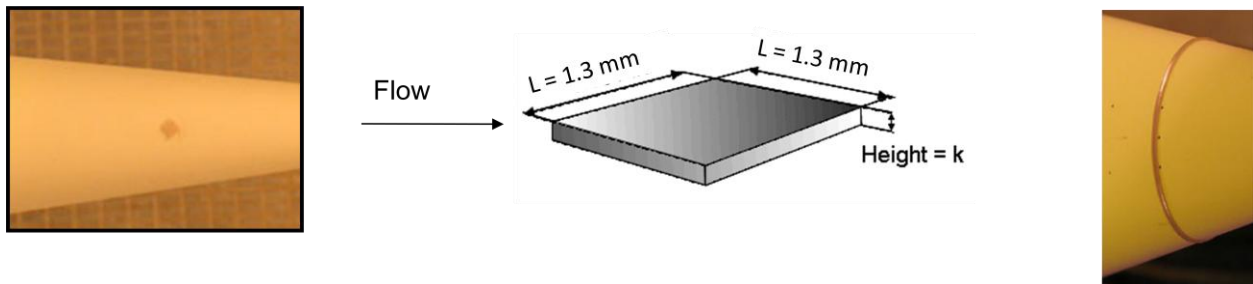
Figure 14: Boundary Layer Trips Utilized for HIFiRE 5 Testing; (a) diamond trip, (b) diamond trip dimensions, (c) strip trip

4.1.2. Facility

The data included in this report were obtained in the NASA Langley Aerothermodynamics Laboratory (LAL).[38] The 20-Inch Mach 6 Air Tunnel has well characterized perfect gas flows in terms of composition and uniformity. Representative test conditions for the facility are shown in Table 1. The values of $P_{t,1}$ and $T_{t,1}$ are accurate to within ±2%. The uncertainties in the angle of attack of the model are ±0.2º.

The Langley 20-Inch Mach 6 Tunnel is a blow down wind tunnel that uses dry air as the test gas. Air from two high pressure bottle fields is transferred to a 600-psia reservoir and is heated to a maximum temperature of 1000°R by an electrical resistance heater. A double filtering system is employed having an upstream filter capable of capturing particles larger than 20 microns and a second filter rated at 5 microns. The filters are installed between the heater and settling chamber. The settling chamber contains a perforated conical baffle at the entrance and internal screens. The maximum operating pressure is 525 psia. A fixed geometry, two-dimensional contoured nozzle is used; the top and bottom walls of the nozzle are contoured and the side walls are parallel. The nozzle throat is 0.34 in. by 20 in., the test section is 20.5 in. by 20 in., and the nozzle length from the throat to the test section window center is 7.45 ft. This tunnel is equipped with an adjustable second minimum and exhausts either into combined 41-ft diameter and 60-ft diameter vacuum spheres, a 100-ft diameter vacuum sphere, or to the atmosphere through an annular steam ejector. The maximum run time is 20 minutes with the ejector, though heating tests generally have total run times of 30 sec, with actual model residence time on tunnel centerline of approximately 5-10 sec. Models are mounted on the injection system located in a housing below the closed test section.

4.1.3. Experimental Methods

The two-color relative-intensity phosphor thermography measurement technique was used to obtain global experimental aeroheating data on the model.[39,40,41] This technique uses a mixture of phosphors that fluoresce in the bands of the visible spectrum when illuminated with ultraviolet light. The red and green bands are used and the intensity of the fluorescence is dependent upon the amount of incident ultraviolet light and the local surface temperature of the phosphor. This phosphor mixture, which is suspended in a silica ceramic binder and applied with an air brush, is used to coat a slip cast silica ceramic model. The final coating thickness is approximately 25 μm. Using a 3-CCD (Charge Coupled Device) camera, fluorescence intensity images of an illuminated phosphor model exposed to the heated hypersonic flow of the tunnel are acquired and converted to temperature mappings via a temperature-intensity calibration. The temperature-

intensity calibration uses the ratio of the red and green components of the image to construct a lookup table which converts the intensities to temperature values. Currently, this calibration is valid over a temperature range from 296 K to 444 K. The temperature data from the time-sequenced images taken during the wind tunnel run are then reduced to enthalpy based heat transfer coefficient at every pixel on the image (and hence globally on the model) using a heat-transfer calculation assuming one-dimensional semi-infinite slab heat conduction and a step function in the heat transfer coefficient, h.[40]

Table 1: Representative Test Conditions for the 20-In Mach 6 Air Tunnel

Tunnel	Test Gas	$P_{t,1}$, kPa	$T_{t,1}$, K	M_∞	Re_∞, m^{-1} $x10^{-6}$	P_∞, kPa	T_∞, K	q_∞, kPa	V_∞, m/s
Mach 6	Air	200	482	5.86	1.748	0.14755	62.0	3.544	920.7
Mach 6	Air	407	490	5.88	3.431	0.2922	62.1	7.088	929.0
Mach 6	Air	855	512	5.98	6.494	0.55986	63.2	13.996	951.8
Mach 6	Air	1724	506	5.99	13.261	1.11117	62.1	27.931	946.0
Mach 6	Air	2523	520	6.02	18.473	1.59346	63.4	40.348	957.9
Mach 6	Air	3282	517	6.04	24.216	2.05555	62.8	52.214	956.1

Global heating images and corresponding centerline data cuts will be presented in the non-dimensional h/h_{ref} format and were extracted from a two-dimensional image. The reference h value was based on the Fay-Riddell hemisphere stagnation point heating equation[42] with a nose radius of 0.6363 mm.

Uncertainties in the phosphor thermography are based on surface temperature rise, and those presented here are based on historical testing with a variety of model types. On surfaces with significant temperature rise, such as windside surfaces (>39 ℃), uncertainties are in the range of ±10%. For moderate temperature rise (11-17 ℃) such as the leeside, the uncertainties are roughly ±25%. More information on uncertainties in the phosphor thermography can be found in Refs. 40 and 41.

4.2.   Test Results

4.2.1. Windside Heating

One of the primary motivators for this wind tunnel testing was the desire to determine the heating rates and boundary layer transition characteristics of the windward surface of the HIFiRE 5 flight vehicle. Initial testing was done without trips in order to determine the smooth-body transition pattern. The transition pattern at zero AOA exhibited a double-lobed pattern as illustrated in Figure 15. This pattern closely resembles N-factor contours for stationary crossflow instabilities for the sharp elliptic cone. Figure 16 is the 0 deg AoA case at a Reynolds number of $9.8x10^6$/m with a significantly more sensitive color bar range. The jagged nature of

the transition front is evident, another property of stationary crossflow. On the basis of these resemblances, this transition pattern is presumed to be the result of crossflow.[43] As shown in Figure 15, the centerline heating departed from the laminar heating conditions at all unit Reynolds number tested, though at the lowest unit Reynolds number, 3.6×10^6/m, heating rates did not reach fully turbulent heating conditions before the end of the model. All of the other conditions reached a fully turbulent value and as the Unit Reynolds number was increased, the transition moved closer to the nose of the vehicle. As shown in the heating images for each set of data, the primary heating was off centerline. Figure 17 shows that the heating is highest near the leading edges of the vehicle and drops off slowly towards the centerline, indicative of turbulent heating conditions. As the Unit Reynolds number is increased, transition moves closer to the leading edge.

A prominent feature in the images is a "cold streak" of lower heating that runs down the centerline of the model on the minor axis. This local dip in heating is probably caused by an influx of fluid from the high-pressure leading edges to low-pressure centerline. This influx causes a thick inflected boundary layer on the centerline that reduces heating.[25] This feature is evident in the turbulent as well as the laminar boundary layer. Generally the transition patterns are similar to those observed for the HIFiRE-5 configuration in the CUBRC LENS I wind tunnel, with the exception of leading-edge transition, as noted in the discussion of the side surface below.[44] It should be noted that the AEDC elliptic cone transition patterns show no well-defined crossflow side lobes. This may be due to the sharp nose, which might be expected to destabilize the centerline, or simply due to lack of resolution due to the placement of sensors.
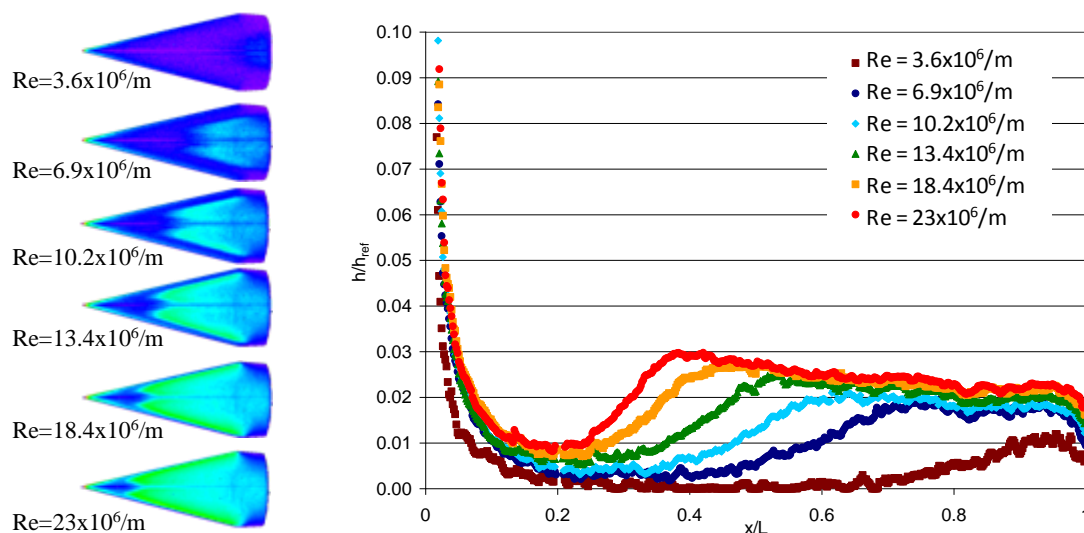
Figure 15: Centerline Heating for the HIFiRE 5 Vehicle at 0 deg AoA

Approved for public release; distribution unlimited.
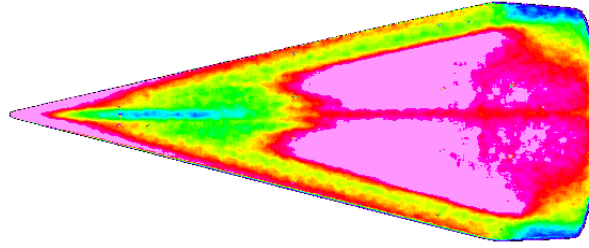
Figure 16: Transition Front on the Windside at 0 deg AoA, Re = 10.2x10^6/m (altered color bar range)
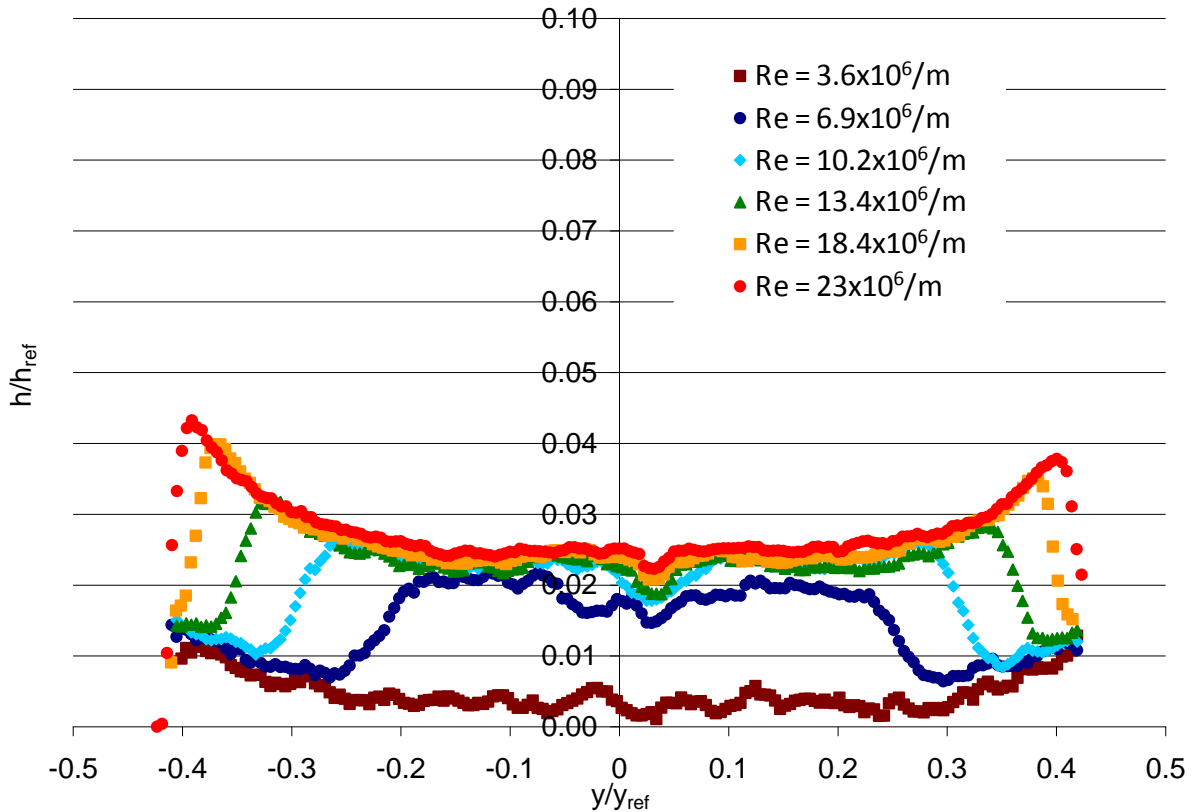
Figure 17: Spanwise Heating on HIFiRE 5 at x/L = 0.7, 0 deg AoA

As the angle of attack is increased, the centerline boundary layer transition becomes more evident and the transition pattern changes from a two- to three-lobed pattern. As shown in Figure 18, at -4 deg AoA, the leeside heating (discussed further in the next section) is in a single lobe around the centerline. At -2 deg AoA, the two-lobe pattern starts to emerge and continues to develop at 0 deg AoA. At 2 deg AoA (windward), a small centerline lobe becomes evident and is roughly inducing transition at the same x/L location as the off-centerline transition. As the angle of attack is further increased to 4 deg, the centerline transition becomes more evident and transitions forward of the off-centerline region. This pattern is indicative of the switch from in-flow towards out-flow as the angle of attack is increased for the vehicle.[45]
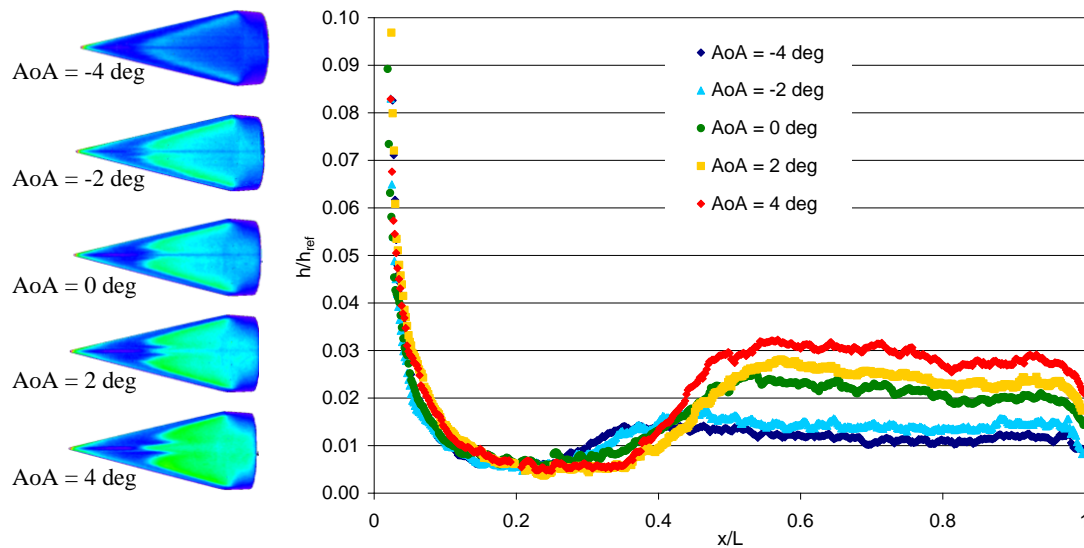
Figure 18: Angle of Attack Effects at Re = 13.4x10^6/m

Significant effort was spent on the boundary layer transition tripping on the windward surface of the HIFiRE 5 vehicle. At 0 deg AoA no boundary layer trips utilized (ranging from 89 to 470 μm) were able to induce early boundary layer transition on the centerline of the flight vehicle. Both 2-D (strip to represent joints on the vehicle) and 3-D (diamond shaped to represent the fasteners on the closeout panel of the vehicle) trips were tried. Some localized increases in heating were evident (Figure 19) immediately aft of the trip but the flow quickly returned to the un-tripped heating levels. It should be noted that the natural boundary layer transition onset for the case shown (Unit Reynolds number of 18.4x10^6/m) is very close to the trip location [the centerline data seems to show transition earlier than the images to the left but this is due to the color contours used and the transition onset locations are accurate]. For other, lower, unit Reynolds numbers tested, the natural transition locations move aft on the vehicle and the same pattern of a localized increase in heating followed by the return to un-tripped heating levels is repeated (not shown). At no point was a "fully effective" (transition immediately at the site of the trip) trip found. It is evident from the heating images that while there seemed to be very little effect of the trip on the centerline, there was significant effect on the leading edges of the vehicle (2-D trips) and off-centerline (3-D trips). The 2-D trips did not have a significant effect on the cross-flow transition regions previously identified off-centerline.
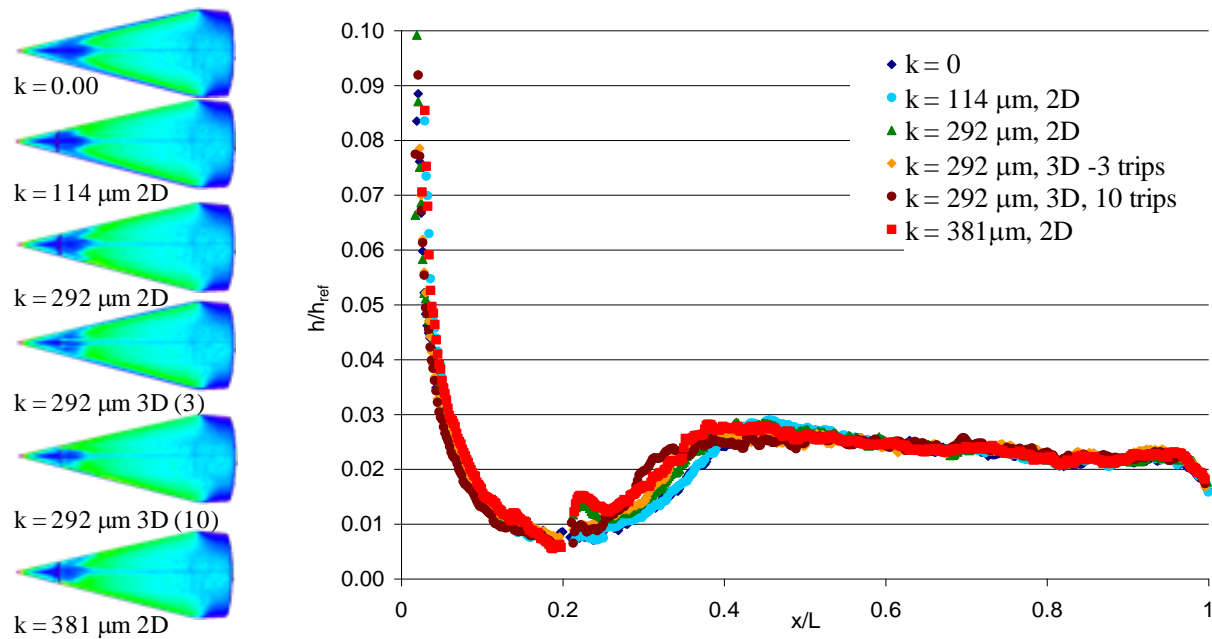
Figure 19: Centerline Tripped Heating Data at 0 deg AoA, Re = 18.4x10^6/m

An attempt was made to quantify the range of critical boundary layer trips (regarded as causing BLT onset somewhere downstream on the vehicle) at two Unit Reynolds numbers, 13.1 and 18.4x10^6/m. Various boundary layer trip heights were tested at 0 deg AoA and 0 deg sideslip. The maximum value of the range (see Table 2 for windside surface results) is associated with the smallest trip that caused a departure from the laminar heating levels. The minimum value stated is associated with the next smallest trip tested, as that trip height did not cause a departure from the laminar heating levels. For the unit Reynolds number of 13.1 x10^6/m, the critical trip is between 267 and 356 μm and for 18.4x10^6/m, the critical trip is between 114 and 292 μm when using the 2D trip shape.

The 2-D trips had a more significant effect both on and off of the centerline at angle of attack, probably because of thinner boundary layers. When the vehicle was pitched to 4 deg AoA, the 2-D trips caused a shift forward in the onset of centerline boundary layer transition as well as transition on the leading edges (Figure 20). Increasing the trip height moved the transition onset location further forward on the vehicle.

Table 2: Critical Boundary Layer Trip Height for the Windward Surface (0 deg AoA, 0 deg Sideslip)

Unit Reynolds Number (x10^6/m)	Trip Geometry	Minimum Critical Height (μm)	Maximum Critical Height (μm)
13.1	2D (strip)	267	356
18.4	2D (strip)	114	292
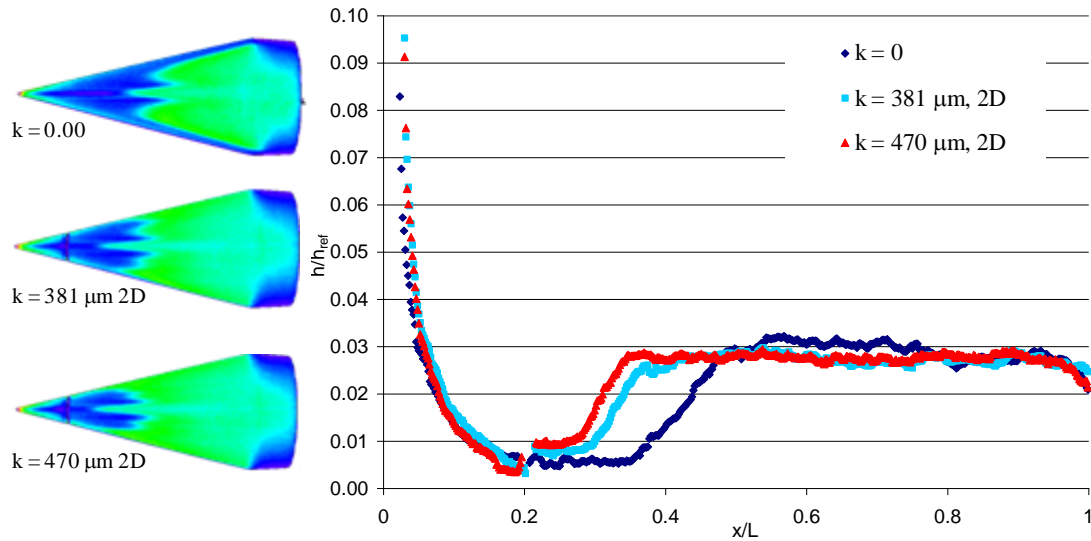
Figure 20: Angle of Attack Effect on Tripped Windside Heating at Re = 13.4x10^6/m

A concern for the flight vehicle is the potential contamination of heating flight data on the smooth, clean side by access-panel closure hardware on the other side of the flight vehicle. For this reason, discrete boundary layer trips were tested at various locations on the windward surface in an attempt to quantify the spreading angle of the turbulent wedge associated with the trip. Three locations were initially tested, to be referred to as centerline, Trip Location 1 and Trip Location 2. See Figure 21 for a diagram of trip locations. All three trips were at x/L=0.2. The Trip Location 1 was 5.8 mm off the centerline and the Trip Location 2 was 8.9 mm off the centerline. The centerline trips were not found to cause downstream boundary layer transition at any conditions and will not be discussed further. The Trip Locations 1 and 2 did result in visible disturbances at most conditions though were significantly more effective at increased angle of attack. A large trip was utilized (k = 470 μm) in order to ensure the maximum possibility of resulting in non-laminar heating. No study was completed on the effect of trip height. In all cases, the augmented heating did not spread to the leading edge of the vehicle far enough upstream to affect the opposite side of the elliptical cone. This indicates that the hardware on the closeout panel side of the flight vehicle would not influence the heating on the other "clean" side of the vehicle.
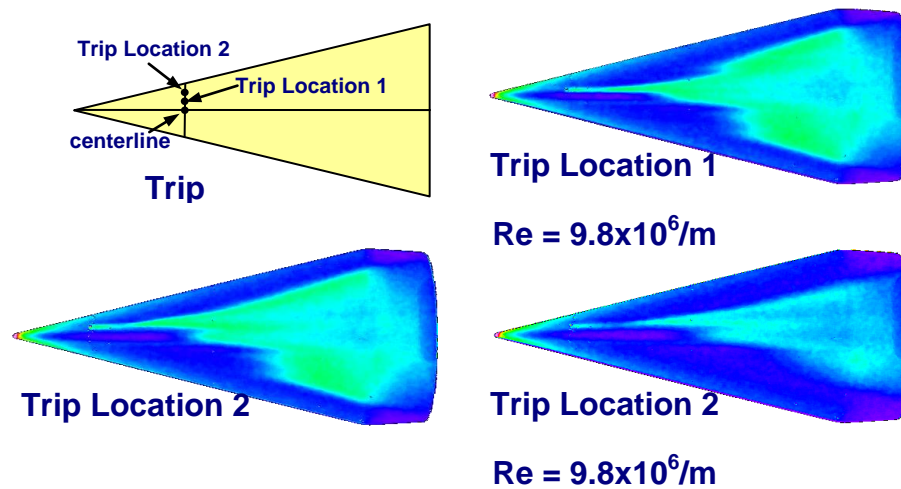
Figure 21: Spreading Angles from Discrete Trips on the Windward Surface

4.2.2. Leeside Heating

Leeside surface heating and boundary layer transition characteristics of the HIFiRE 5 vehicle were required as a part of the ground test program. No boundary layer tripping was done for the leeside surface and -2 and -4 deg AoA were tested with 0 deg sideslip. A variety of Unit Reynolds numbers were run in order to characterize the natural boundary layer transition patterns for the leeside surface. As shown in Figure 22, as the Unit Reynolds number is increased at -2 deg AoA, the heating levels increase. For all Unit Reynolds numbers tested there appears to be turbulent heating on the body of the vehicle, with the departure from laminar heating occurring earlier as the Unit Reynolds number is increased. Elevated heating due to transition occurs off-centerline. The double-lobed transition pattern is similar to that observed on the vehicle at zero AOA, and suggests that crossflow is the dominant transition mechanism on the leeside. At -4 deg AoA, the heating appears to be a single lobe (shown in Figure 18).
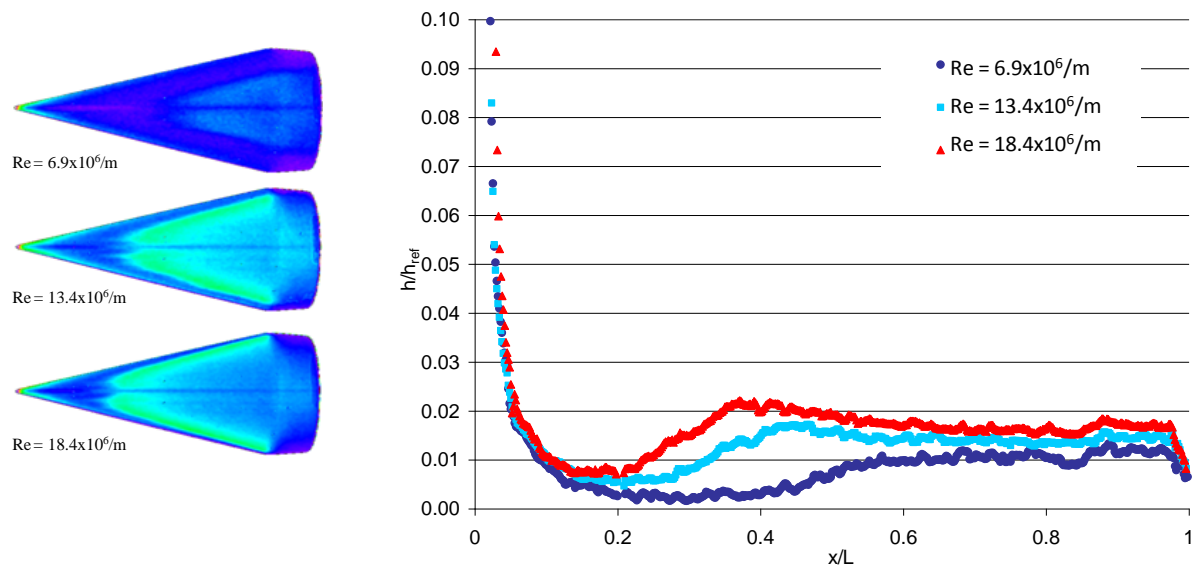
Figure 22: Leeside Heating on the HIFiRE 5 Vehicle, -2 deg AoA

4.2.3. Leading Edge Heating

Heating and boundary layer transition characteristics of the leading edge of the vehicle were determined. The baseline shape was tested extensively in the tunnel to determine the effects of natural and forced boundary layer transition. Initial testing indicated that in the absence of boundary layer trips, the leading edge would naturally transition at a unit Reynolds number of $17.4x10^6$/m, shown in Figure 23. The turbulent or non-laminar heating associated with the windside and leeside of the vehicle do not contaminate the centerline of the side surface at 0 deg AoA and 0 deg sideslip. This Unit Reynolds number value was used for the remainder of the testing as the target Unit Reynolds number for the side surface. A boundary layer trip was considered to be critical if it caused deviation from the laminar heating profile at this Unit Reynolds number. In all cases the smooth leading edge transition appears downstream from the centerline transition, and appears to result from a smooth merger of the turbulent fields on the top and bottom of the model. This is in contrast to a distinct leading edge first transition observed in some cases in tests at CUBRC.[44] The cause of this difference in transition behavior between the current tests and CUBRC tests is unclear, but may be related to the higher wall-cooling used in the CUBRC tests.
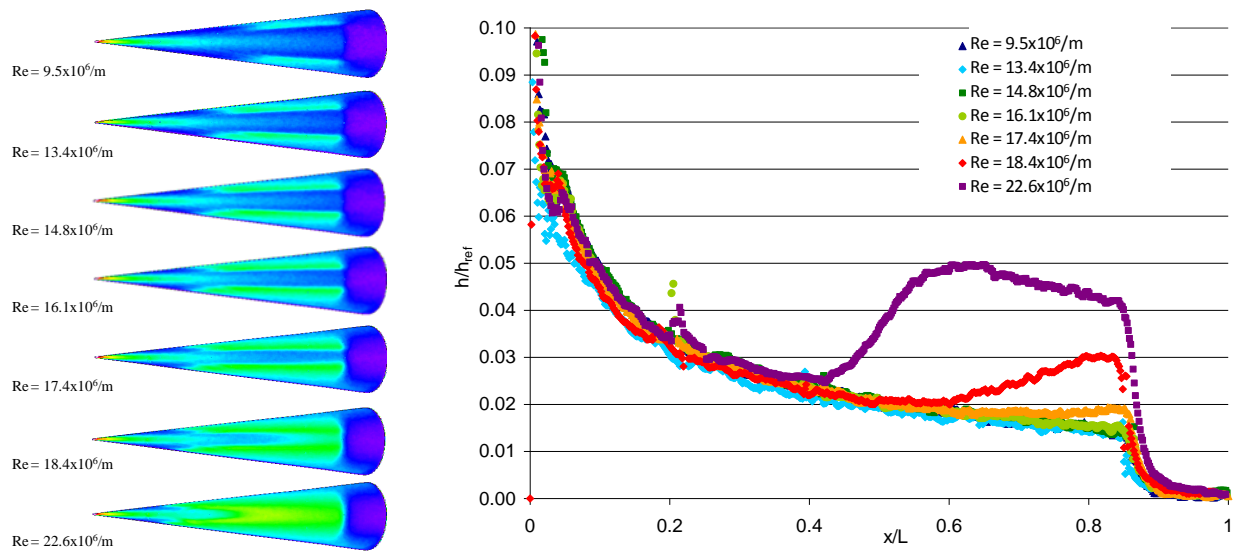
Figure 23: Leading Edge Heating on the Side Surface, AoA = 0 deg

Just as on the windside surface, the side surface was tested with a variety of boundary layer trips to determine the range of trip effectiveness. The focus was on the 3-D ("diamond") trips to represent fasteners on a closeout panel on the vehicle and 2-D ("strip") trips to represent joints between the nose and body sections of the vehicle at 0 deg AoA and two unit Reynolds number conditions, (a) the 17.4×10^6/m condition identified above and (b) 3.0×10^6/ft to match the maximum quiet-flow Reynolds number in Purdue University's Mach 6 Quiet Tunnel. As shown in Figure 24 for the 2D trips with a Unit Reynolds number of 9.8×10^6/m, the critical boundary layer trip height was found to be between k = 229 and 292 μm. The ranges determined for this case and the other three cases are summarized in Table 3. At the unit Reynolds number of 17.4×10^6/m case with the 3-D trips, the smallest boundary layer trip tested (k = 64 μm) caused boundary layer transition and no smaller boundary layer trips were available. In an attempt to further bound the values and in the absence of smaller trips, the trip was placed further aft on the model (x/L of 0.5 as opposed to 0.2 for the rest of the boundary layer trip testing). Even at this further aft location the k= 64 μm trip did cause a notable departure from the laminar centerline heating (Figure 25). No further investigation was done. At the lower unit Reynolds number condition (Re = 9.8×10^6/m) the critical boundary layer trip height was between 114-203 μm. for the 3-D trip case and 381-470 μm for the 2-D trip case. It is clear from this testing that the 3-D trip is more effective than the 2-D shape.
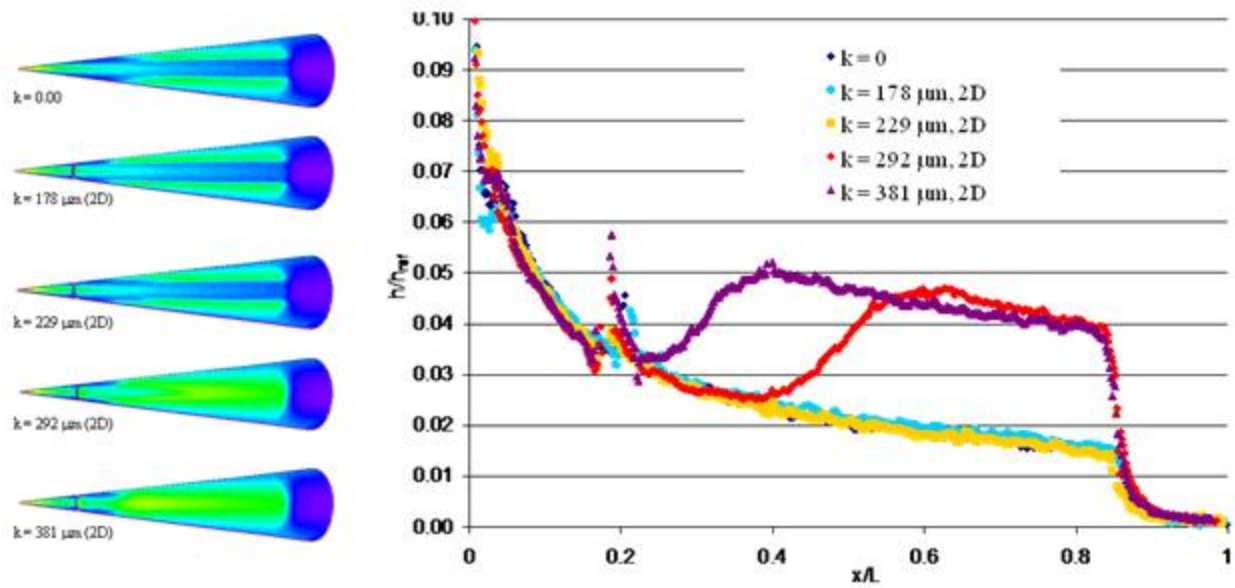
Figure 24: 2D Boundary Layer Trip Effects on Side Centerline Heating, Re = 17.4x10^{6}/m, AoA = 0 deg

Table 3: Critical Boundary Layer Trip Height for the Side Surface

Unit Reynolds Number (x10^{6}/m)	Beta (deg)	Trip Geometry	Minimum Critical Height (μm)	Maximum Critical Height (μm)
9.8	0	3D (diamond)	114	203
9.8	0	2D (strip)	381	470
17.4	0	3D (diamond)	NA	64
17.4	0	2D (strip)	229	292
18.4	4	2D (strip)	229	318
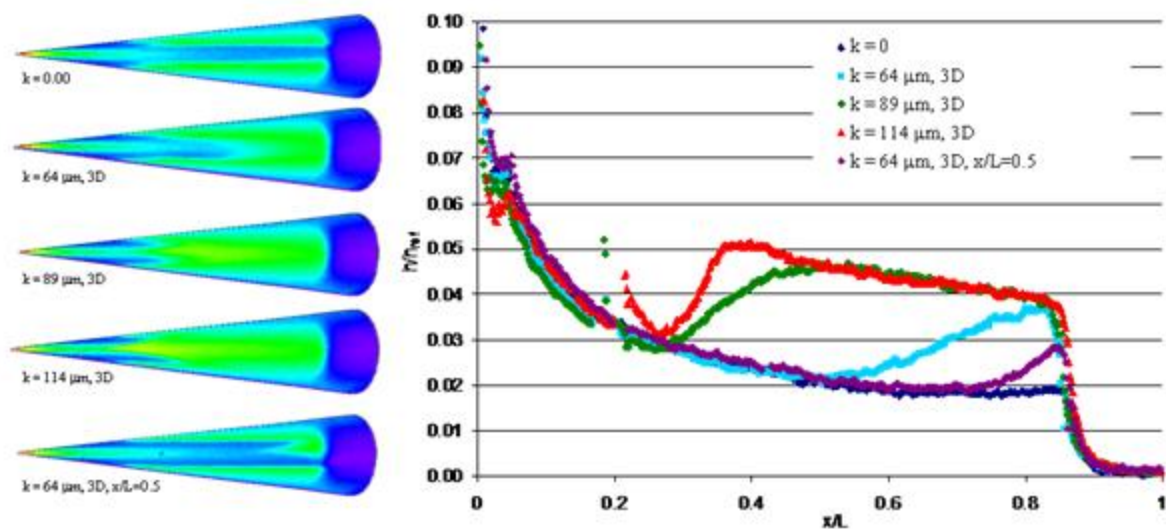
Figure 25: Side Surface Leading Edge Heating at Re = 17.4x10⁶/ft, AoA = 0 deg [trips at x/L=0.2 unless noted]

A brief study in the effect of sideslip angle on the side heating was done and the vehicle was tested at -4, 0 and 4 deg sideslip. All three cases were tripped with a 318 μm 2-D trip at Re = 18.4x10⁶/m (except for the 0 deg case where the closest trip size was 292 μm at a Unit Reynolds number of 17.4x10⁶/m). As shown in Figure 26, the centerline transitioned at all of the sideslip angles but boundary layer transition moves significantly forward at a sideslip of +4 deg. At a sideslip angle of -4 deg, the transitional/turbulent leading edge heating appears to result from a smooth merger of the turbulent fields on the top and bottom of the model. The appearance of the leading edge transition in this case is different from the zero AOA tripped case, and the leading edge transition does not appear to be the result of the trip at -4 deg sideslip.
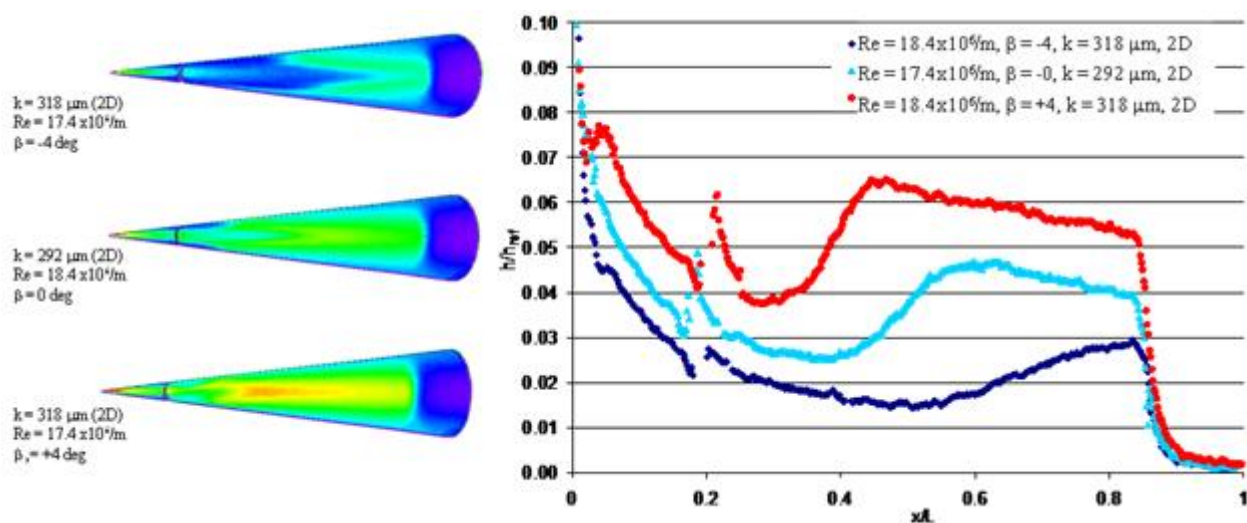
Figure 26: Effect of Sideslip Angle on the Side Heating, AoA = 0 deg

At the sideslip +4 deg case, a boundary layer tripping study was completed at a Unit Reynolds number of 18.4×10^6/m and 0 deg AoA. As shown in Figure 27, the k=229 μm trip did not cause a departure from the laminar heating. When the k=318 μm trip was used, the flow transitioned very quickly and close to the trip location. No testing was done in order to further refine the range.
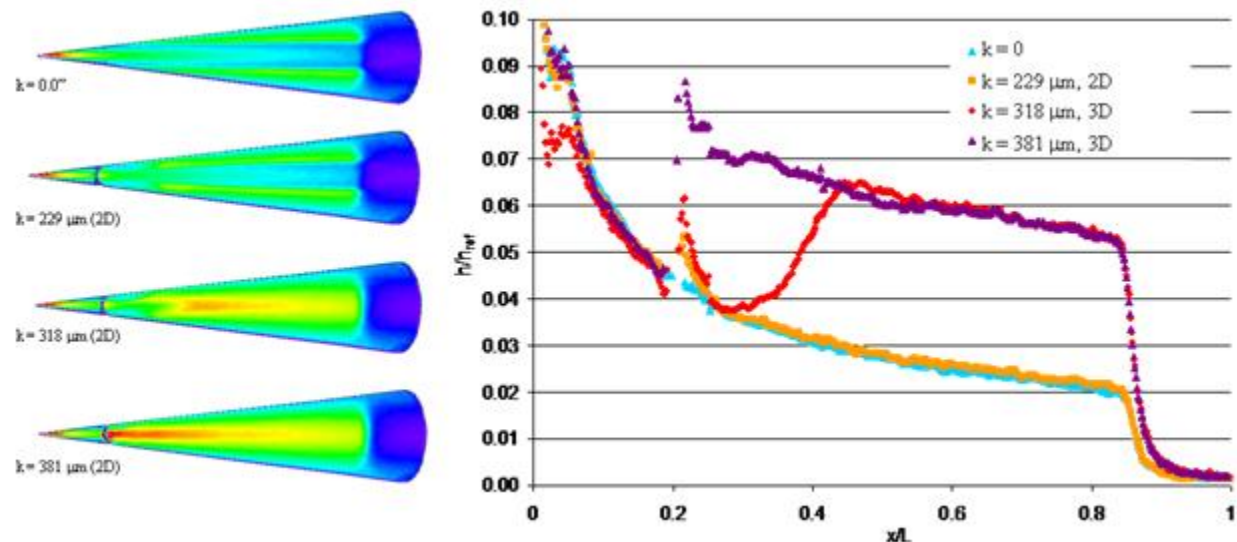
Figure 27: Boundary Layer Trip Effectiveness for the Side Surface, 4 deg Beta, Re = 18.4×10^6/m

4.3.   Anticipated Flight Transition Reynolds Numbers

There is no test window per se during the HIFiRE-5 flight, since data are acquired and telemetered continuously throughout ascent and descent. However, the beginning of the useful reentry test period is defined by the highest altitude at which transition may be expected. The end of the effective test window occurs either where the vehicle fails structurally due to combined aerothermal loads, or flow over the vehicle is fully turbulent. The HIFiRE-0 vehicle departed from stable flight at approximately 19 km, probably due to fin failure, although roll anomalies occurred as high as 23 km.[31] An important goal of the HIFiRE-5 analysis and ground test was to determine probable transition altitudes.

Transition altitudes were determined from wind tunnel results and stability calculations. [43] Presumably, wind tunnel results will be biased towards lower transition Reynolds numbers due to tunnel noise[46] and provide an upper altitude (lower Reynolds number) bound for transition. N-factor correlations, using expected correlating values for flight (approximately 8-12), should give lower altitude (higher Reynolds number) bounds on transition. Of interest are the highest altitude at which transition may be expected, and the altitude at which flow is turbulent from the most upstream sensors, a case in which the entire vehicle is turbulent and no boundary layer transition data is provided. Determination of altitude transition bounds is complicated by the dramatic difference between the test-article centerline stability and leading edge stability. Transition altitudes are thus bounded by high altitude, earliest and latest transition estimates, and low altitude, earliest and latest transition estimates, each for centerline and leading edge.

Figure 29 shows an example of heat transfer data NASA LaRC Mach 6 wind tunnel.[47] Transition Reynolds numbers were extracted by plotting measured heat transfer rates in log-log coordinates. A straight line was fit to the sensibly laminar portion of the data, and another to the transitional portion of the data. The lower bound on transition is taken as the point where heat transfer first deviates from the laminar trend, and the upper bound is taken as where the two extrapolated lines intersect.
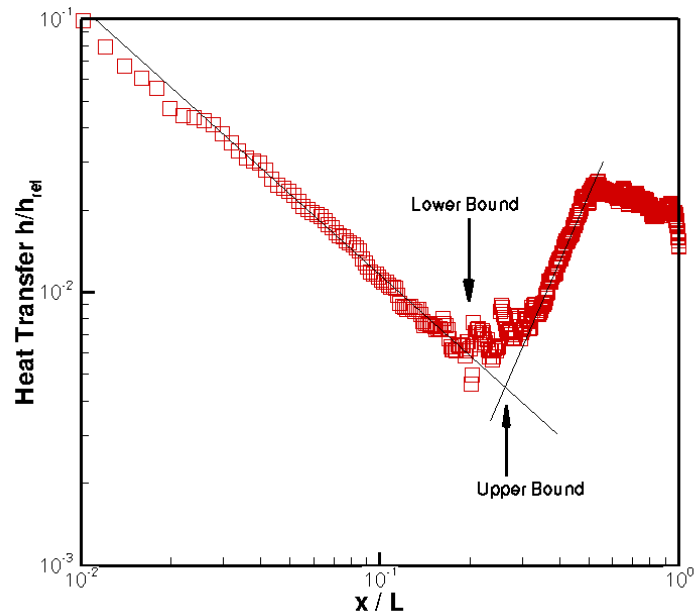
Figure 28 Example of transition location determination

Figure 29 shows upper and lower bound Reynolds numbers for centerline transition, extracted from wind tunnel data as described above. There is a strong and probably spurious trend in transition Reynolds number with tunnel unit Reynolds number. Although the "unit Reynolds number effect" has been observed and speculated upon for many years, the general consensus is that it seems to be an artifact related to wind tunnel noise.[46] Centerline transition Reynolds numbers are thus expected to lie between $6x10^5$ and $1.8x10^6$. With a smooth leading edge surface, transition was observed only under a small number of test conditions corresponding to higher Reynolds numbers within the test matrix. No unit Reynolds number effect was observed in the leading edge transition Reynolds numbers (due either to the limited data set or true flow physics). Leading edge transition Reynolds numbers obtained by the same method (based on freestream conditions and leading edge diameter) ranged from $4.5x10^5$ to $5.8x10^5$.

The expected extreme ranges for transition on HIFiRE-5 are plotted on Reynolds-number versus altitude maps in Figure 30. Figure 30 plots length Reynolds number (based on freestream conditions and overall reference length L=0.861m) on the left, and leading edge diameter Reynolds number (based on freestream conditions and diameter at the base of the test article at x = 0.861 m) on the right. The black line indicates the Reynolds number during reentry obtained from trajectory simulation. In both plots a green line is superimposed to indicate the expected range of altitudes at which transition may begin near the base of the cone. The extent of this region is determined by the transition Reynolds numbers derived from wind tunnel data

described above. A red line is superimposed to indicate where transition is expected to move upstream of the forward sensors at x=0.3 m, again as derived from wind tunnel data. The green and red points indicate these respective altitudes as derived from PSE computations. Freestream-based Reynolds numbers can only serve as relatively crude surrogates for more sophisticated N-factor correlations, but since the Mach number, wall-temperatures and angle of attack vary very little over the trajectory range of interest, these Reynolds numbers are adequate for engineering estimates.

In contrast to the wind tunnel data, which shows earliest transition on the centerline, stability calculations indicate that leading edge and centerline transition will occur at nearly identical Reynolds numbers. This was observed in higher-Reynolds number cases tested at CUBRC.[44] If transition occurs at the extreme low-limit of Reynolds number $(6x10^5)$ this would correspond to an altitude of 39.4 km (492.5 sec). A more plausible transition altitude would be that derived from PSE stability analysis, corresponding to a length Reynolds number of $3.7x10^6$. This altitude is 28.3 km, occurring at 497.9 seconds. Figure 11 indicates that if the vehicle is properly aligned by the bang-bang maneuver, AoA of less than one degree may be achieved at 39.4 km altitude.
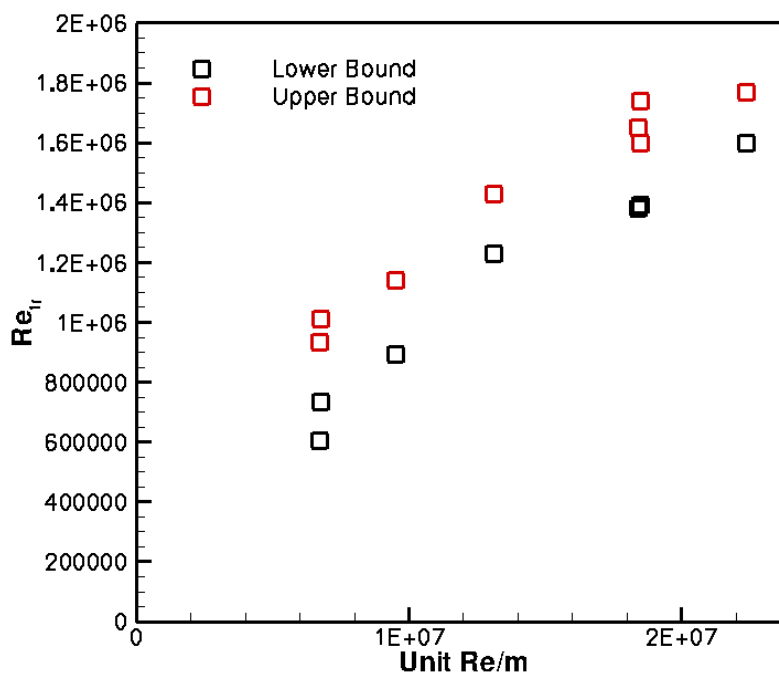
Figure 29 Centerline transition Reynolds numbers from wind tunnel data
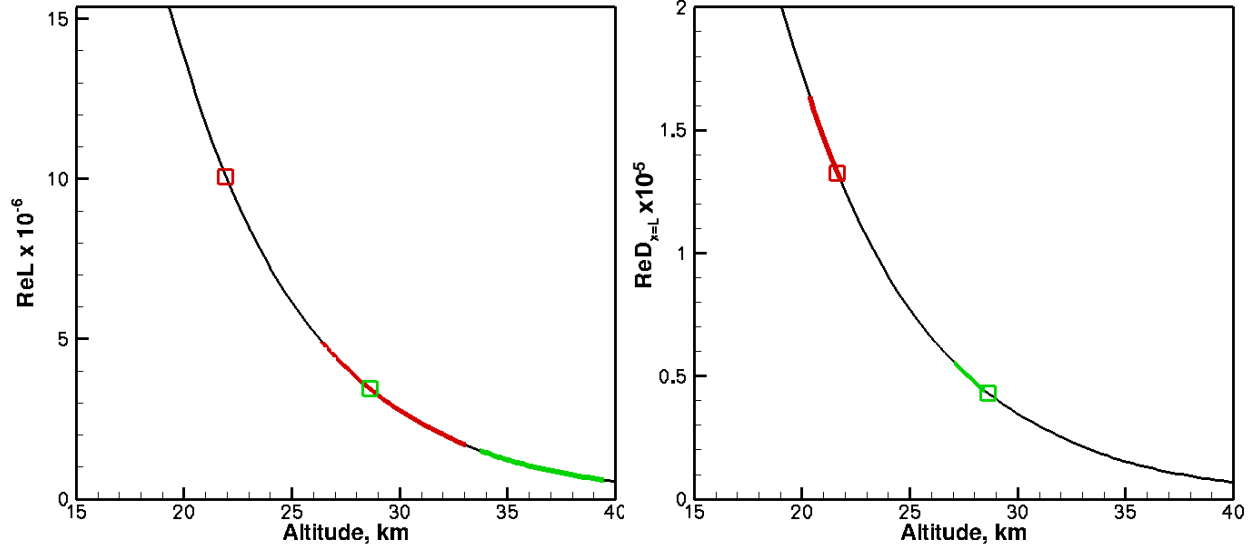
Figure 30 Length Reynolds number (left) and leading edge diameter Reynolds number (right) as functions of altitude.

4.4.   Correlations for Roughness-Induced Transition

The primary concern for HIFiRE-5 roughness occurs on the leading edge, where the boundary layer is thinnest. Roughness was applied using 2D (tape strips) and 3D (tape squares) to the HIFiRE-5 model leading edge in the NASA LaRC 20-inch Mach 6 wind tunnel.[47] Heat transfer measurements from these experiments were used to determine the transition location due to the roughness elements. The procedure to determine the transition location was similar to that outlined previously for smooth-body transition. These tests confirmed that the leading edge was the region of the model most susceptible to roughness tripping. The boundary layer tripped more effectively with diamond-shaped roughness than with the 2D strip. Roughness correlations were used to extrapolate the wind tunnel results to flight conditions in order to place requirements on the flight-vehicle full-scale roughness.

Poll used the parameter $\overline{R}$ to correlate incompressible swept cylinder leading edge transition, and mapped this correlation to compressible flow by evaluating $\overline{R}$ at a reference temperature T^* to obtain the correlating parameter $\overline{R}^*$.[48] Although $\overline{R}^*$ was developed for roughness on swept cylinders, and the HIFiRE-5 configuration possesses a non-cylindrical leading edge that increases in diameter in the downstream direction, $\overline{R}^*$ was investigated as a representative correlation. The correlating parameters were obtained using Newtonian theory, consistent with past results published by other investigators. The elliptic cone leading edge radius is taken in the plane transverse to the freestream. Although strictly speaking the leading edge radius should be defined normal to the leading edge, the radius in the plane normal to the freestream velocity is easier to define and for the high sweep of HIFiRE-5, is within 4% of the radius normal to the leading edge.

Very little data regarding transition from 3D roughness exists for swept leading edges in hypersonic flow. The HIFiRE-5 data are compared in Figure 31 to results of Creel, et al. [49] obtained in the NASA LaRC Mach 3.5 quiet tunnel. The Creel data were obtained on a cylinder swept at 60-deg. Critical roughness occurs at $k/\eta*$ slightly less than one. Critical roughness is defined as roughness just large enough to affect transition. Effective roughness occurs at $k/\eta*$ near two. Effective roughness is defined as roughness so large that further increases in height cause no further forward movement of transition.[50] Results show that the data are generally in agreement with the correlation obtained by Creel. Creel et al. observed similar trends for a 45-deg sweep model. Critical roughness values were higher for the 45-deg sweep configuration than the 60-deg sweep configuration. The Mach 3.5 data also show that transition was more sensitive to roughness under noisy flow, compared to quiet flow.
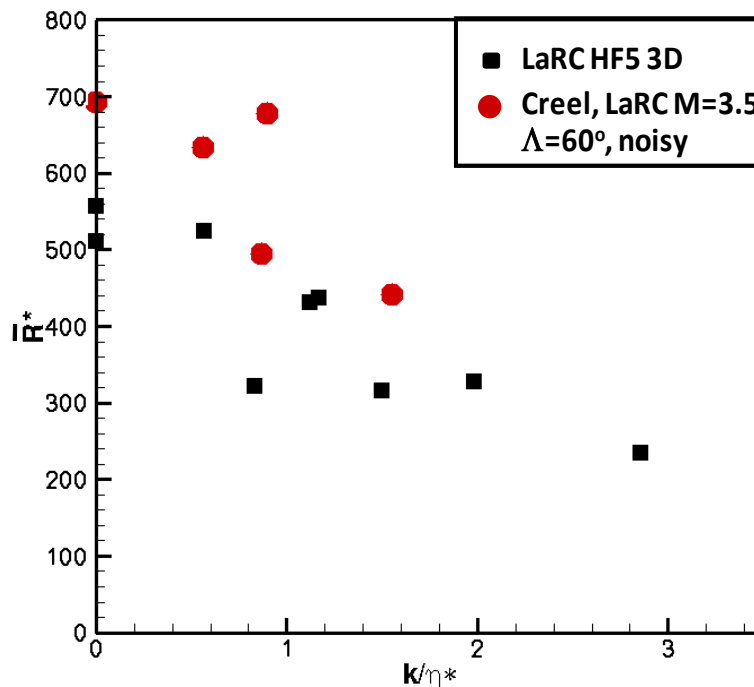
Figure 31 Scaling of transition due to 3D roughness

A larger body of data exists regarding 2D roughness, usually trip wires applied around the leading edge.

Figure 32 compares 2D tape strip data for HIFiRE-5 to other transition data from 2D trips on cylinders by Murakami et al.,[51] Benard et al.,[52] and Da Costa, as cited in Benard. Data with arrows represent bounding values only. These data, coming as they do from various wind tunnels, Mach numbers and geometries, show a great deal of scatter. The general trend of the HIFiRE-5 data is consistent with data from cylindrical leading edges. The HIFiRE-5 leading edge transition is unaffected by roughness for $k/\eta* < 3$.

Since the HIFiRE-5 configuration does not possess a cylindrical leading edge of constant radius, it is not immediately clear why the $\overline{R}^*$ correlation collapses the data. The $\overline{R}^*$ versus $k/\eta*$ correlation is based on the length scale $\eta*$, which characterizes the boundary layer velocity and

integral thicknesses for similar profiles. In order to assess the suitability of η^* as a length scale for the HIFiRE-5 boundary layer, the displacement and momentum thicknesses along the leading edge, as determined from a Navier-Stokes solution for the NASA Mach 6 model,[53] were normalized by η^*. Figure 33 shows that beyond 0.1 m downstream of the nosetip, η^* characterizes the boundary layer thickness well, so $\overline{R}^*$ versus k/η^* might be expected to correlate HIFiRE-5 leading edge transition, just as it correlates transition on swept cylinders.

Figure 31 indicates that the critical value of k/η^* for 3D roughness is approximately 0.6. Figure 32 shows 2D roughness begins to be significant when $k/\eta^* > 3$. These values are approximately where transition begins to move upstream from the smooth-body case. The distribution of roughness height along the leading edge at 18 km altitude during descent, corresponding to these two values, is shown in Figure 34. The 18 km altitude is chosen to set roughness tolerances since it is the lowest expected altitude (highest Reynolds number) at which data will be obtained. 2D roughness is assessed at the first joint location of 0.1 meters, since this represents the most probable form of 2D roughness. At this location the allowable joint height mismatch would be 0.22 mm. At the same location, tolerances for 3D roughness are much more stringent, 0.045 mm. Data obtained under noisy and quiet flow conditions for HIFiRE-1 in the Purdue Mach 6 quiet tunnel[8] indicate that tripped transition may be affected by wind tunnel noise. Critical and effective roughnesses were higher under quiet conditions. Creel et al.[49] observed similar behavior for leading edge roughness in supersonic flow. Therefore, allowable-roughness correlations based on noisy wind tunnel data may be conservative when extrapolated to flight. Correlations may only be expected to provide at best an order-of-magnitude estimate of allowable roughness. Experience on HIFiRE-1 showed that a tolerance of 0.08 mm could be held at joints. As an added factor of safety, this lower value was imposed for maximum allowable steps at joints, well below the 0.22 mm value obtained from the k/η^* correlation for 2D roughness.
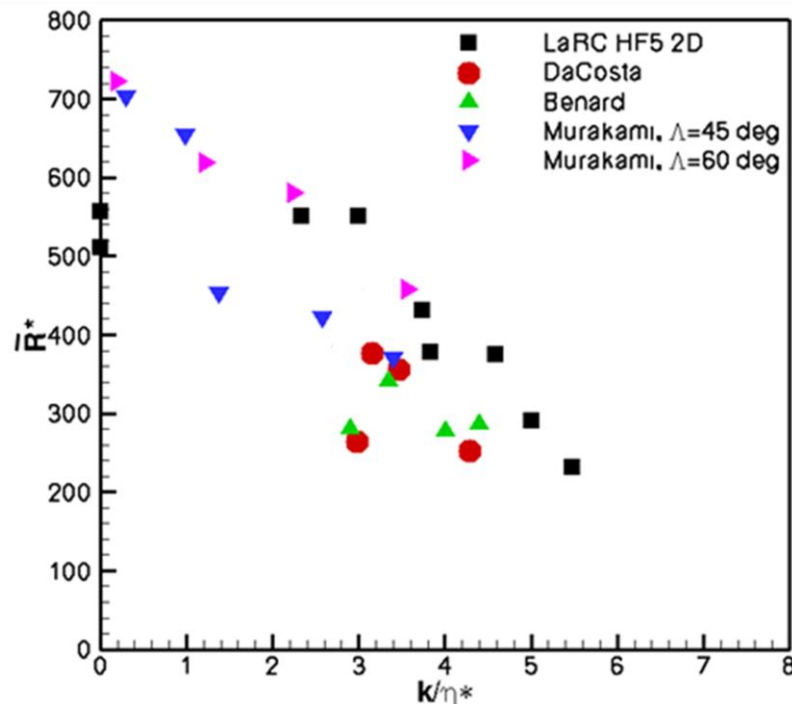
Figure 32 Scaling of transition due to 2D roughness
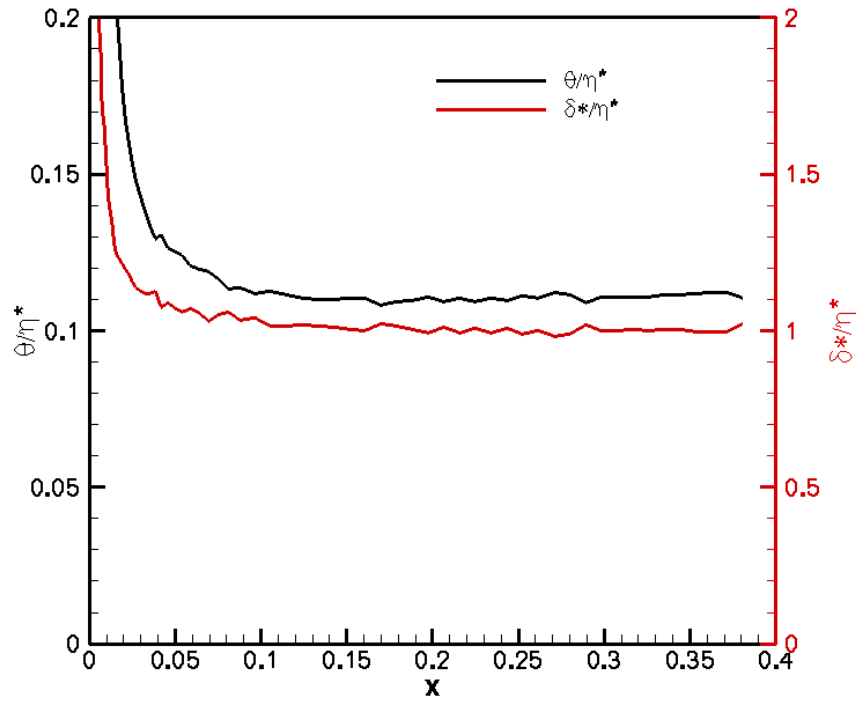
Figure 33 Boundary layer thicknesses normalized by length scale η^*.
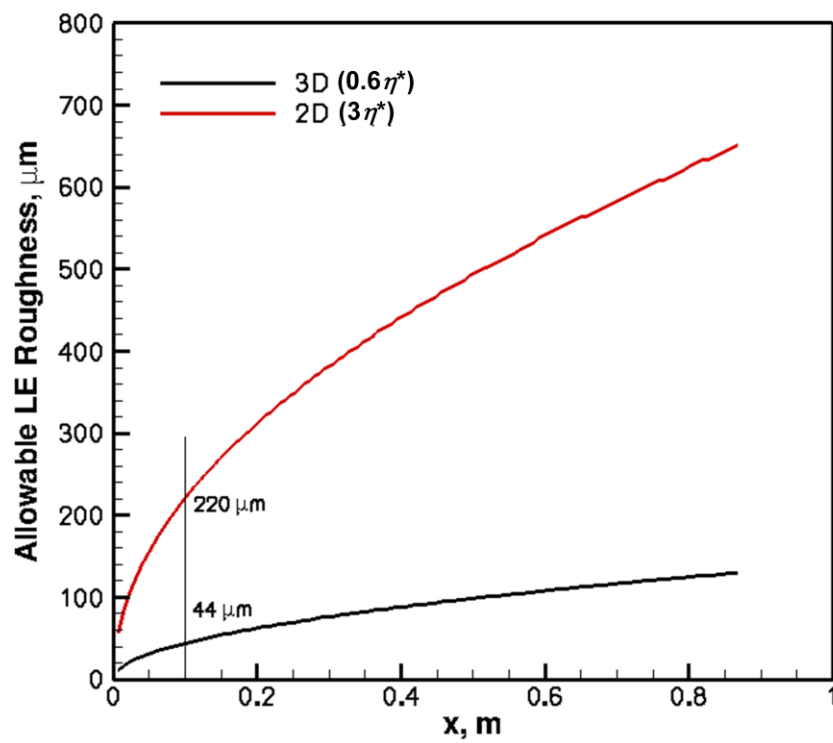
Figure 34 Allowable roughnesses along HIFiRE-5 leading edge at 18 km.

The natural construction for the HIFiRE-5 vehicle would be a clamshell shape, similar to HIFiRE-1. However, this would place longitudinal joints along the leading edge, precisely where the configuration is most susceptible to roughness. A split along the *x-y* plane along the minor axis was rejected since it would make access to internal components inconvenient. In order to prevent this, the vehicle is designed with one-piece leading edges, as shown in Figure 35. Sliding internal keys, similar to HFIRE-1,[14] lock the leading edges together with top and bottom clamshell pieces without external penetrating fasteners.
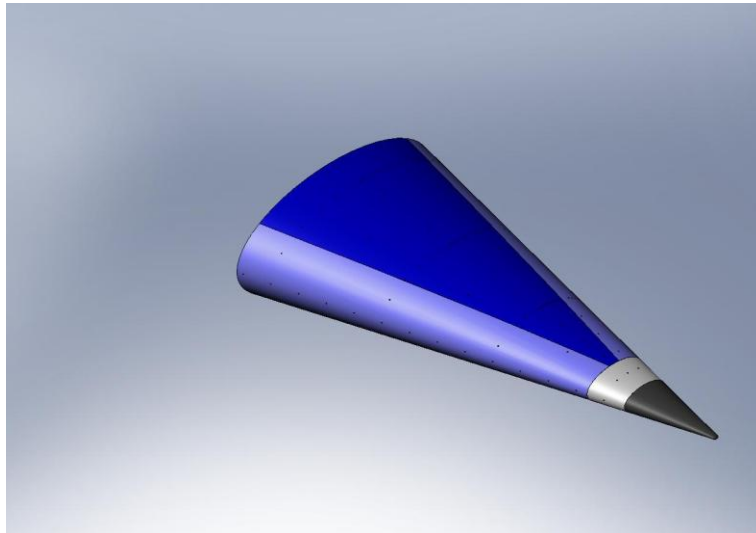
Figure 35 HIFiRE-5 aeroshell construction.

Approved for public release; distribution unlimited.

5. Computation

5.1. Computational Tools

The simulation of boundary layer transition for this work incorporates two tools. The first is the Stability and Transition Analysis for hypersonic Boundary Layers (STABL)[54] software suite. The suite utilizes parabolized stability equations (PSE) to find N factors that represent the exponential growth of naturally-occurring disturbances in the boundary-layer. The PSE solver relies on a laminar mean flow solution to propagate the disturbances through and find their resulting N factors. The N factors can then be compared to experiments and correlations made with the location of transition on the geometry. Again this analysis relies on a quality mean flow solution so care has to be taken to ensure all features of the flow field are captured. This will require a large computational grid and in the past Full Navier-Stokes (FNS) solutions were impractical to simulate. As a result, PNS solvers were used, where the simplification of parabolization of the governing equations reduced the computation time to reasonable levels that computers at the time could handle. With the increase of computer speeds FNS solutions can now be computed in a reasonable time and hence the motivation for this work.

A. US3D – CFD Solver To generate the mean flow solution used for transition analysis, the US3D non-equilibrium solver was used.[55] The solver uses an unstructured finite volume method, incorporating the Stager-Warming flux splitting method with a MUSCL limiter for the invisicid flux calculations. The gas domain was simulated using 5-species air with reaction equations based on Park[56] and Blottner[57] viscosity model.

B. STABL Suite STABL is a suite of software for analyzing the flow over 2D and axi-symmetric geometries.[54]

5.1.1. Mean Flow Solution

A grid resolution study was not conducted, but relied on a study on the previously mentioned study of a sharp elliptic cone and a study conducted by Choudhari et al.[54] who conducted a similar analysis of the HIFiRE-5 vehicle. The grid size used was 450x300x300 (Body Length x Surface Normal x Radial). The same grid was used for all of the cases and a shock fitting algorithm in US3D was used to fit the grid to each flow condition.

Four flight conditions were calculated for a Mach 7 flow at altitudes of 21.8, 25.0, 28.3, and 33.0 km (in the rest of this report only the two leading significant figures will be used to denote each case). The surface temperature was defined using a prescribed temperature for each case based on heat conduction analysis of an estimated trajectory for the vehicle. These results were interpolated onto the grid wall boundary. The solution was run with a max CFL of 10 (due to solution stability reasons) until the nose section's L2 norm residual converged to a small number. The solution at the nose was then "frozen" and the rest of the domain was solved using a CFL of 10,000. Slices of the centerline and leading edge planes were then used to conduct the 2D PSE calculations. Figure 36 shows the density profile contours of the 28km case along slices of the body. We can see a low density region at the centerline and a high density region along the leading edge. Along the centerline a small vortex can be seen forming along the length of the

Approved for public release; distribution unlimited.

body, growing as it travels downstream. This roll up region creates a thicker boundary layer along the centerline compared to an axisymmetric geometry.
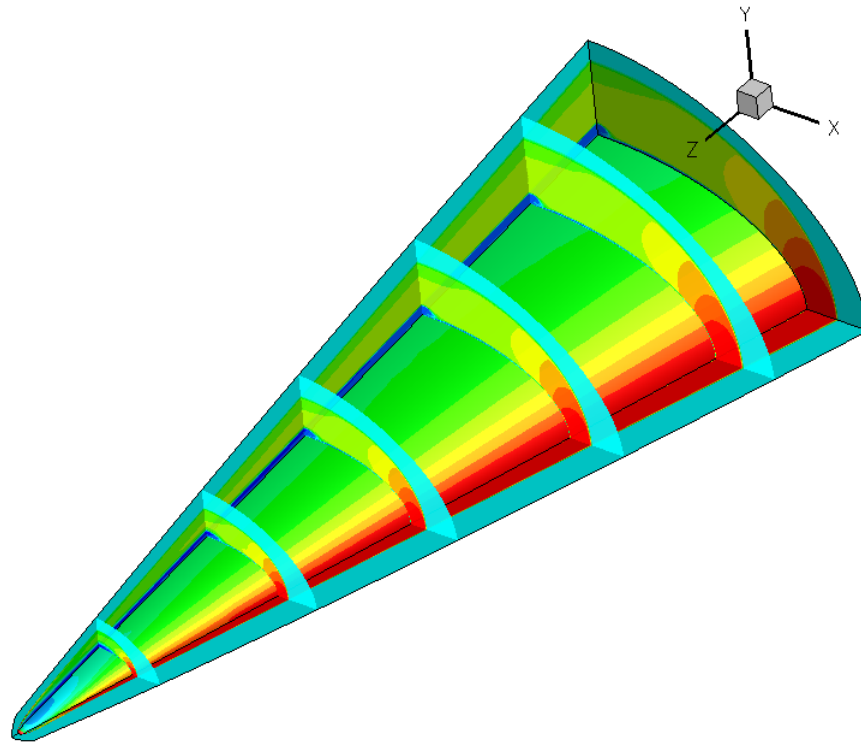
Figure 36 Contour slices of fluid density for 28km case.

Figure 37, Figure 38, Figure 39 and Figure 40 show the boundary layer thickness for each case at three locations along the body length. In the figures, theta denotes the surface location angle in the body width and height plane. So an angle of zero denotes the centerline location and an angle of 90 denotes the leading edge location. The boundary layer is thickest at the centerline where this vortex is formed due to the pressure gradients along the surface. It is interesting that the boundary layer height at the centerline is similar for the four cases at the body length of 0.8 m location.

Figure 37 **Boundary layer thickness at select locations along the length of the body for 21km case. Theta the radial coordinate from 0 (centerline) to 90 (leading edge).**

Figure 38 **Boundary layer thickness at select locations along the length of the body for 25km case. Theta the radial coordinate from 0 (centerline) to 90 (leading edge).**
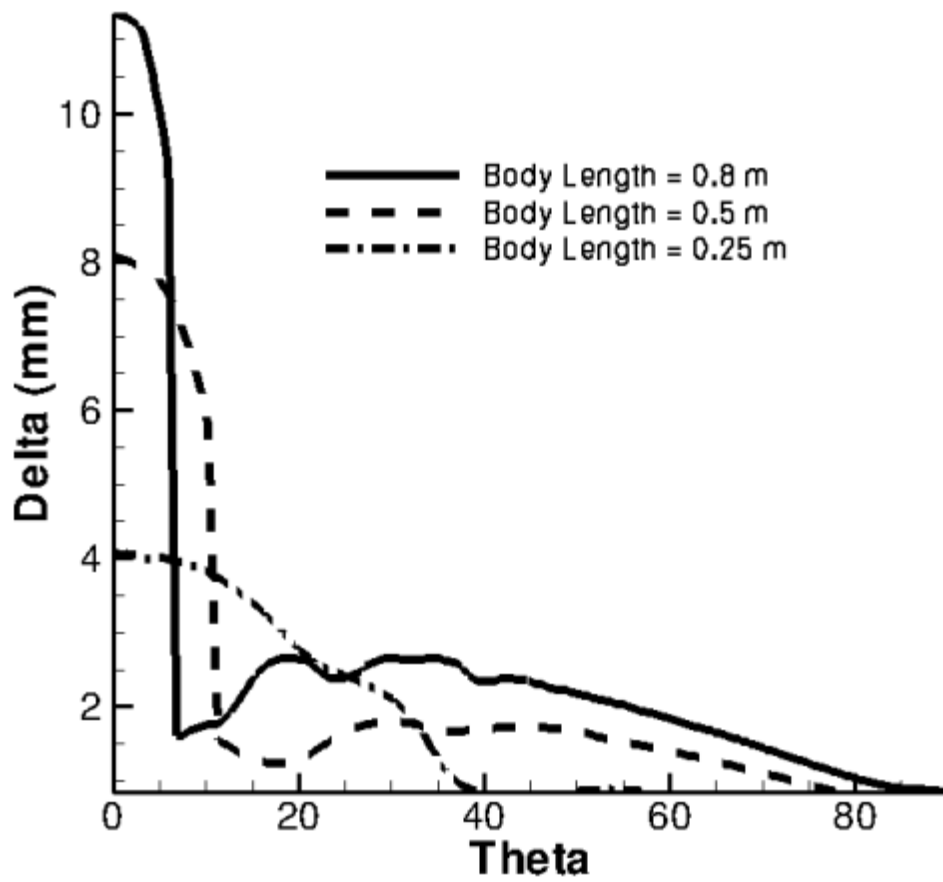
Figure 39 Boundary layer thickness at select locations along the length of the body for 28km case. Theta the radial coordinate from 0 (centerline) to 90 (leading edge).
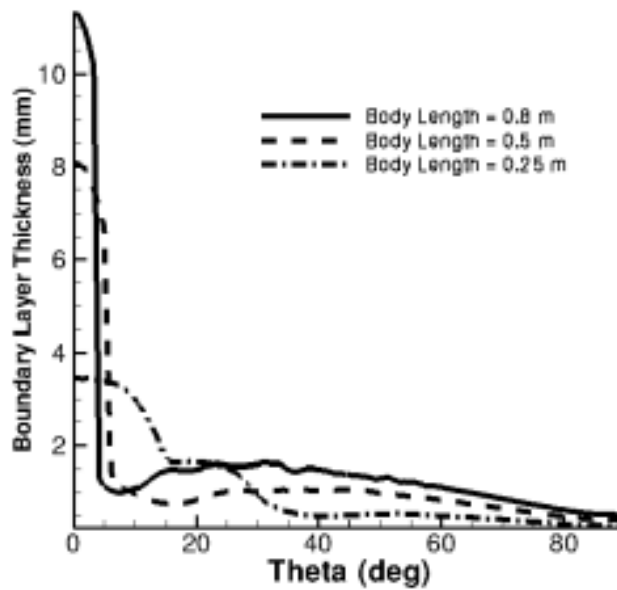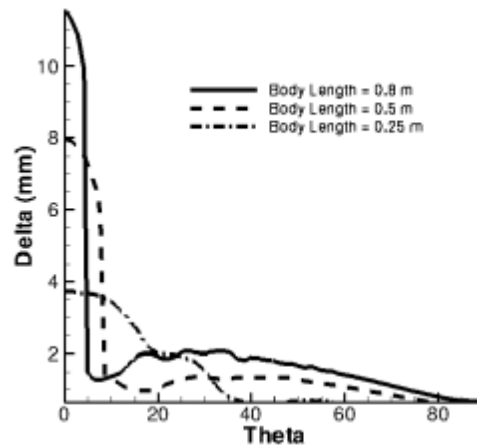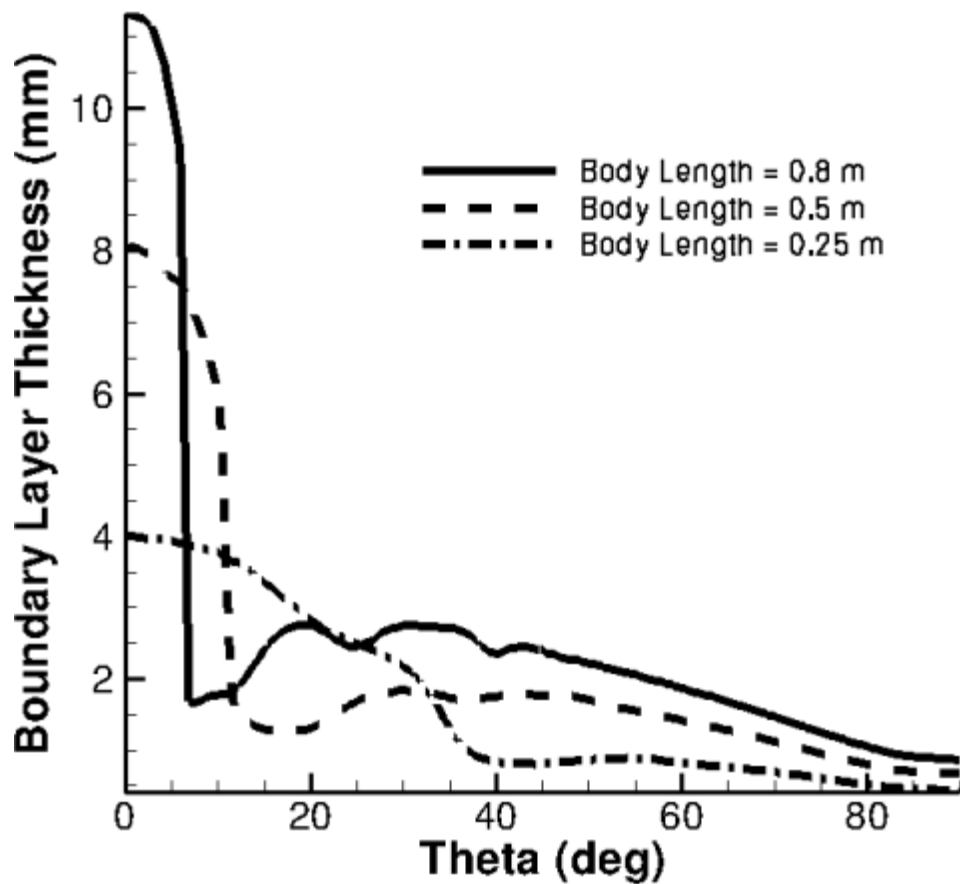
Figure 40 Boundary layer thickness at select locations along the length of the body for 33km case. Theta the radial coordinate from 0 (centerline) to 90 (leading edge).

To better understand the development of the boundary layer, Figure 41 and Figure 42 show contours of the density for the 28km and 21km cases respectively. The plots are a close up of the roll up region on a plane at the 0.8 m location along the body length. Comparing between the two figures, both structures have similar heights at the centerline. The shape of the vortex region stands out as the most different. For the 21km case, the region is more developed and shows a deeper penetration of the fluid being entrained towards the centerline. This makes the boundary layer height in Figure 37 decrease more rapidly. Looking upstream, similar comparison to the development of the vortex can be seen.

Figure 41 Density contour at x = 0.80 m plane for 21 km case.

Figure 42 Density contour at x = 0.80 m plane for 28 km case.

Figure 43 Density contour at x = 0.53 m plane for 21 km case.
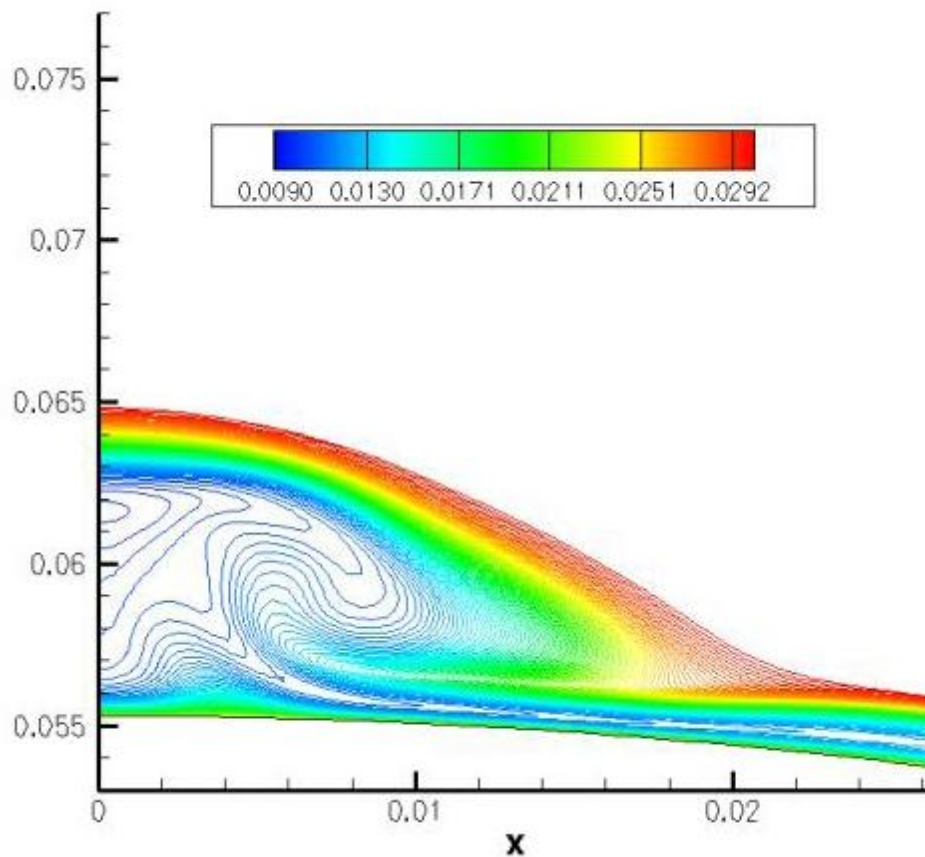
Figure 44 Density contour at x = 0.53 m plane for 28 km case.

Figure 43 and Figure 44 show the body length location of 0.53 m. Figure 45 and Figure 46 show the body length location of 0.23 m. In both cases the vortex looks to be more developed for the higher Reynold's number flow as to be expected. It is i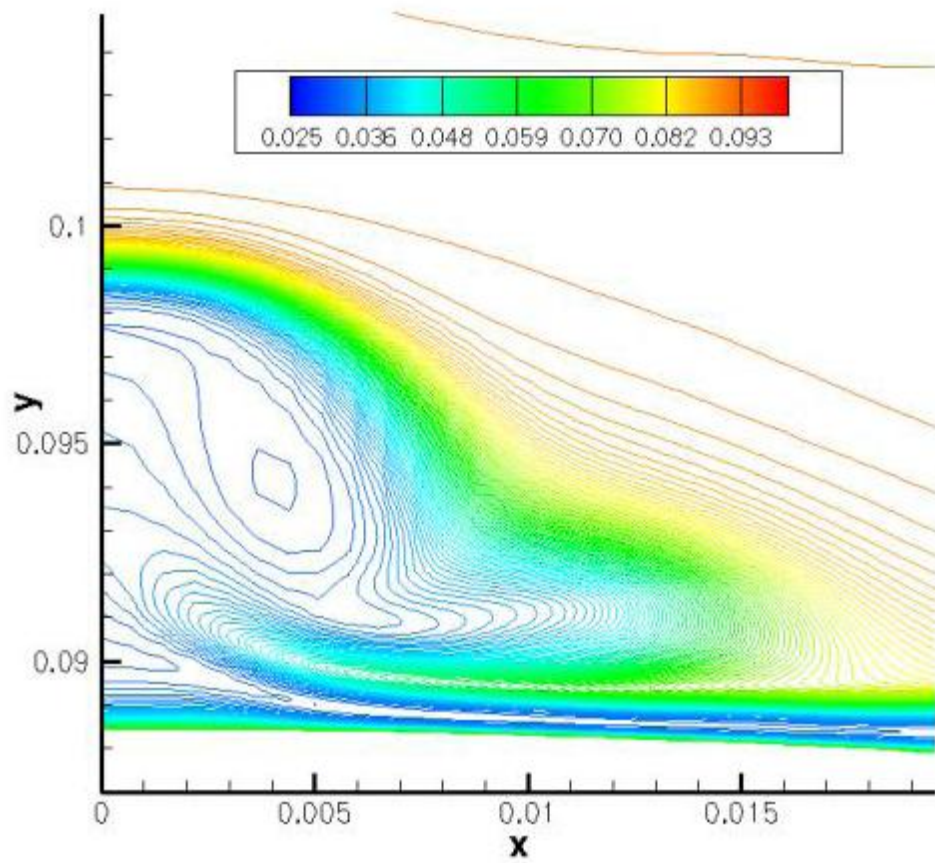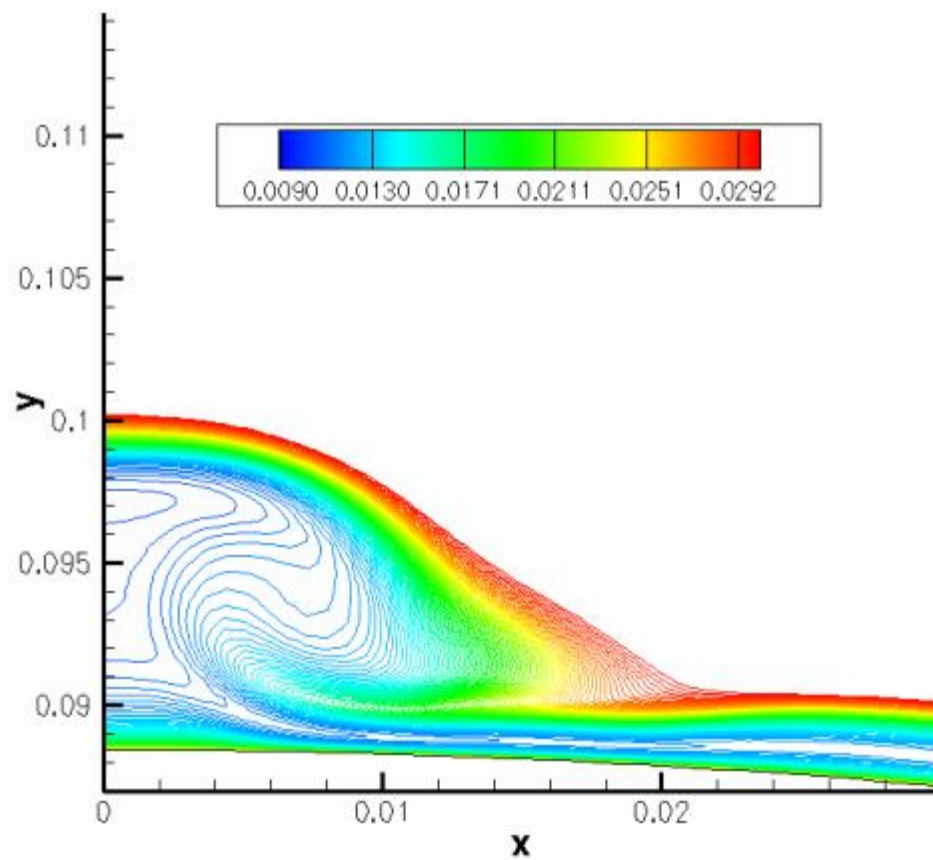nteresting how the vortex structure size stays somewhat similar. Figure 47, Figure 48, Figure 49 and Figure 50 show the boundary layer edge velocity streamlines and all four compare closely to the trends of a pressure gradient driving the flow to the centerline symmetry plane. To better understand the flow the maximum cross flow velocity is used. This cross flow is defined by taking the projection of the boundary layer velocity onto the normal vector of the boundary layer edge velocity. Figure 51, Figure 52, Figure 53 and Figure 54 show contours of the maximum crossflow velocity divided by the magnitude of the edge velocity of the boundary layer.   All four figures show a large normalized maximum crossflow velocity a small distance downstream of the nose region. There is a slight increase on the normalized maximum crossflow velocity with decreasing altitude. Another way of presenting the maximum crossflow is by that of the conventional crossflow Reynolds number Re_{cf} ($w_{max} \delta_{10}/\nu_e$). Figure 55, Figure 56, Figure 57 and Figure 58 show the crossflow Reynolds number over the surface of the vehicle. As expected we see the value increasing with decreasing altitude.
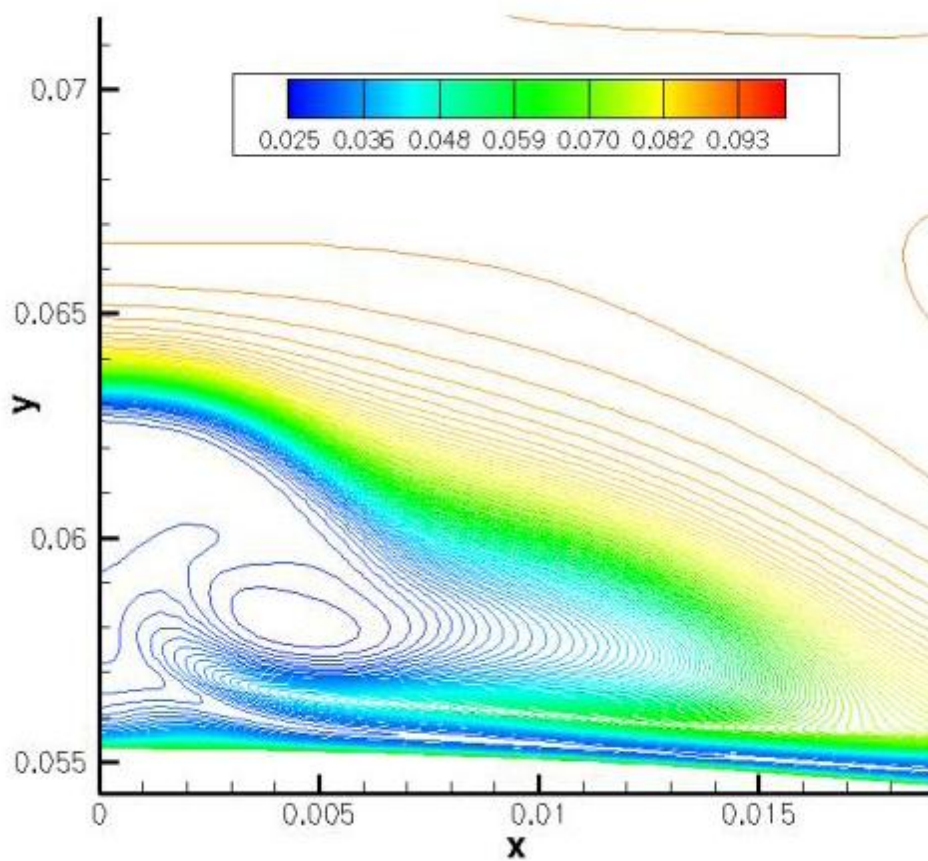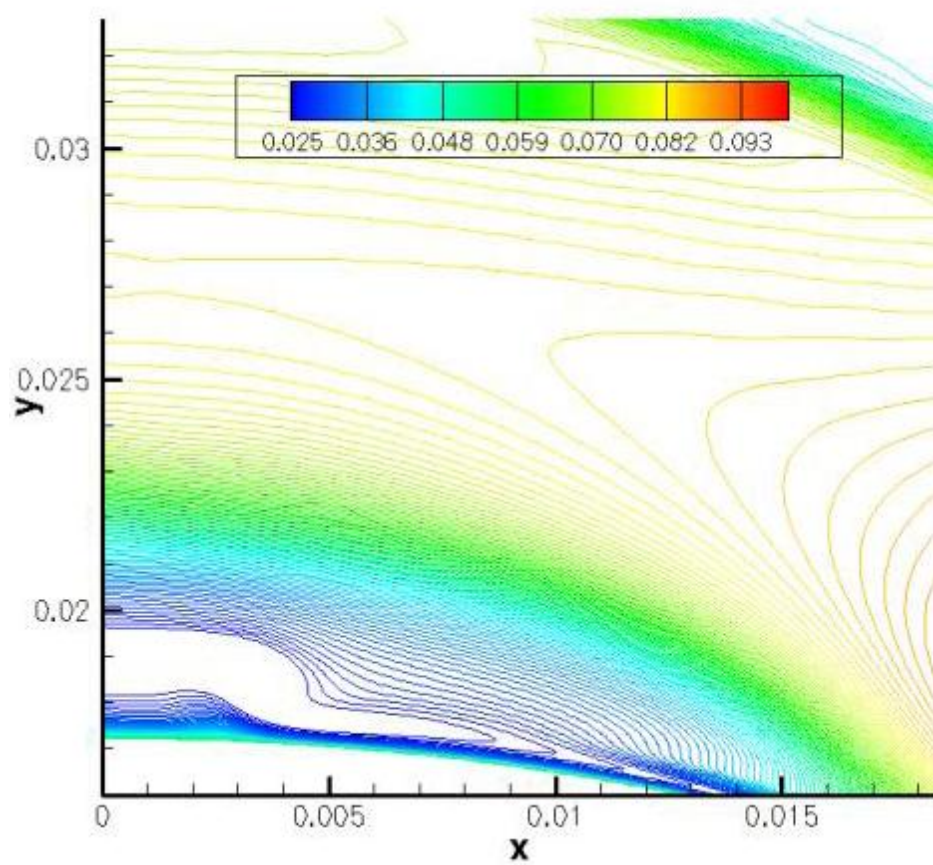
Figure 45 Density contour at x = 0.23 m plane for 21 km case.
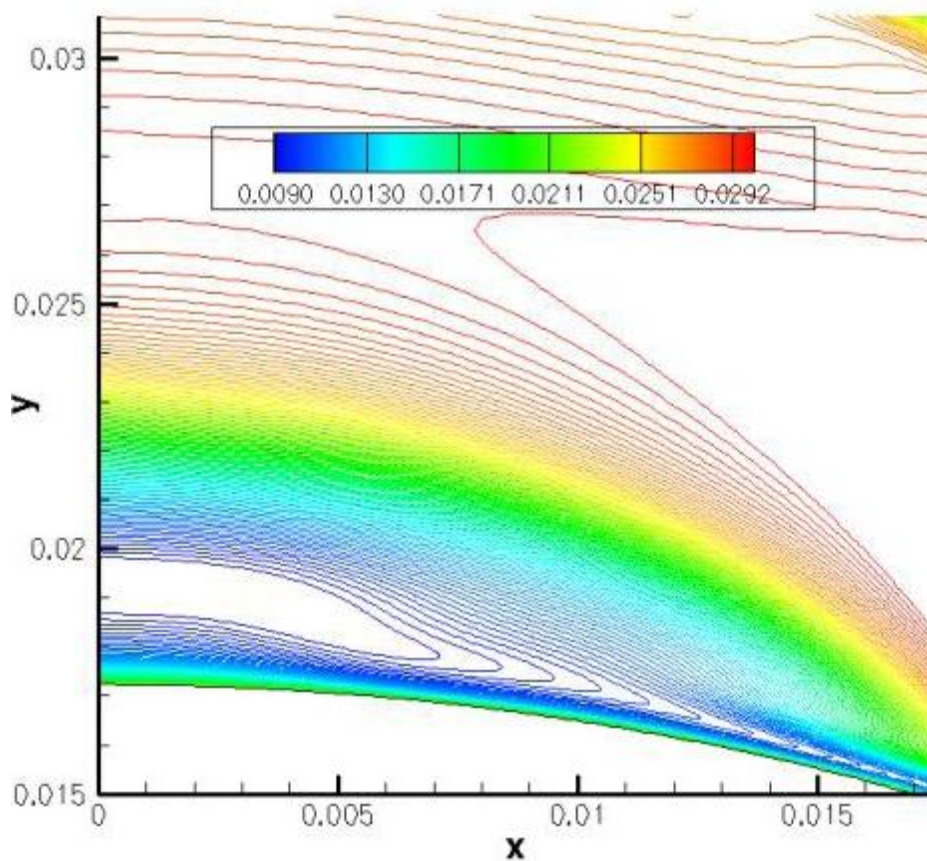
Figure 46 Density contour at x = 0.23 m plane for 28 km case.
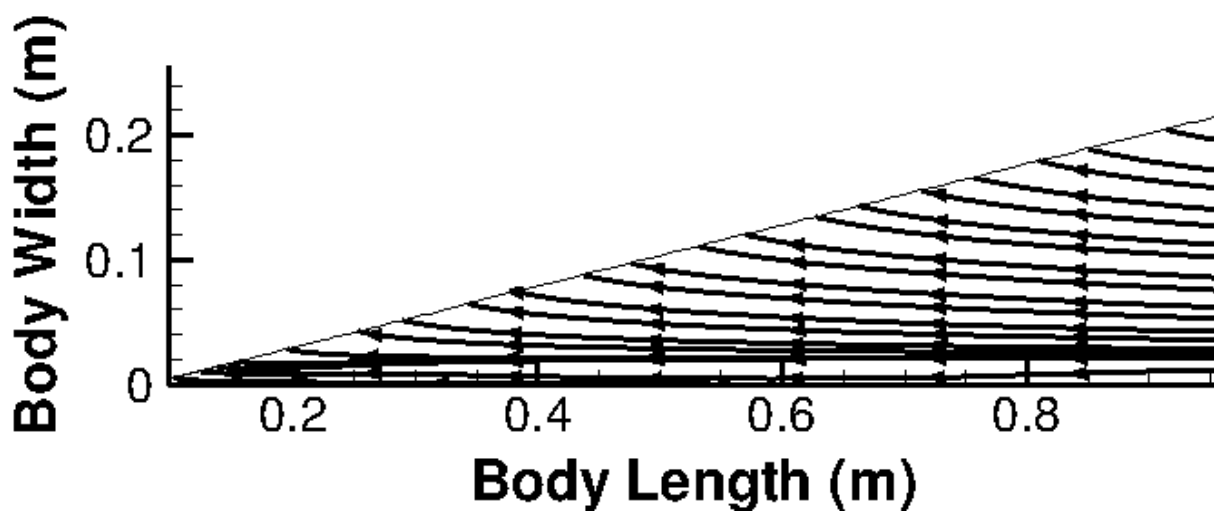
Figure 47 Boundary layer edge streamlines for 21 km case.
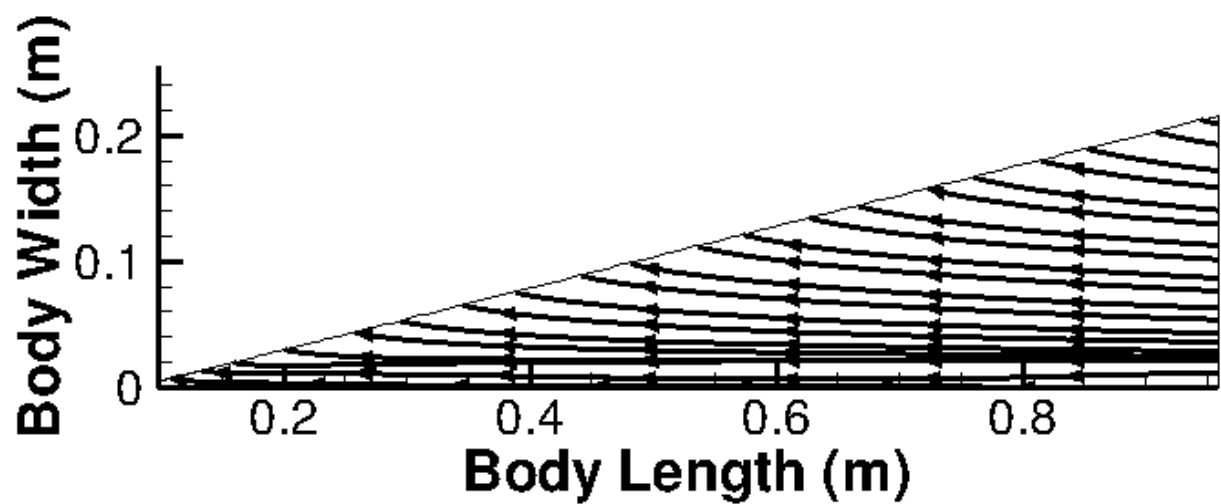
Figure 48 Boundary layer edge streamlines for 25 km case.
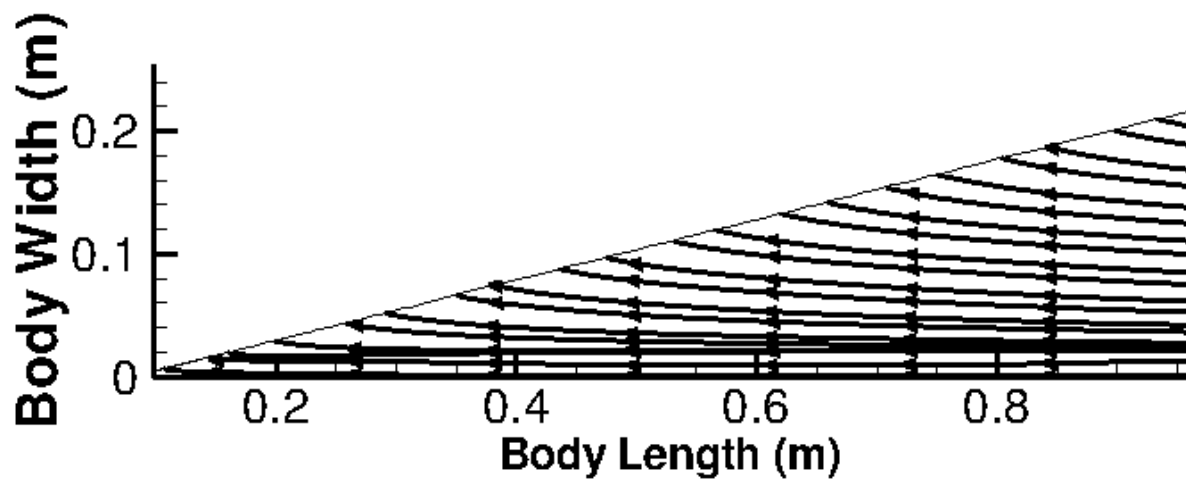
Figure 49 Boundary layer edge streamlines for 28 km case.
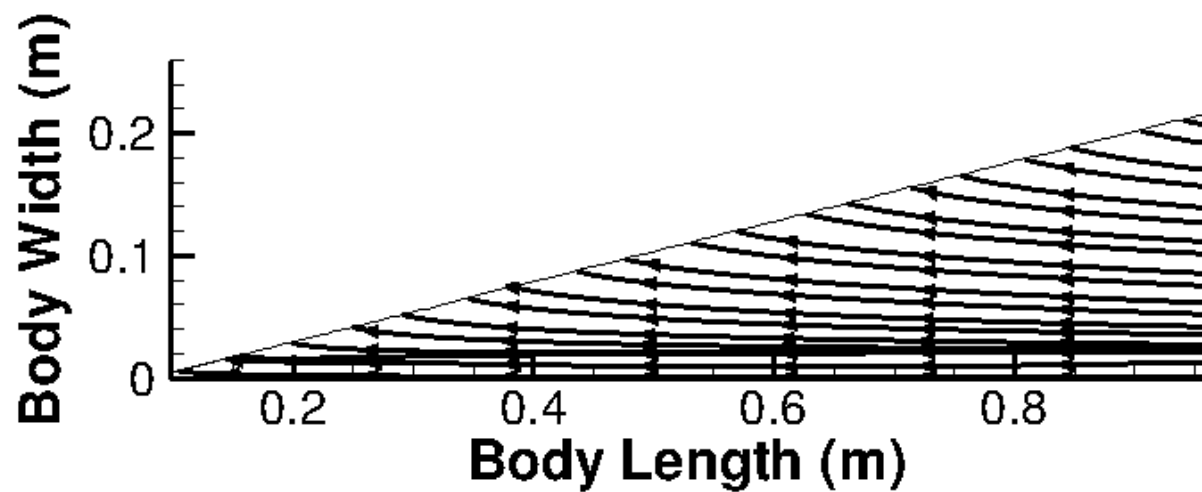
Figure 50 Boundary layer edge streamlines for 33 km case
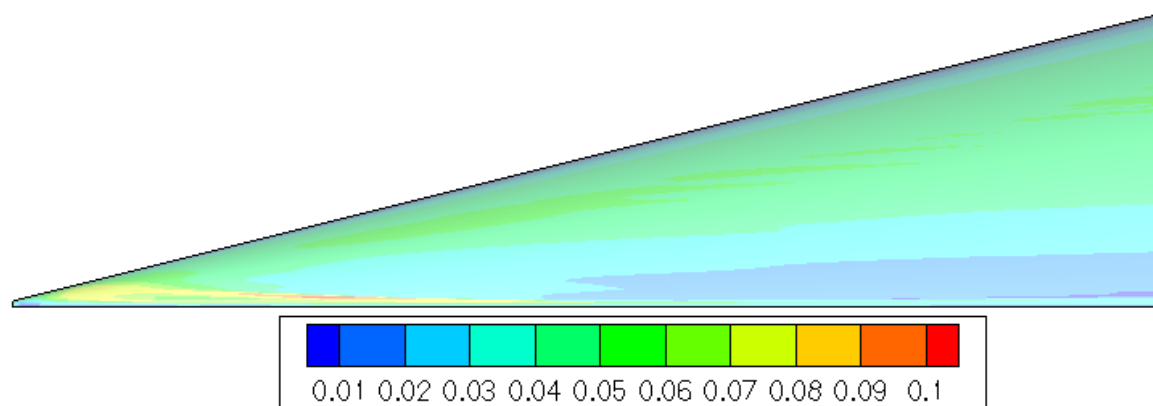
Figure 51 Maximum crossflow velocity contours for 21 km case.
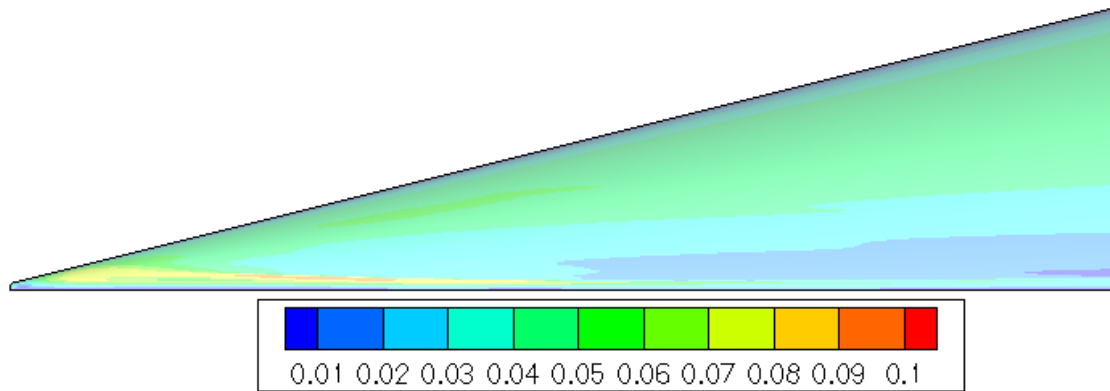
Figure 52 Maximum crossflow velocity contours for 25 km case.
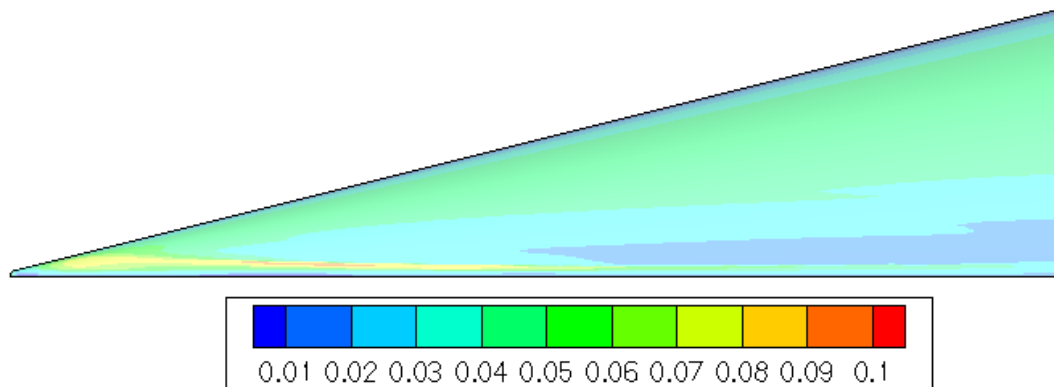
Figure 53 Maximum crossflow velocity contours for 28 km case.
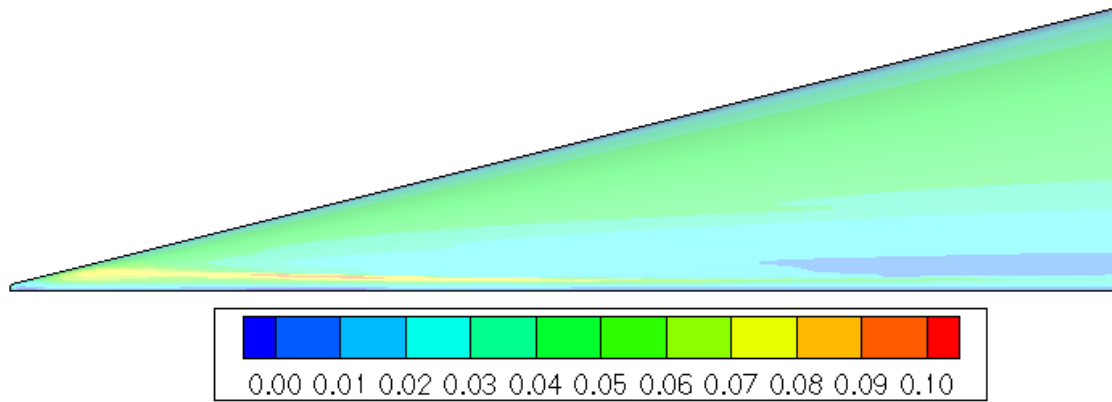
Figure 54 Maximum crossflow velocity contours for 33 km case.
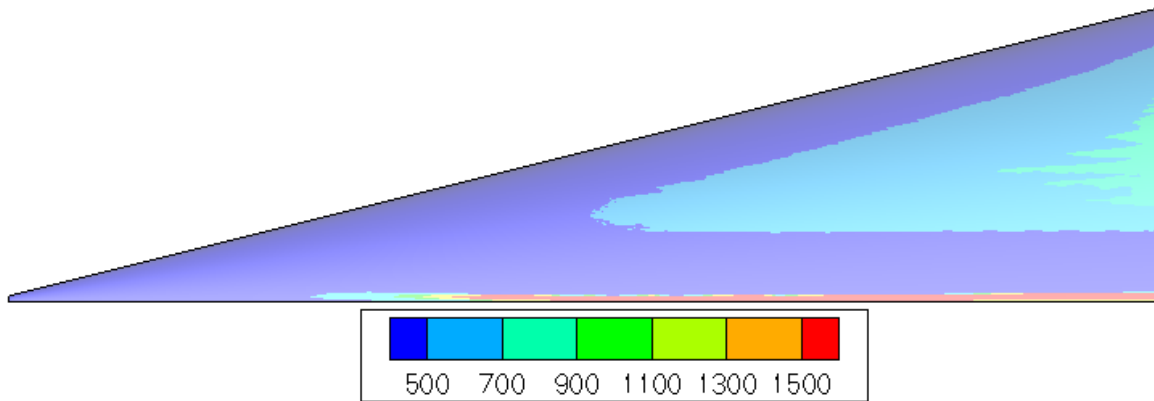
Figure 55 Crossflow Reynolds number contours for 21km case
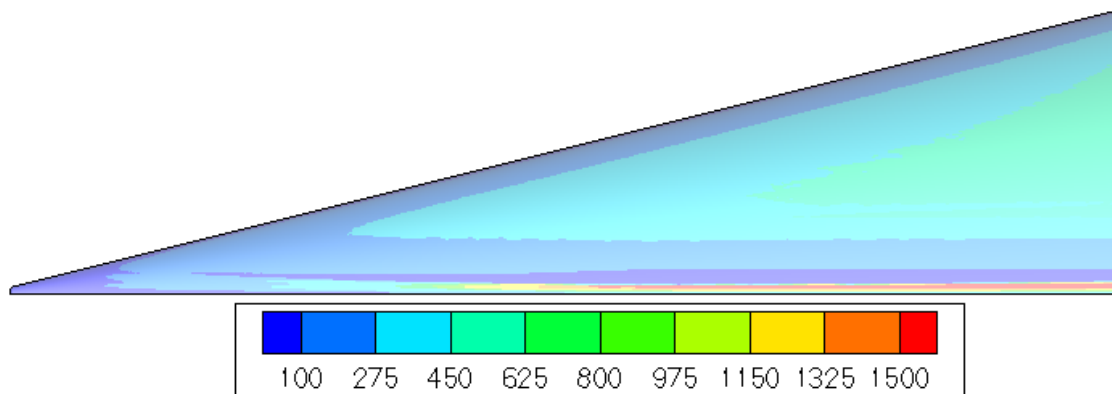
Figure 56 Crossflow Reynolds number contours for 25km case
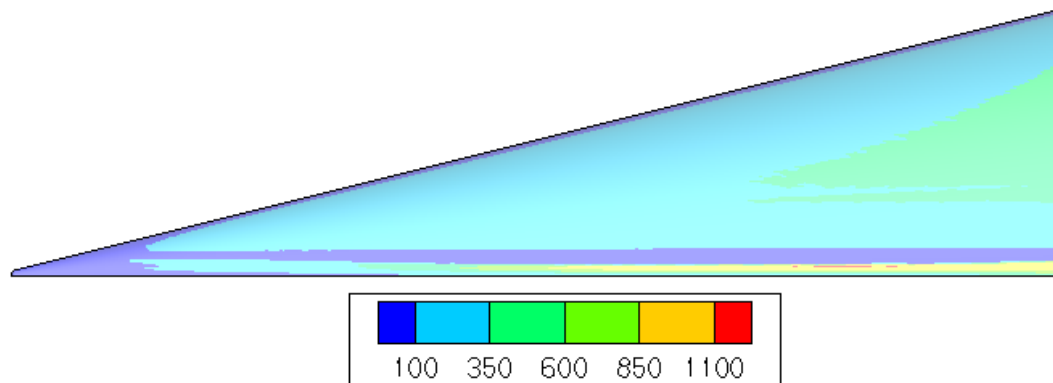
Figure 57 Crossflow Reynolds number contours for 28km case
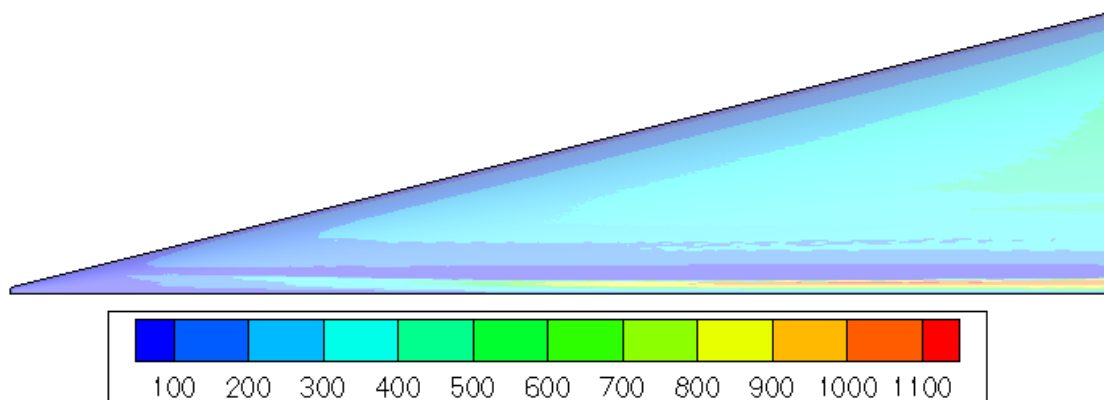
Figure 58 Crossflow Reynolds number contours for 33 km case

5.1.2. PSE Results

The centerline and leading edge plane CFD solutions were provided as input for stability analyses. The STABL suite was used for the calculations. The PSE solver built into STABL is currently only capable of analyzing two dimensional flows. Hence only the centerline and leading edge planes were examined. The PSE solver evaluates a range of instability frequencies and outputs the growth of the frequencies along the length of the geometry in the form of an N factor. Figures 24 and 25 show the maximum N factor over the length of the geometry for the leading edge and centerline. Traditionally for 2D flows, the N factor will correlate to a transition location. As a rule of thumb for free flight, an N factor of approximately 11 indicates the location of expected transition. Looking at the leading edge cases, the 28 and 33km cases show similar growth of N factors and indicate that boundary layer transition may not occur at those altitudes using the N =11 transition estimation. The other two cases reach N factors much larger than 11 and suggest that transition will occur. For the centerline cases, the PSE results show an N factor growth that is very similar for the 25, 28, and 33km cases. The 21km case is very different and shows a significantly larger growth in N over the body length.
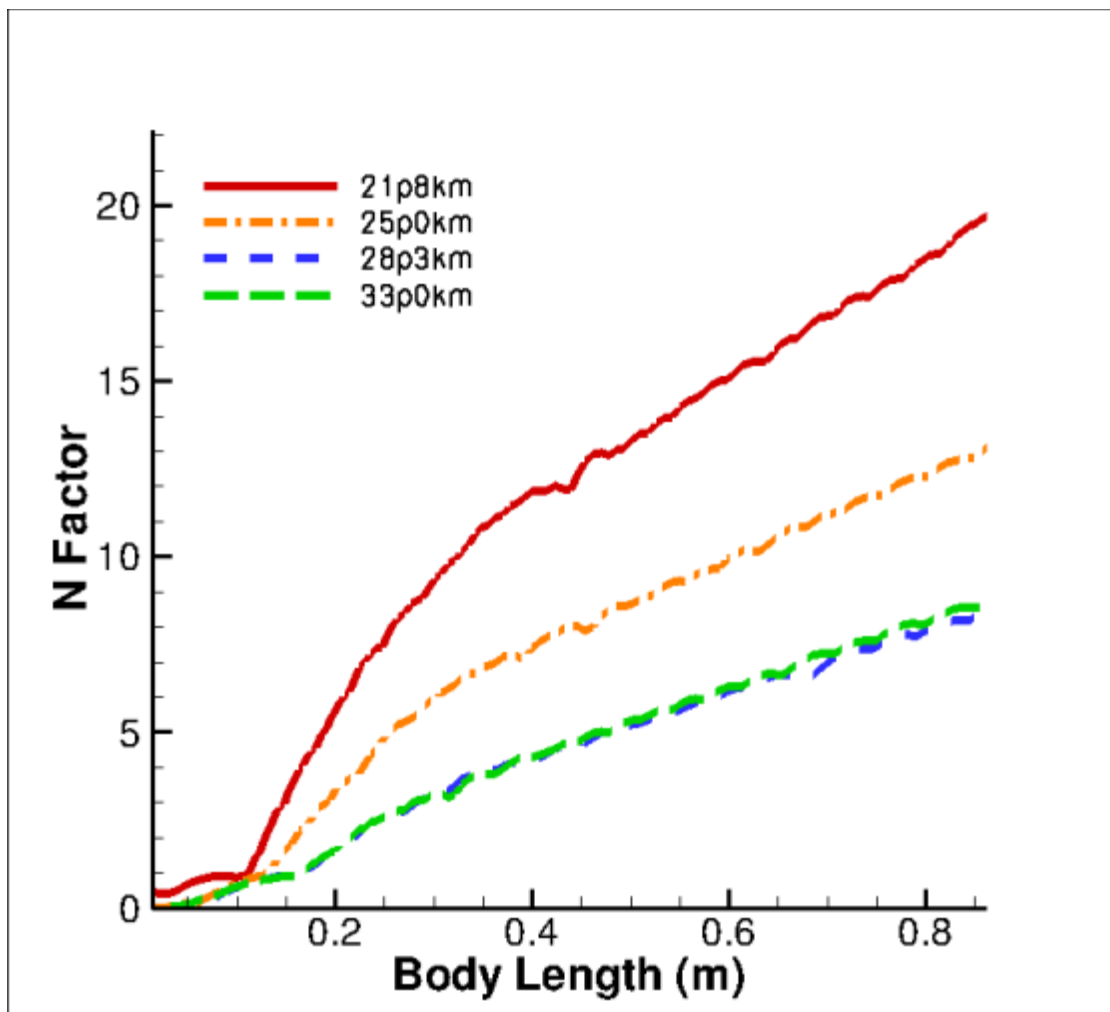
Figure 59 Maximum N-factor along leading edge for all cases
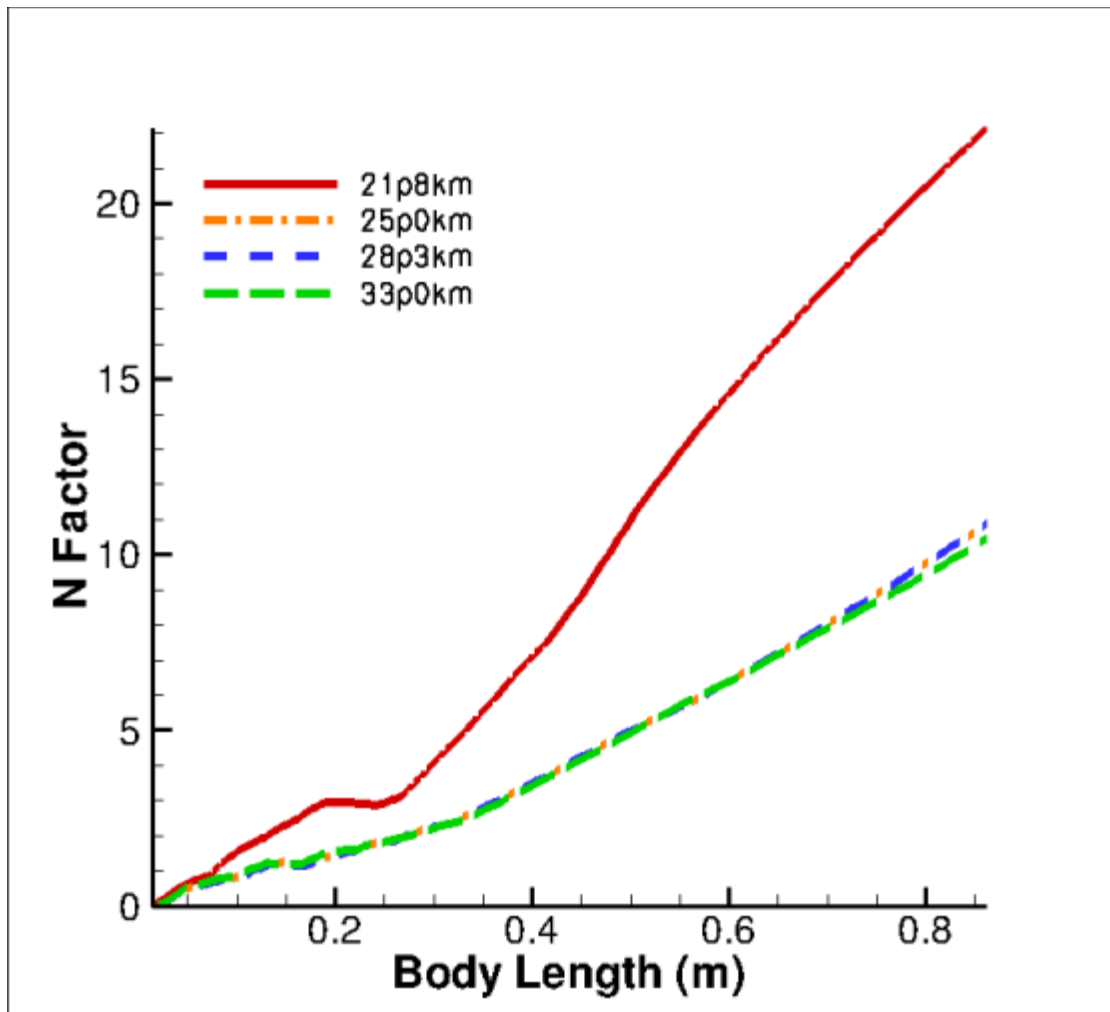
Figure 60 Maximum N-factor along centerline for all cases

Figure 61, Figure 62, Figure 63 and Figure 64 show the Linear Stability (LST) diagram for each of the cases analyzed along the leading edge. The contour plot represents the growth rate of instabilities as found from LST analysis. The colored lines represent the estimated first, second, and higher mode disturbance frequencies. Each figure shows a tight band of frequency growth that follows close to the 2nd mode estimation. The black line denotes the maximum N factor frequency as calculated by the PSE equations. The line closely follows the upper limit of the linear frequency growth band. The results of the PSE analysis are shown in Figure 65, Figure 66, Figure 67 and Figure 68. Comparing these plots to the LST diagrams we can gain some insight into the stability of this slice of the boundary layer. From the PSE analysis, the frequencies which produce the largest N factor at any surface location are also plotted on each figure. Looking at the maximum N factor growth we see that the largest N factors are produced by disturbances passing through this band of unstable second-mode frequencies. These are seen in Figures Figure 65 - Figure 68 as the black N factor lines which start at around 0.2 m and which experience amplification as they continue downstream. The 21km case shows growth in a 1000-3000 kHz range and the 33km case shows growth in the 700-1750 kHz range. Referring

back to Figure 60, we saw that the N factor growth was similar for all cases except for the 21.8km altitude.
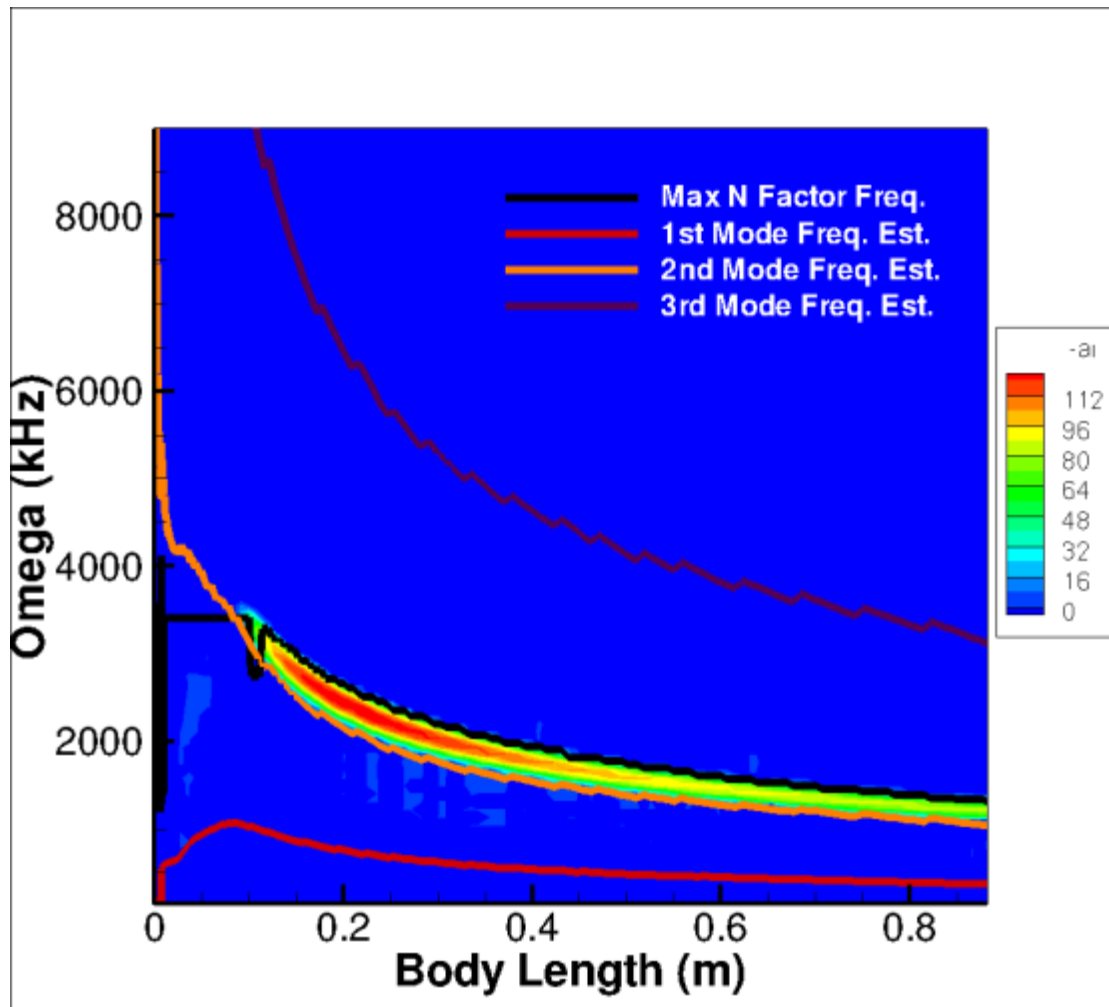
Figure 61 LST stability diagram for 21 km leading edge plane. Max N factor frequencies (black). 1st Mode frequency estimate (orange). 2nd mode frequency estimate (red) 3rd mode frequency estimate (purple).
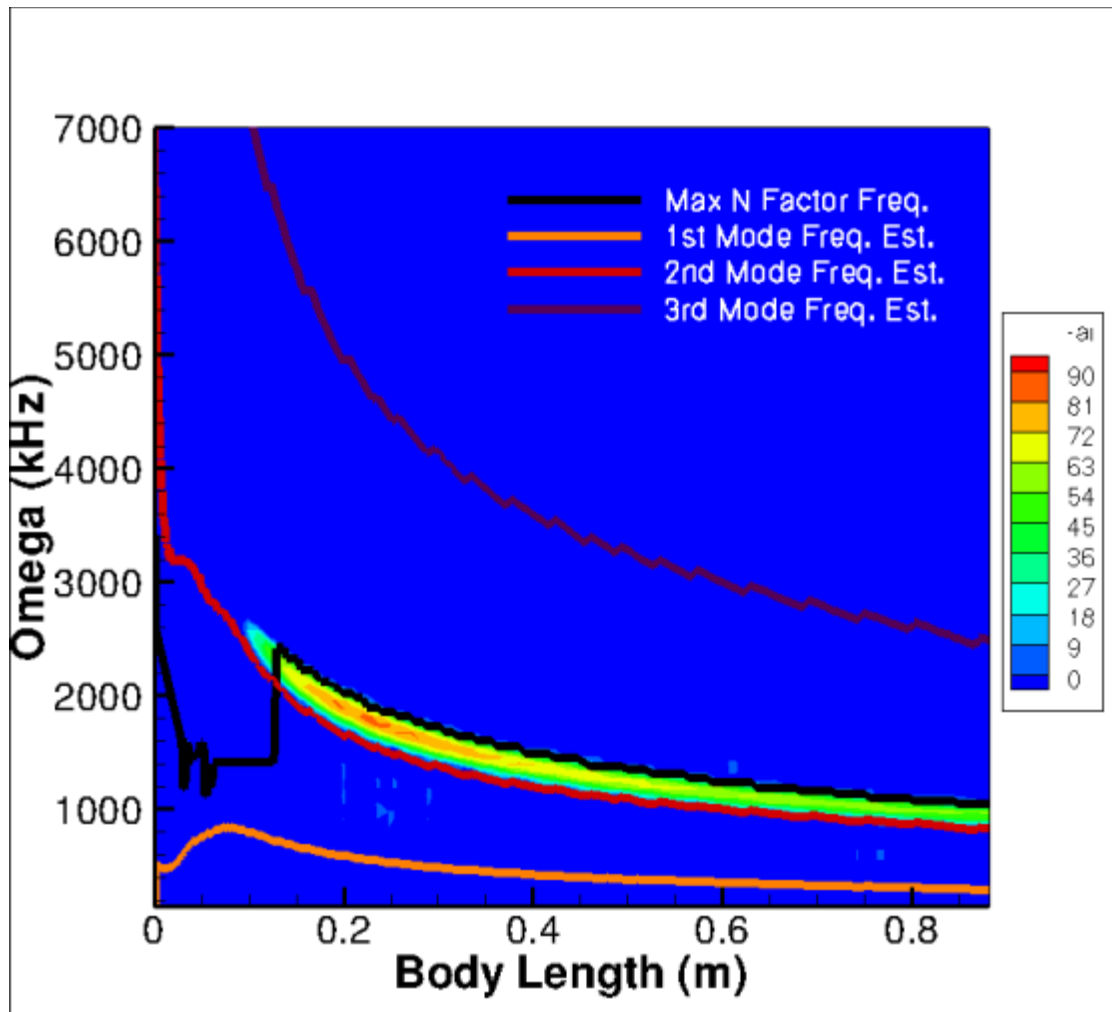
Figure 62 LST stability diagram for 25 km leading edge plane. Max N factor frequencies (black). 1st Mode frequency estimate (orange). 2nd mode frequency estimate (red) 3rd mode frequency estimate (purple).

Figure 63 LST stability diagram for 28 km leading edge plane. Max N factor frequencies (black). 1st Mode frequency estimate (orange). 2nd mode frequency estimate (red) 3rd mode frequency estimate (purple).

Figure 64 LST stability diagram for 33 km leading edge plane. Max N factor frequencies (black). 1st Mode frequency estimate (orange). 2nd mode frequency estimate (red) 3rd mode frequency estimate (purple).
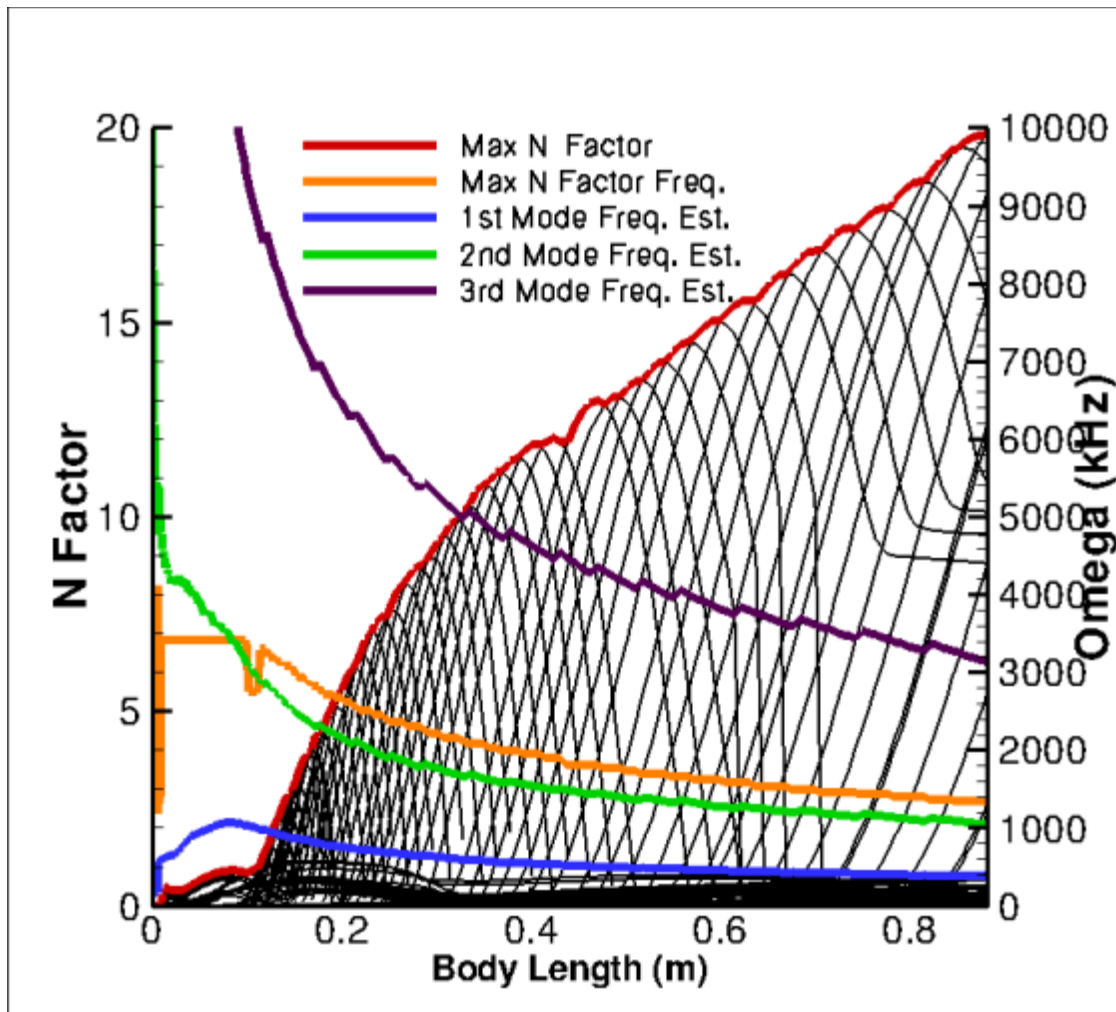
Figure 65 Boundary layer stability results for 21 km case leading edge plane. N factors of calculated frequencies using STABL (black). Max N factor line (red). Max N factor frequencies (orange). 1st Mode frequency estimate (blue). 2nd mode frequency estimate (green). 3rd mode frequency estimate (purple).
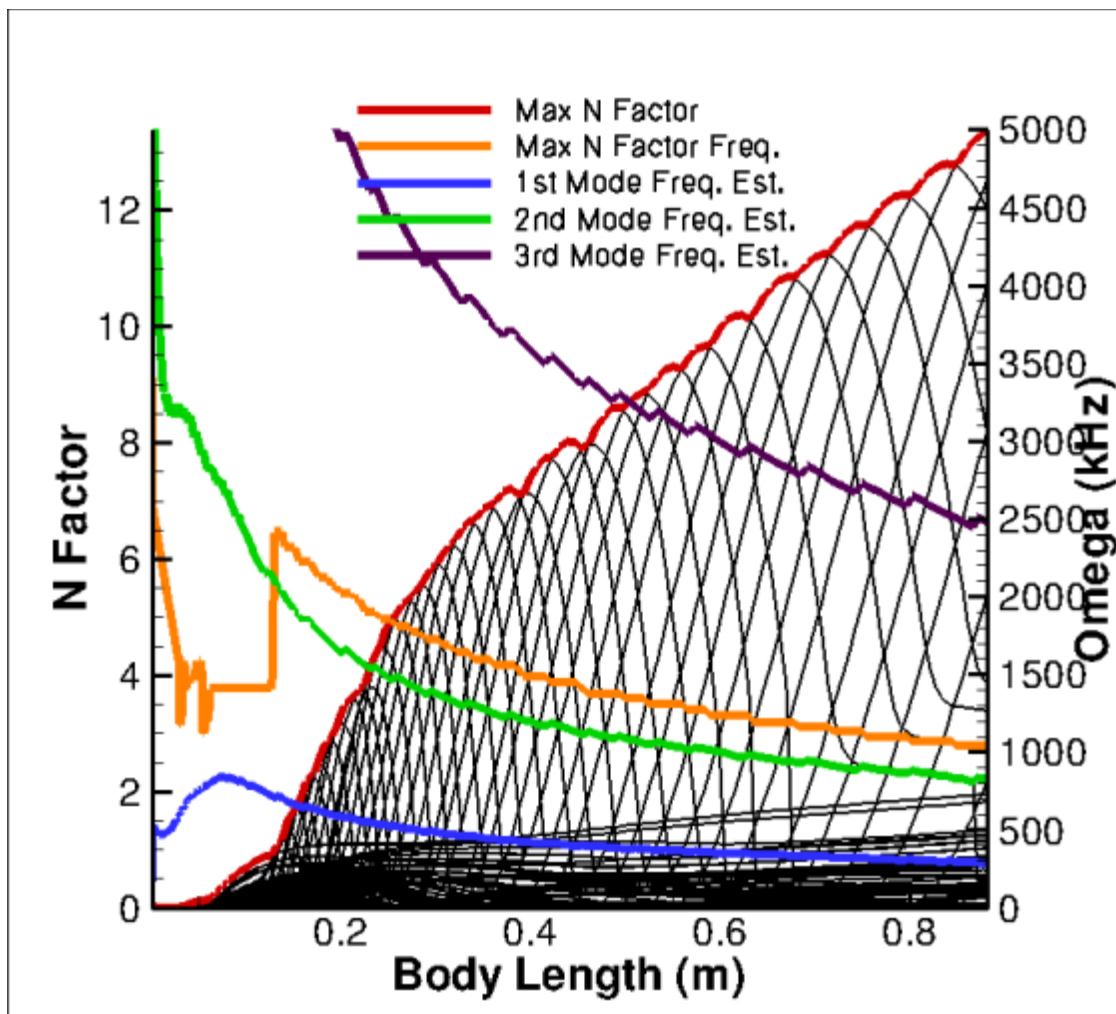
Figure 66 Boundary layer stability results for 25 km case leading edge plane. N factors of calculated frequencies using STABL (black). Max N factor line (red). Max N factor frequencies (orange). 1st Mode frequency estimate (blue). 2nd mode frequency estimate (green). 3rd mode frequency estimate (purple).
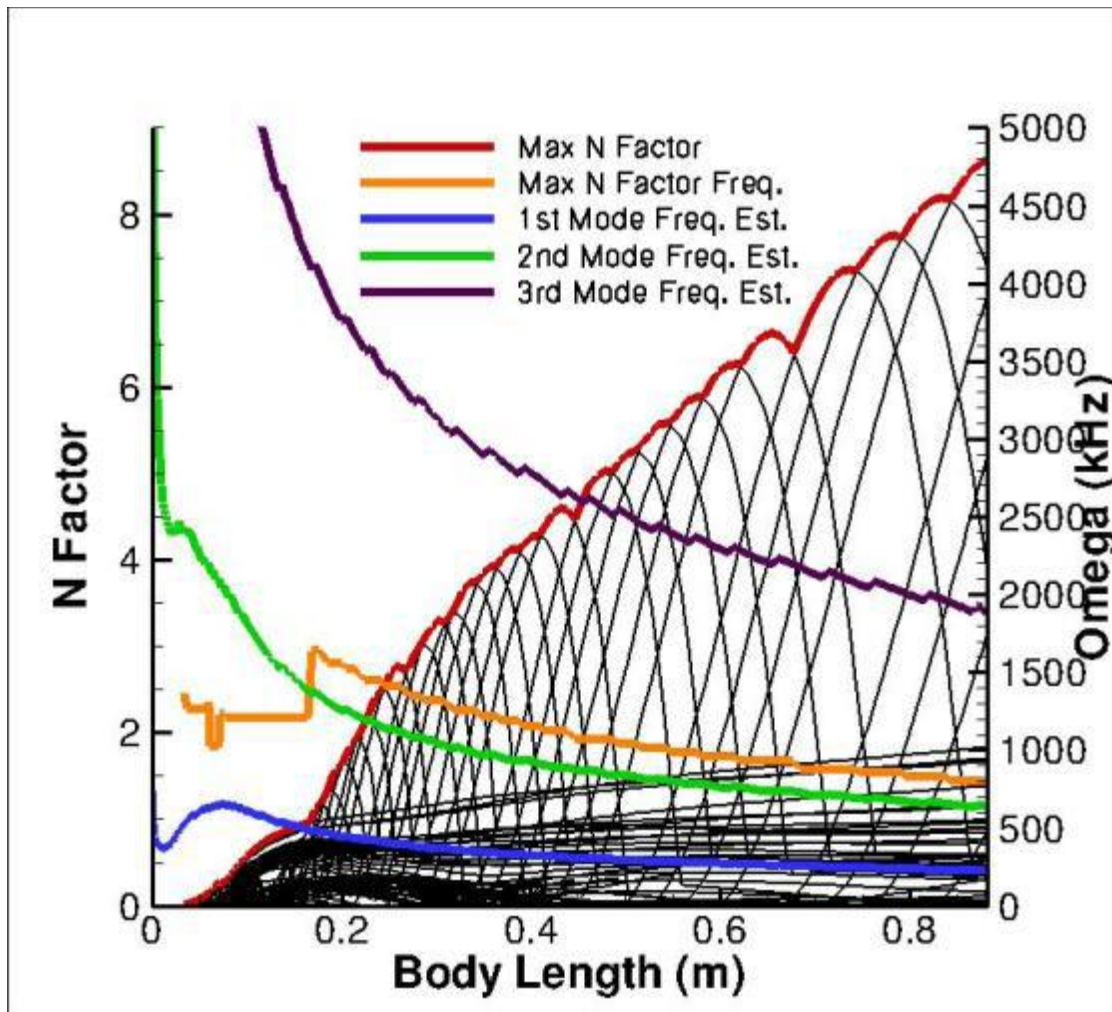
Figure 67 Boundary layer stability results for 28 km case leading edge plane. N factors of calculated frequencies using STABL (black). Max N factor line (red). Max N factor frequencies (orange). 1st Mode frequency estimate (blue). 2nd mode frequency estimate (green). 3rd mode frequency estimate (purple).
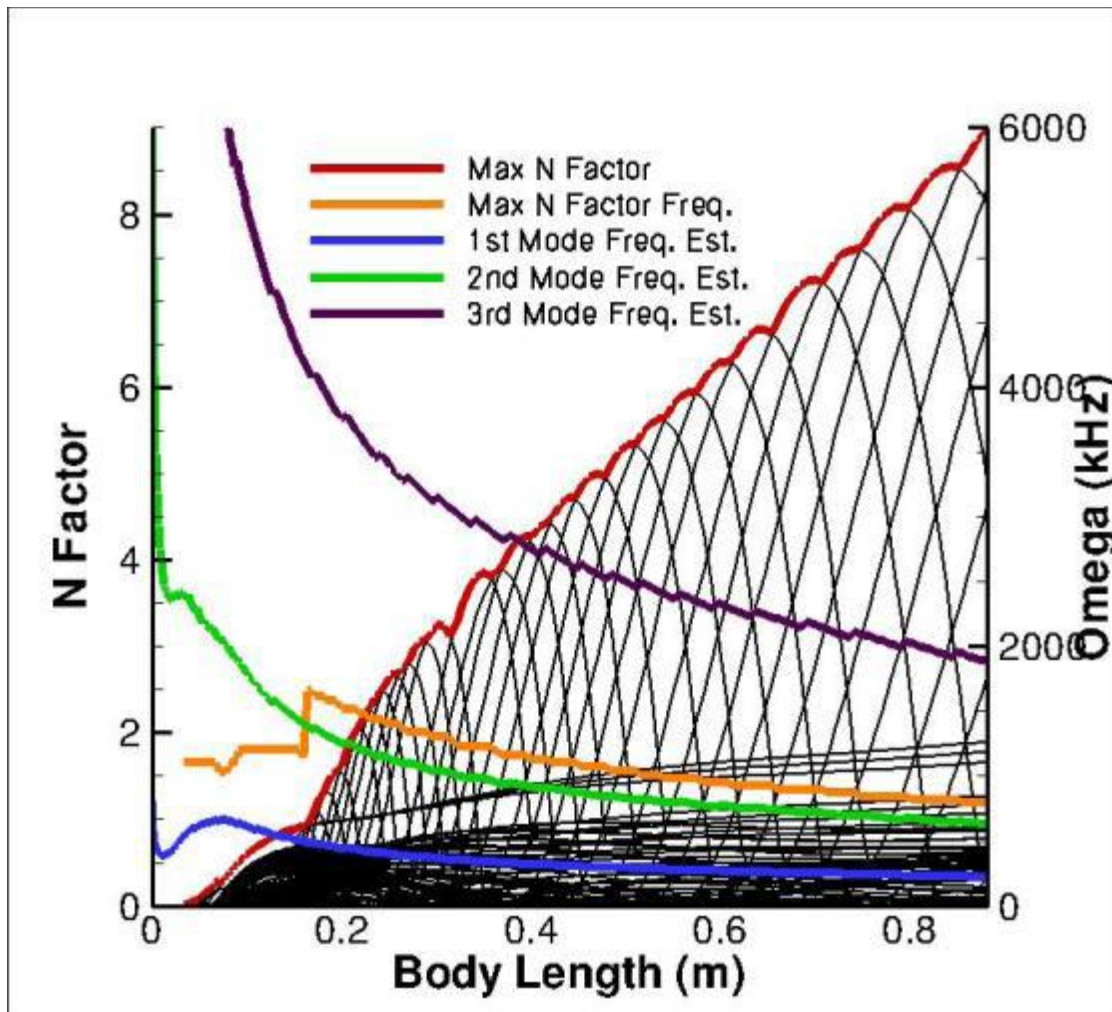
Figure 68 Boundary layer stability results for 33 km case leading edge plane. N factors of calculated frequencies using STABL (black). Max N factor line (red). Max N factor frequencies (orange). 1st Mode frequency estimate (blue). 2nd mode frequency estimate (green). 3rd mode frequency estimate (purple).

Figure 69, Figure 70, Figure 71 and Figure 72 show the LST diagram for each case and Figure 73, Figure 74, Figure 75 and Figure 76 show the results of the PSE analysis. As expected from inspecting Figure 60, the results for the 25, 28, and 33 km cases are very similar. For brevity only the 33 km case will be discussed. Figure 72 shows the LST diagram for the 33 km case, analyzed along the centerline. Also on the figure are the lines showing the estimated first, second, and higher mode disturbance frequencies. The diagram shows a large band of unstable frequencies which are nearly constant starting from about 0.2 m and extending down the length of the body. The estimate indicates that these are the second mode frequencies. Below this band we see a range of unstable first mode frequencies and above it, a range of unstable higher mode frequencies. The results of the PSE analysis are shown in Figure 76. By looking at these figures together we can gain some insight into the stability of this slice of the boundary layer. From the PSE analysis, the frequencies which produce the largest N factor at any surface location are also plotted on each figure. Looking at Figure 72 we see that the largest N factors are produced by

Approved for public release; distribution unlimited.

disturbances passing through this band of unstable second-mode frequencies in the range of 50-100 kHz. These are seen in Figure 76 as the black N factor lines which start at around 0.2 m and which experience amplification as they continue downstream. An eigenfunction analysis was performed for the disturbance in the frequency range of 50-100 kHz which produces the largest N factors. The results of this analysis confirm that these are indeed second mode disturbances as indicated by the characteristic shape of the temperature fluctuation and the phase change indicated in the pressure disturbance eigenfunction. The prominent band of unstable higher-frequency disturbances is present in the stability diagram as a result of the upwelling flow on the centerline and the effect that it has on the boundary layer profile. The effect is more dramatic at the 21 km flight as seen in Figure 73 giving hint to the differences seen in the maximum N factor shown in Figure 60. The quality of Figure 65 could be cleaned up with an LST analysis with a higher resolution of test points. Still it is sufficient to illustrate the effect of the boundary layer profile. In this figure we see that the two bands of unstable disturbances – the second mode and the higher-frequency disturbances have begun to merge. The estimate for the first mode disturbance frequency, which is based only on boundary layer edge conditions and the boundary layer thickness, shows a smoothly-decreasing frequency. The estimate for second and higher modes, which is based on an integrated time of travel of disturbance waves in the boundary layer, shows a large jump to higher frequencies. This can be understood by looking at typical boundary layer profiles in this region.
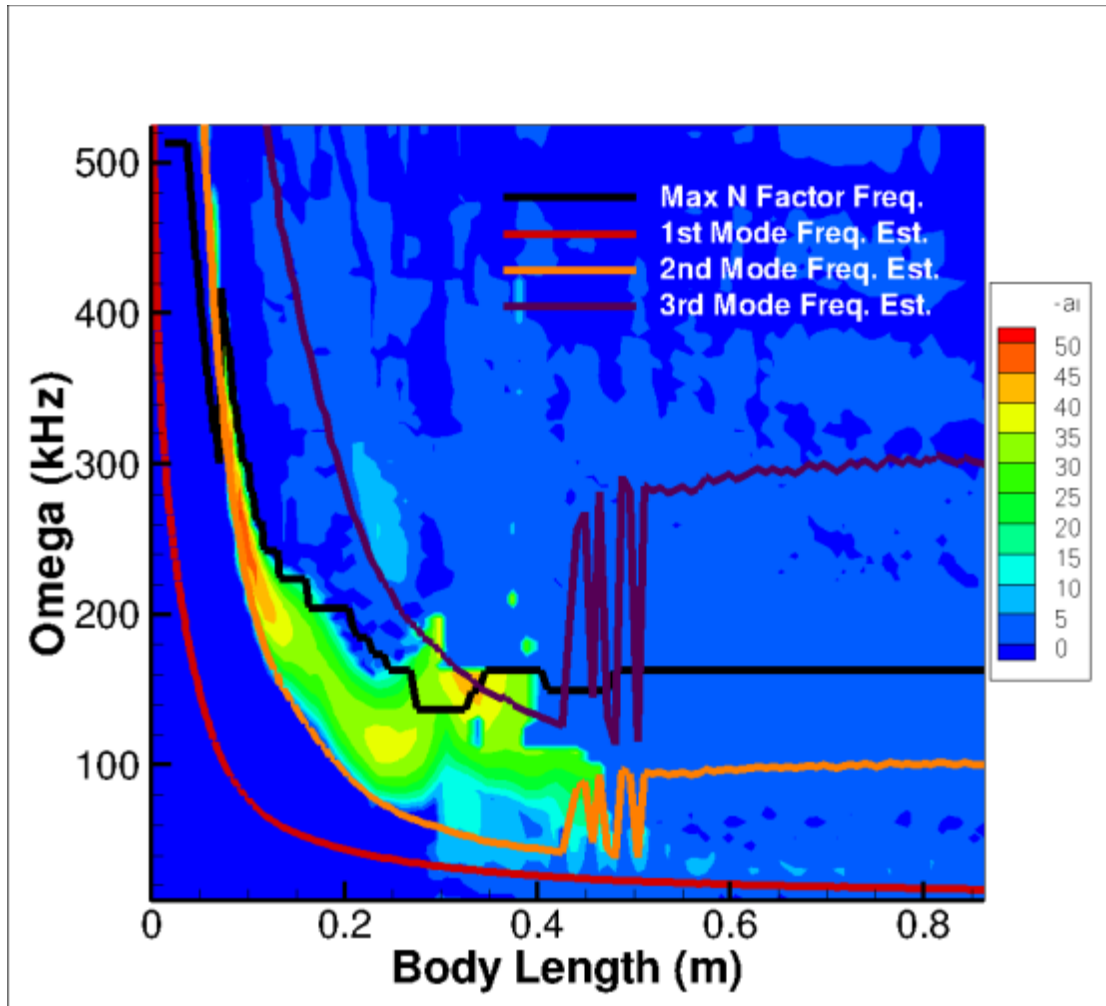
Figure 69 LST stability diagram for 21 km centerline plane. Max N factor frequencies (black), 1st Mode frequency estimate (orange), 2nd mode frequency estimate (red), 3rd mode frequency estimate (purple).
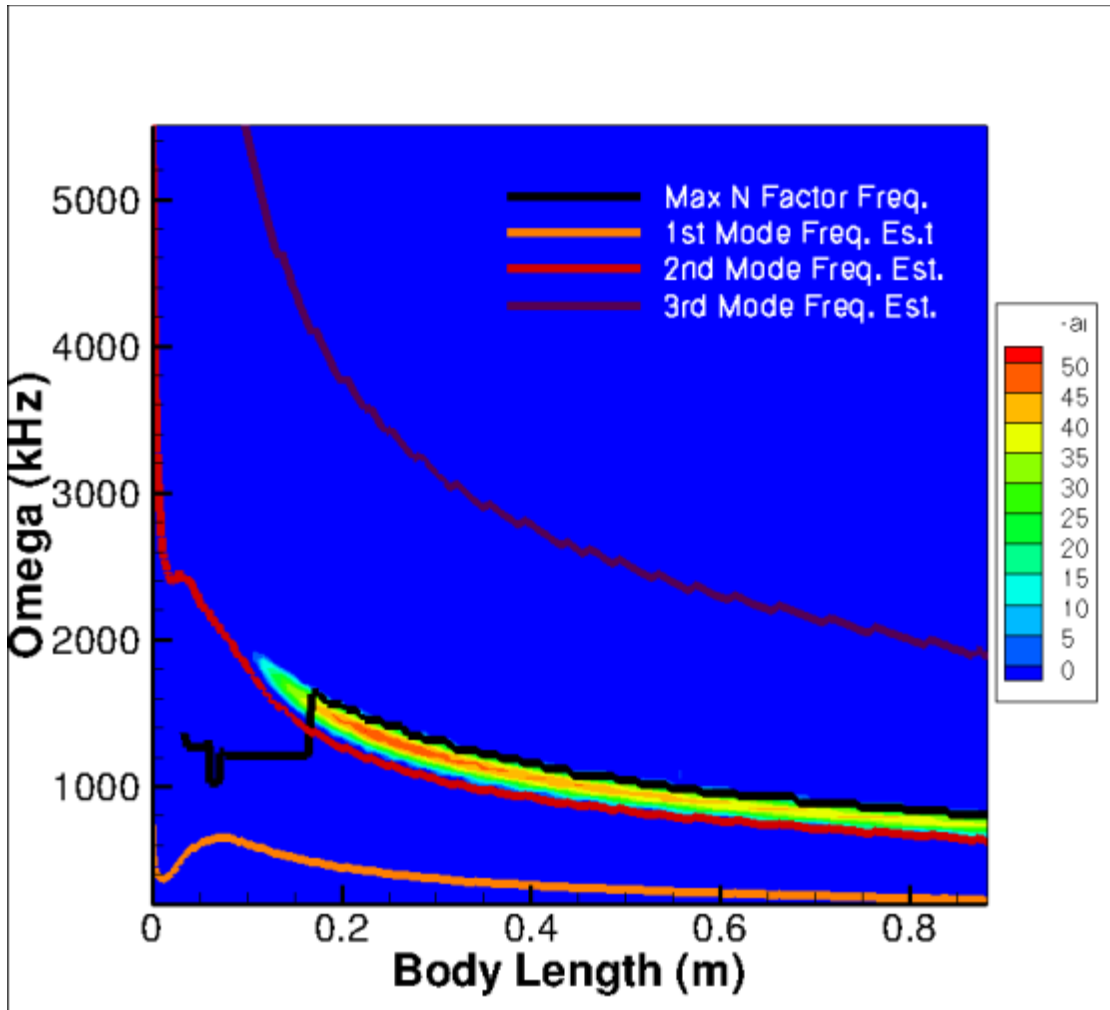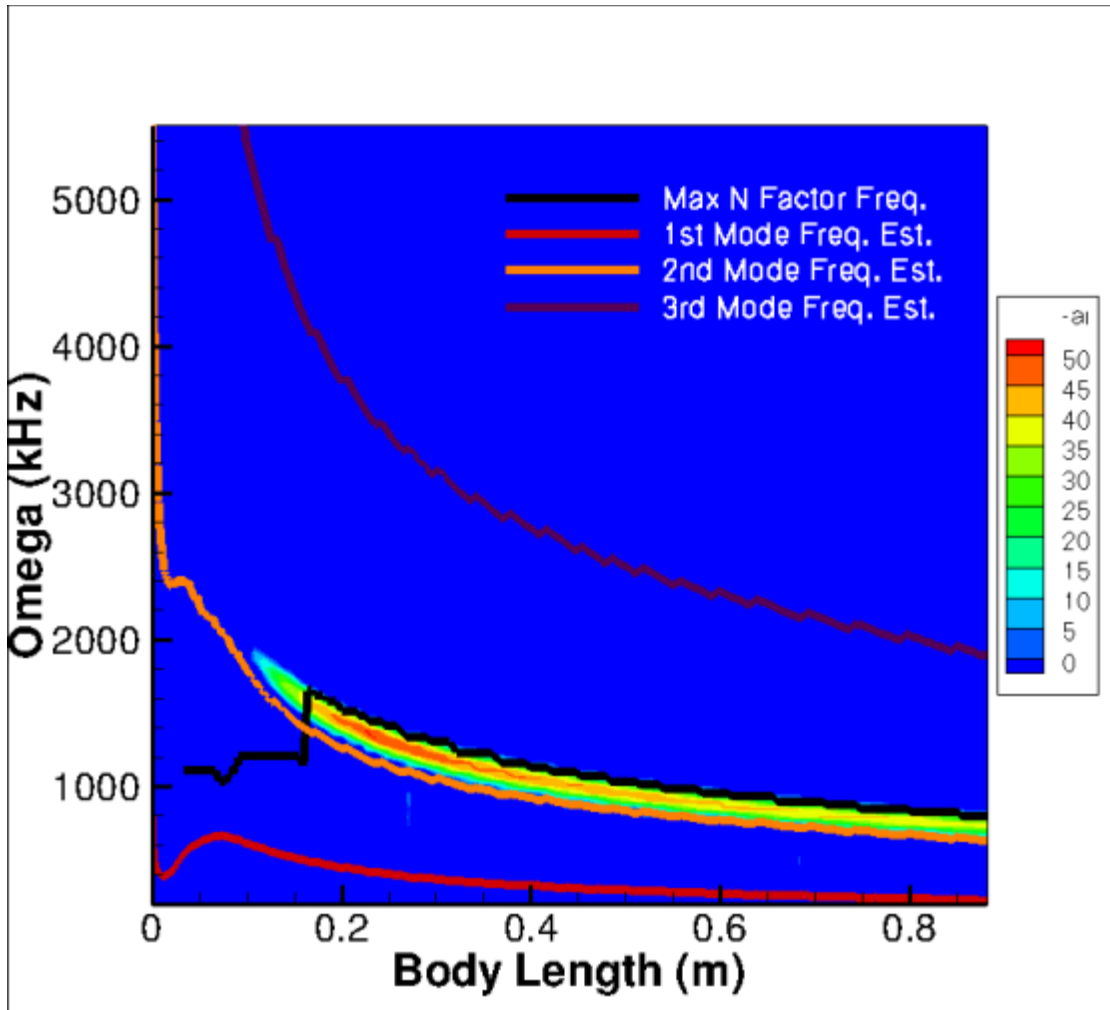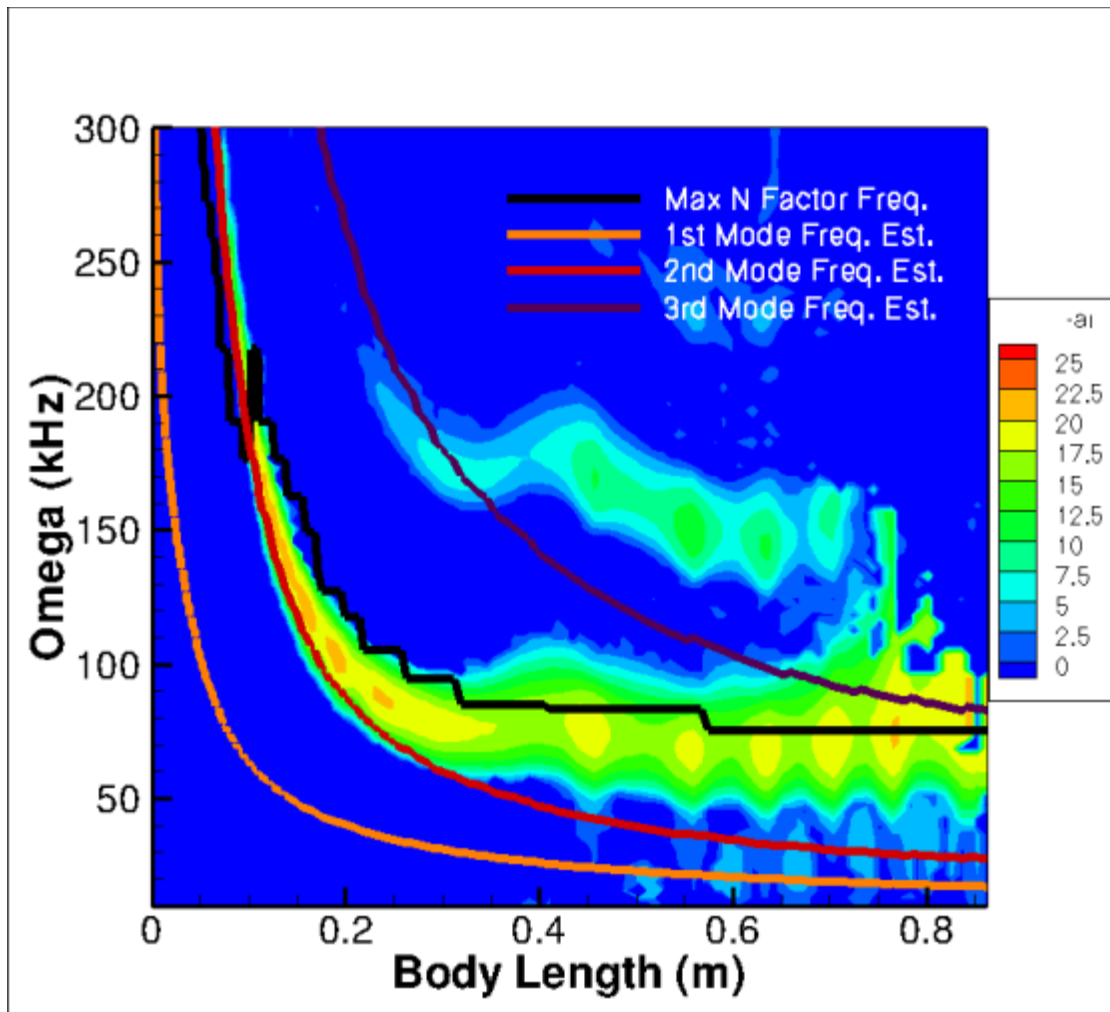
Figure 70 LST stability diagram for 25 km centerline plane. Max N factor frequencies (black), 1st Mode frequency estimate (orange), 2nd mode frequency estimate (red), 3rd mode frequency estimate (purple).
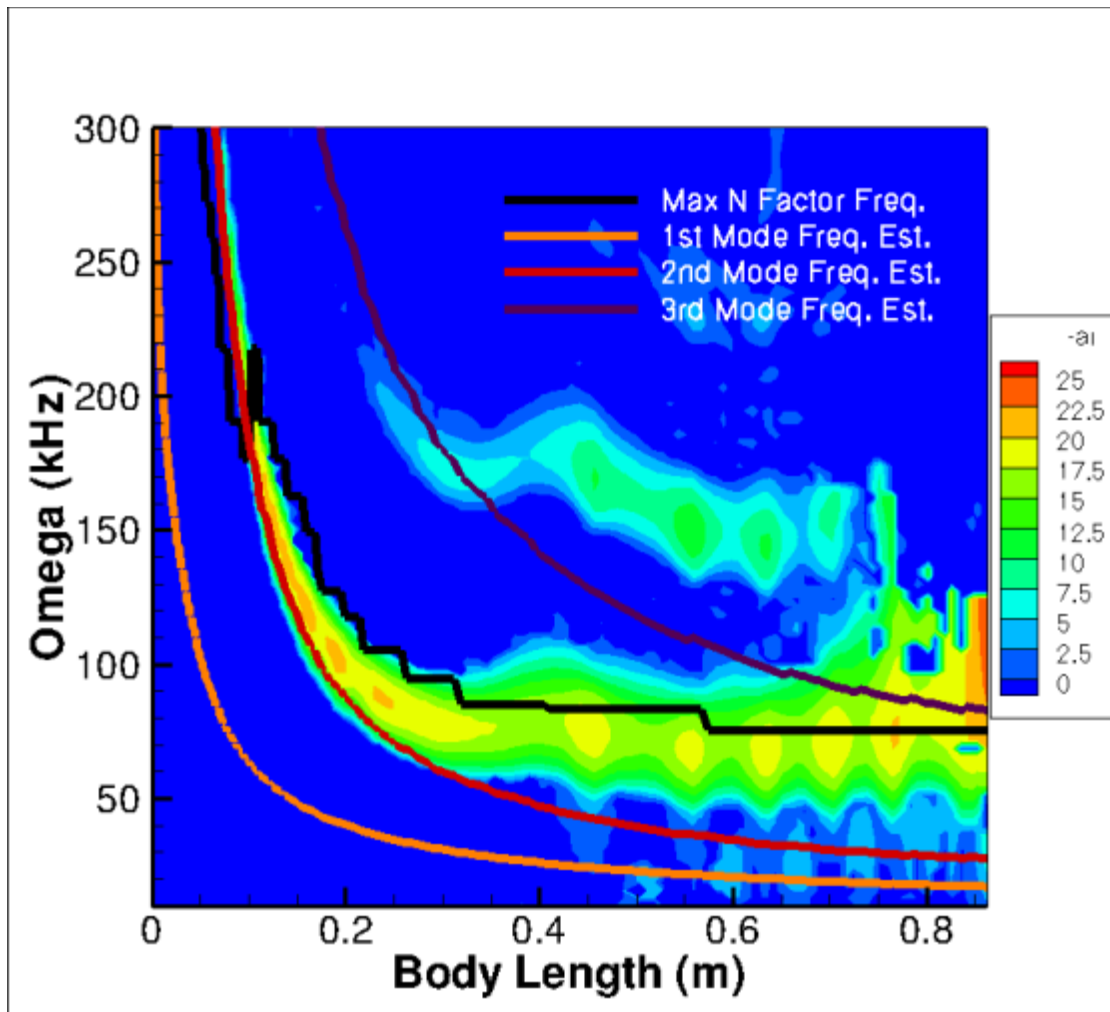
Figure 71 LST stability diagram for 28 km centerline plane. Max N factor frequencies (black), 1st Mode frequency estimate (orange), 2nd mode frequency estimate (red), 3rd mode frequency estimate (purple).
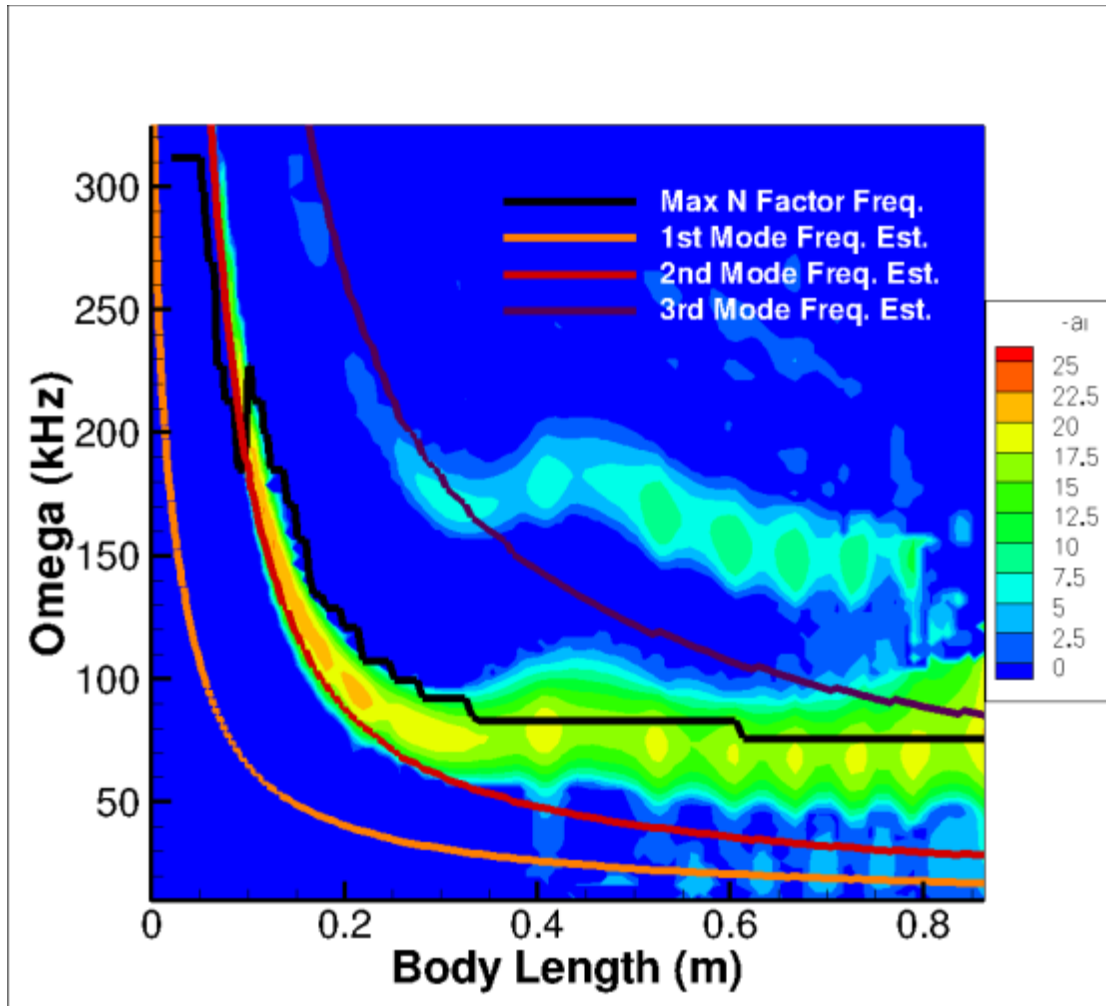
Figure 72 LST stability diagram for 33 km centerline plane. Max N factor frequencies (black), 1st Mode frequency estimate (orange), 2nd mode frequency estimate (red), 3rd mode frequency estimate (purple).
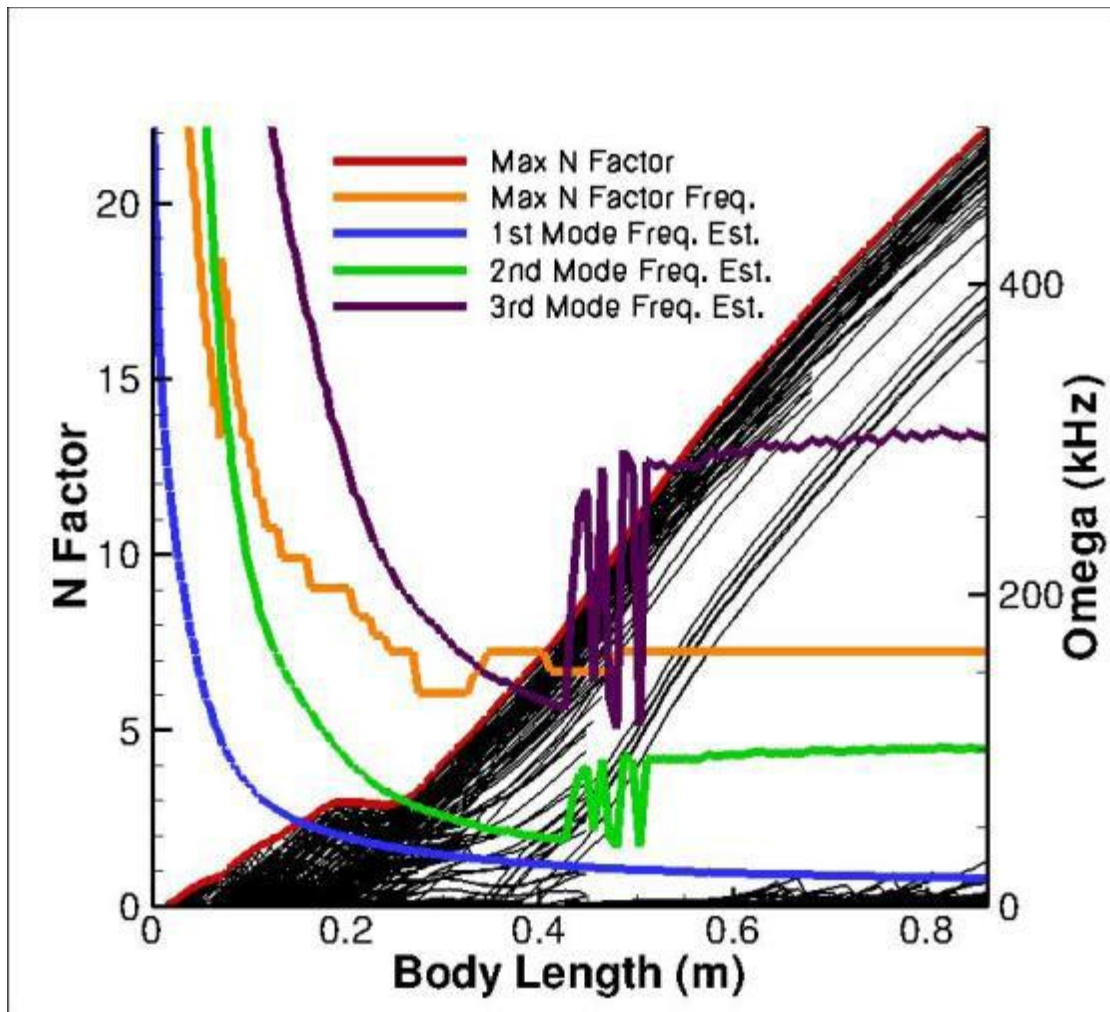
Figure 73 Boundary layer stability results for 21 km case centerline plane. N factors of calculated frequencies using STABL (black), Max N factor line (red), Max N factor frequencies (orange), 1st Mode frequency estimate (blue), 2nd mode frequency estimate (green), 3rd mode frequency estimate (purple).
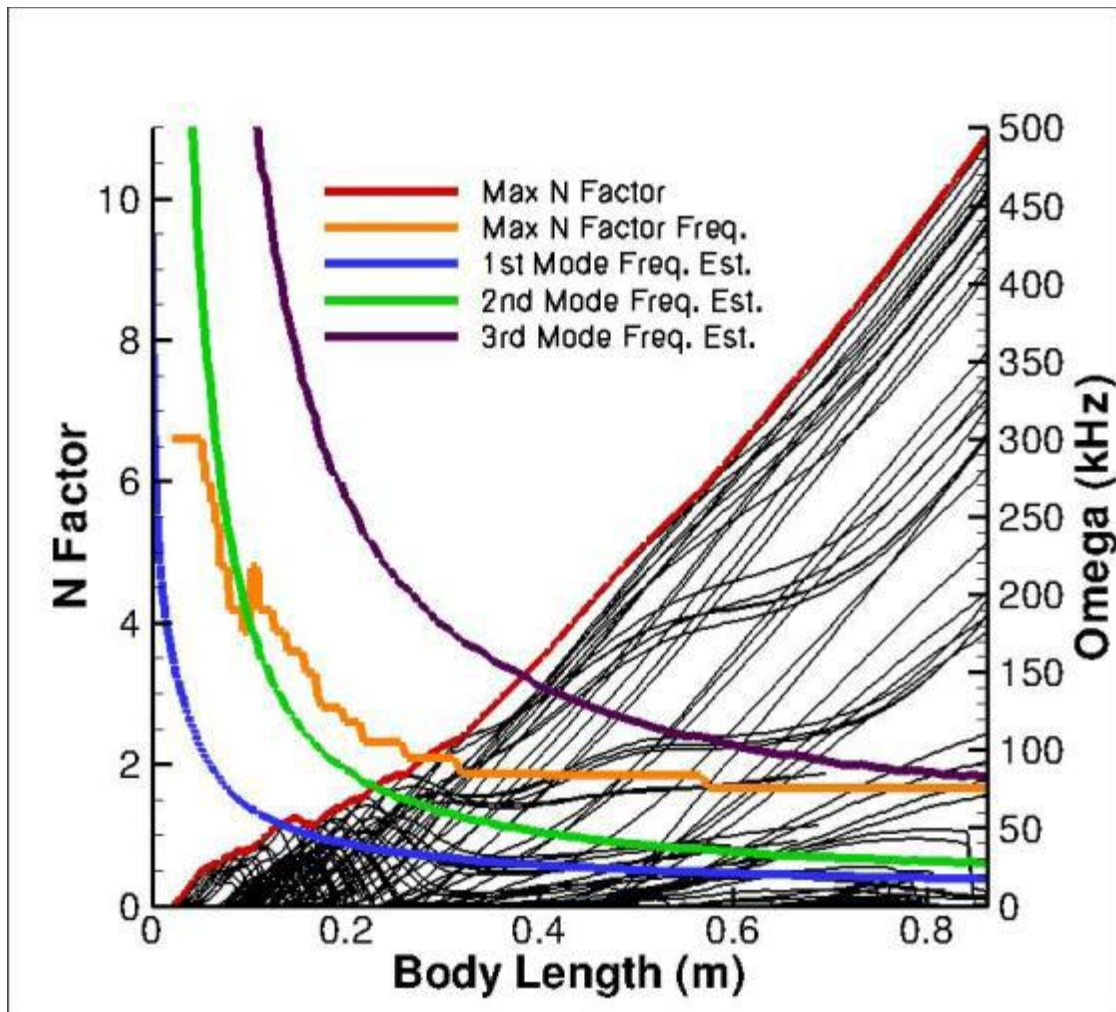
Figure 74 Boundary layer stability results for 25 km case centerline plane. N factors of calculated frequencies using STABL (black), Max N factor line (red), Max N factor frequencies (orange), 1st Mode frequency estimate (blue), 2nd mode frequency estimate (green), 3rd mode frequency estimate (purple).
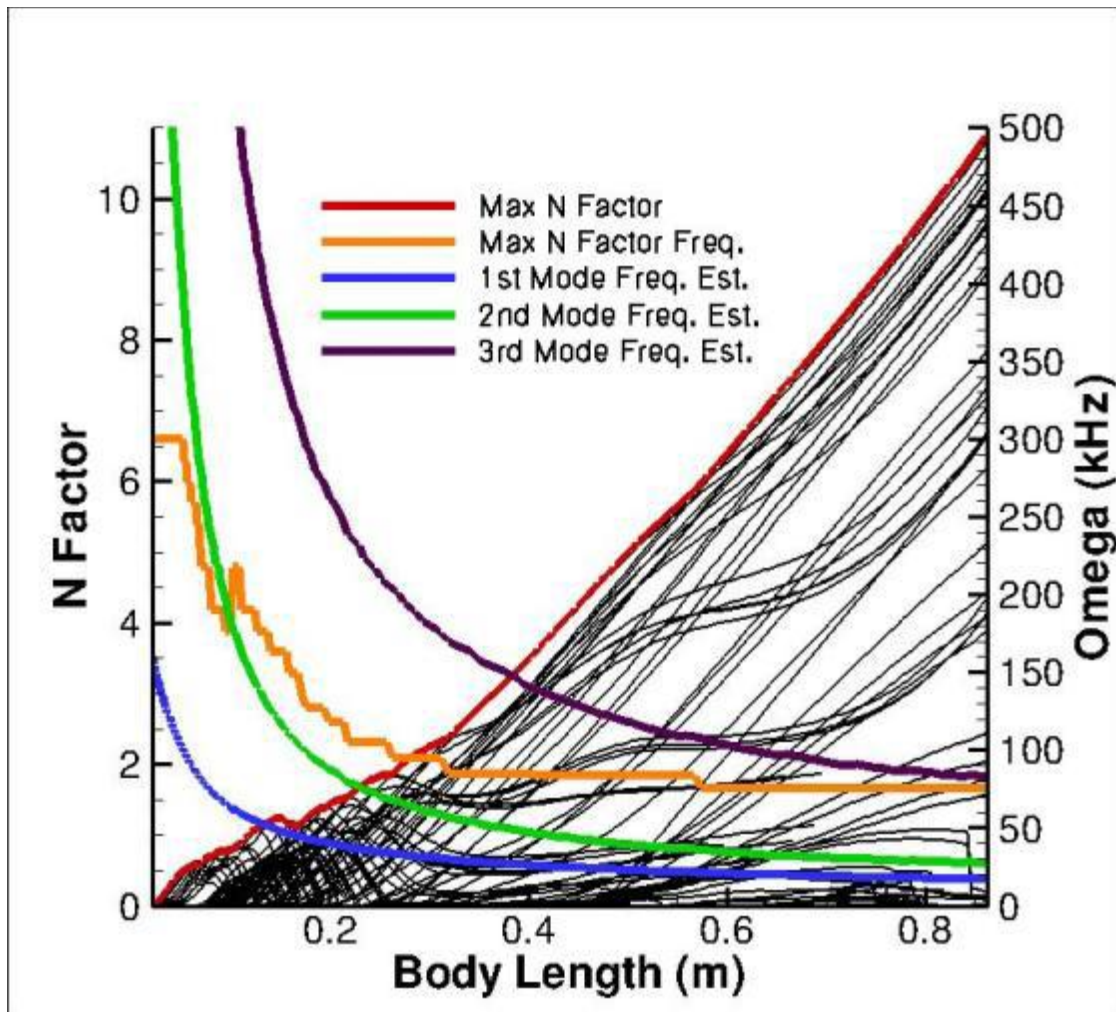
Figure 75 Boundary layer stability results for 28 km case centerline plane. N factors of calculated frequencies using STABL (black), Max N factor line (red), Max N factor frequencies (orange), 1st Mode frequency estimate (blue), 2nd mode frequency estimate (green), 3rd mode frequency estimate (purple).
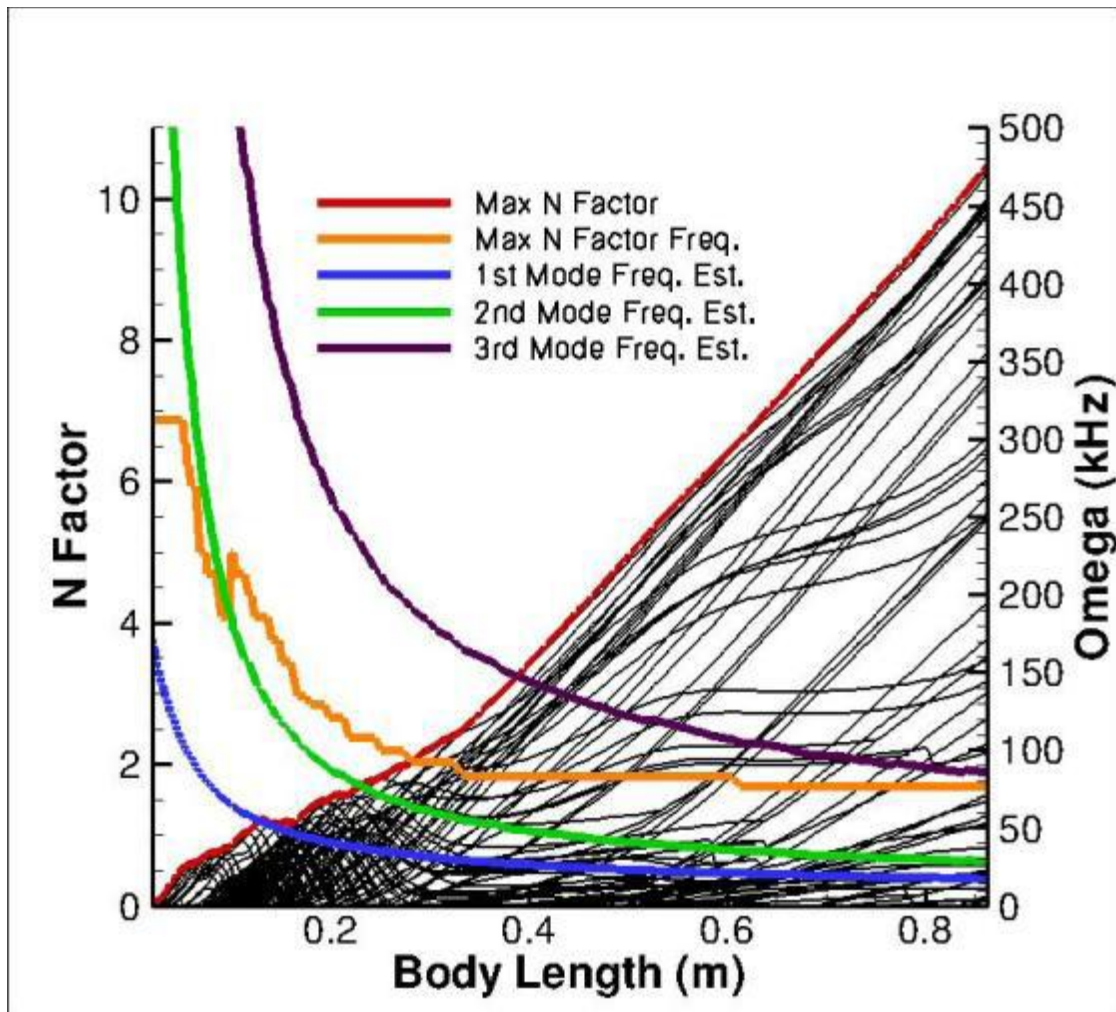
Figure 76 Boundary layer stability results for 33 km case centerline plane. N factors of calculated frequencies using STABL (black), Max N factor line (red), Max N factor frequencies (orange), 1st Mode frequency estimate (blue), 2nd mode frequency estimate (green), 3rd mode frequency estimate (purple).

Figure 78, Figure 78 and Figure 79 show boundary layer velocity profiles at select locations along the centerline profile for the 21km case. As we travel downstream we see that the upwelling flow on the centerline causes the boundary layer profile to have multiple infliction points. Here we see that as a result of the upwelling flow on the centerline, the boundary layer profile has multiple inflection points. Figure 80 shows a slice of the solution at the body length = 0.5 m location. The contour plot is of the flow density showing the structure of the roll up region. The vector plots are of the velocity. In the lower figure the perspective is looking down steam of the body. We can see the contribution of the velocity to flow inward to the centerline. As we approach the centerline the cross velocity decreases due to the symmetry condition and becomes lifted due to the formation of the vortex. The upper figure shows how the boundary layer profile is enhanced due to the uplifting. The boundary layer profile then shows a sharp increase to the edge velocity as it leaves the roll up region. The edge detection method indicates the boundary layer edge to occur at distances progressively out farther from the wall, as

Approved for public release; distribution unlimited.

expected. However, the second mode disturbance exists not between the wall and the edge, but between the wall and the relative sonic line in the boundary layer. The PSE-Chem code predicts that this relative sonic point moves closer to the wall in this region as a result of the changing boundary layer profile. While there is some oscillation in the prediction, indicated by the jumping frequency estimate, the oscillation in the estimate does not affect the stability results. When the relative sonic line moves closer to the wall, the frequency correspondingly increases. Referring back to Figure 76, the results of the PSE analysis show N factors which continue to grow as a result of continued amplification in the region from about 0.4 m to the end of the body, while the amplification in this region is not visible in the LST diagram of Figure 69. This may be the result of assumed values used in filters applied during the LST step to reduce the number of results from the eigenvalue analysis which are then passed to the PSE code for marching. Changing these filters might allow us to fill in the missing parts of the LST diagram. However, the PSE results are not restricted by the filters as once the disturbance is established it may evolve more freely on its own.

Figure 77 Boundary layer velocity profiles for 21 km case centerline plane, upstream

Approved for public release; distribution unlimited.

Figure 78 Boundary layer velocity profiles for 21 km case centerline plane, midbody

Figure 79 Boundary layer velocity profiles for 21 km case centerline plane, aft

Figure 80 Boundary layer velocity profiles and density contour for 21 km case for body length = 0.5 m plane. Upper figure is an iso-view showing velocity profile along roll up region. Lower figure shows velocity profile normal to body length plane slice.
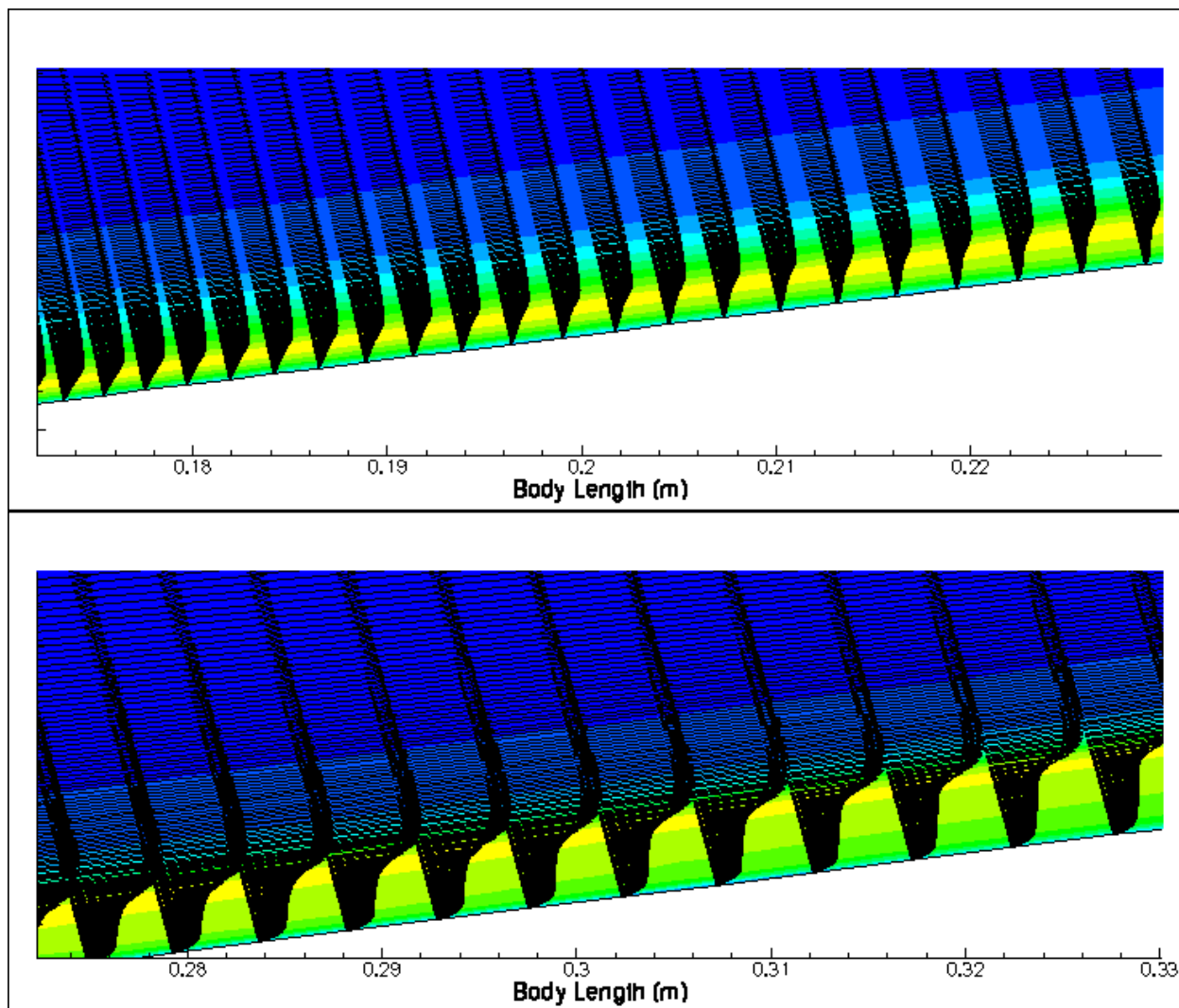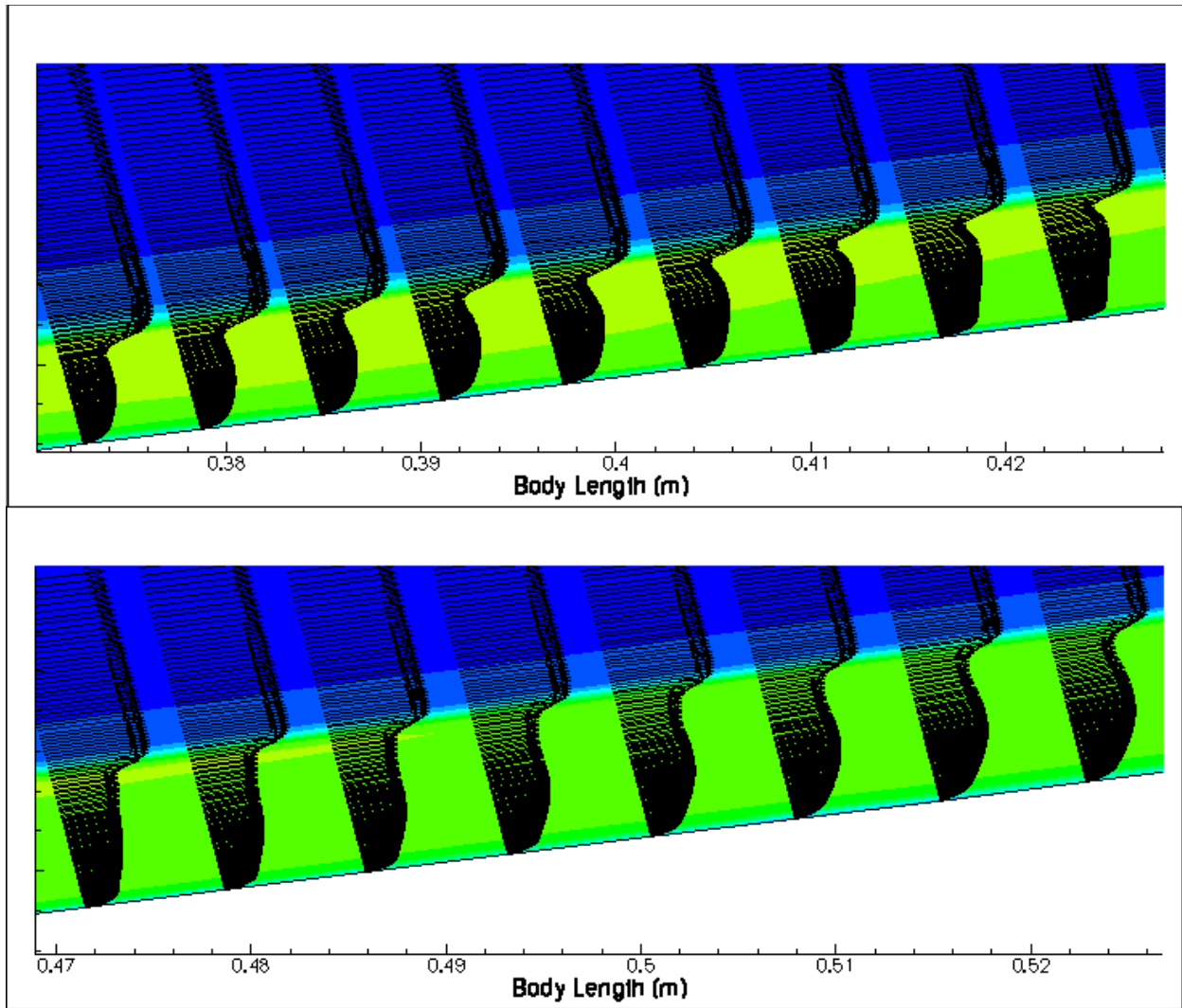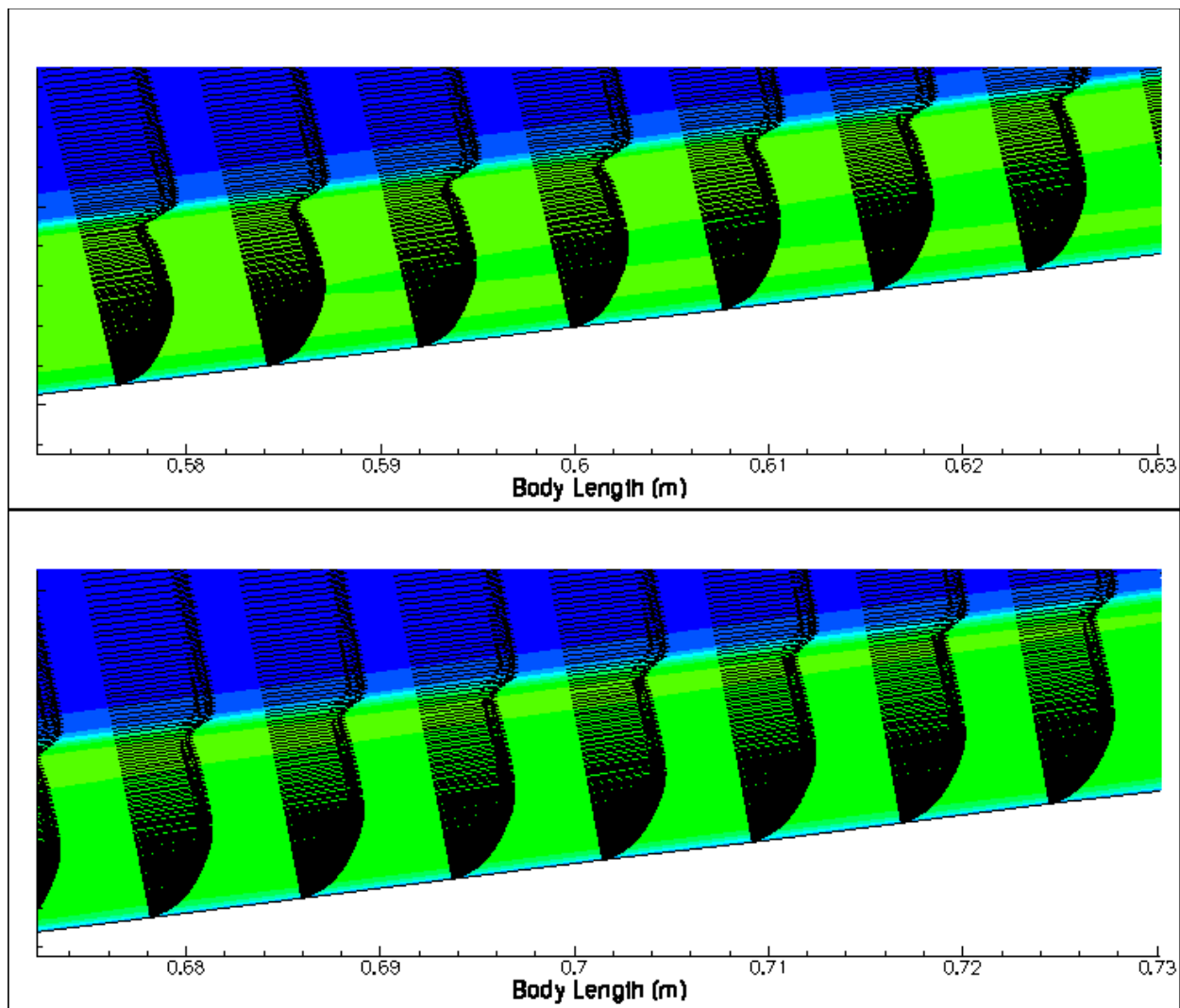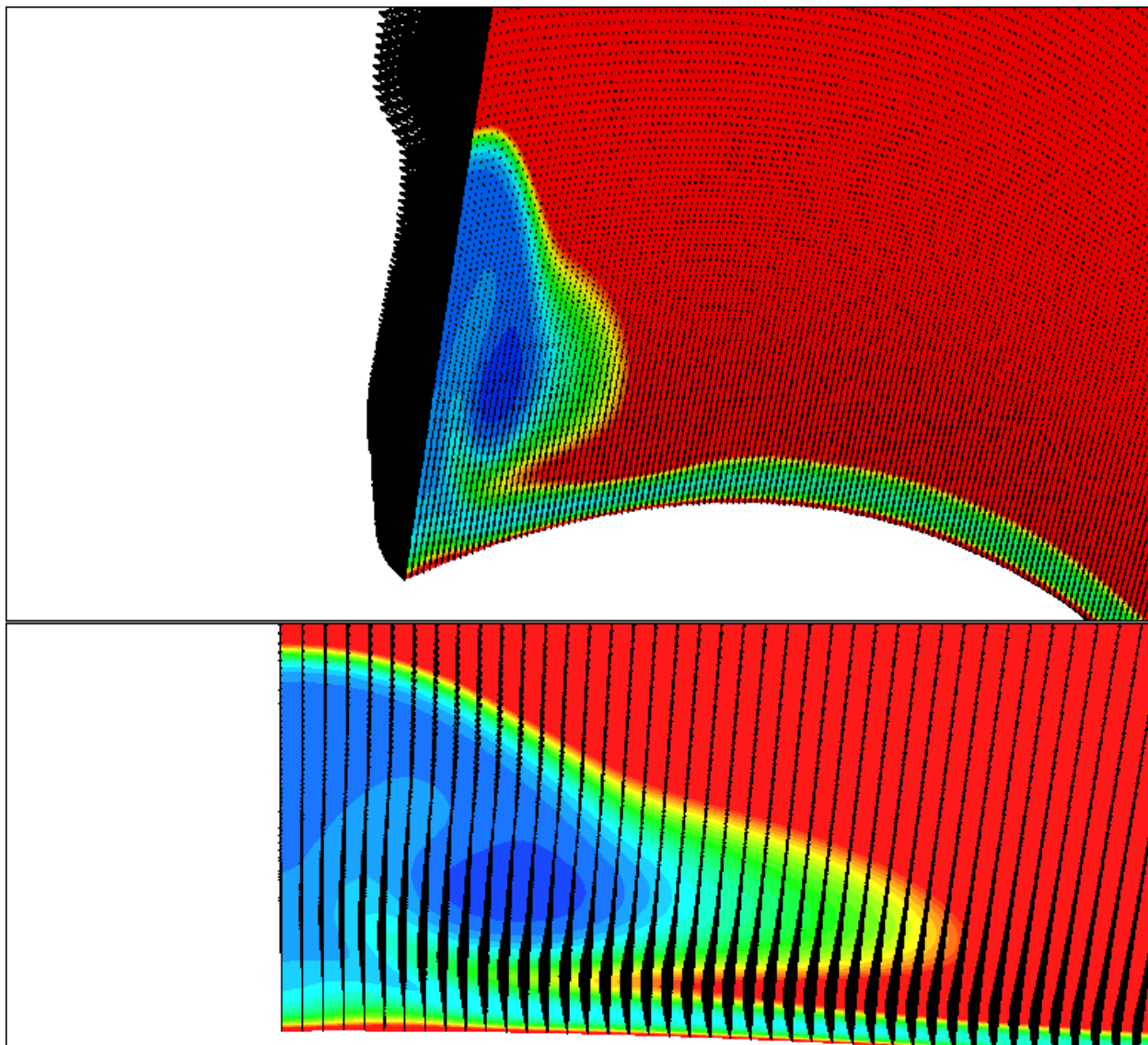
6. Conclusions

A scaled model of the HIFiRE Flight 5 vehicle was assessed in the Langley Research Center's 20-Inch Mach 6 Tunnel. The primary objectives of this test were to determine the boundary layer transition characteristics as well as the effectiveness of 2-D strip trips to simulate the joint between the nosecap and body of the vehicle and 3-D diamond shaped trips, to simulate the fasteners on a closeout panel that will be on one side of the flight vehicle. The data will be used to determine if the augmented heating associated with the fasteners and steps on the vehicle will contaminate the smooth side of the vehicle's data as well as for code calibration and for comparison to future testing in other facilities. In order to accomplish this, global heat transfer images were obtained for unit Reynolds numbers of 1.1×10^6/ft to 7.0×10^6/ft, angles of attack of -4 to +4 deg and side slip angles of -4 to +4 deg, which were conditions pertinent to the flight. Heating data demonstrated that the vehicle can be expected to exhibit natural boundary layer transition on the windside surface in the absence of boundary layer trips. The primary driver of the transition at 0 deg AoA appears to be cross-flow boundary layer transition, but windward centerline transition The HIFiRE-5 vehicle is designed to create transition in hypersonic flight with flowfields and pressure gradients characteristic of maneuvering hypersonic bodies.

The 2:1 elliptic cone configuration, lofted with the S30-Orion stack, is capable of providing adequate Reynolds number to achieve this goal. Although the payload is not axially symmetric and thus has different pitch-plane and yaw-plane aerodynamics, the entire vehicle is stable in both planes. The effect of leading-edge roughness on transition is well-correlated with the $\bar{R}^*$ correlation. This correlation is used to extrapolate wind tunnel data to full-scale flight conditions and obtain allowable leading-edge roughness tolerances. Leading-edge roughness tolerances are stringent but can be achieved using a clamshell design with a one-piece leading edge.

The flow around an elliptic cone is deceivingly complicated when it comes to transition analysis. The presence of complex physical features in the flow lead to instability growth that becomes inconsistent using 2D PSE analysis. For the leading edge of the vehicle, the PSE results show what seems to be second mode growth driving the increase of stabilities. Continuing work will be conducted using eigenvalue analysis to identify if the modes are in fact second mode. The centerline cases showed N factor growth that relied on the structure of the roll up region to define the boundary layer profile. The roll up region on the centerline continued to have the same height with increasing Reynolds number. The 21 km case showed a large difference between the other cases and produced growth rate at twice the rate. Using the current analysis tools, the exact reasons for this difference are not straight forward. Looking at the mean flow we could see the complex change in the boundary layer profile contributing to changes in the growth rate. A more detailed look will be taken to better understand these differences. In addition, a fully 3D PSE analysis will be conducted on the cases to better understand how crossflow interacts with the growth of instabilities.

List of Acronyms, Abbreviations, Symbols

L   reference length (in)

q   dynamic pressure (psi)

$\dot{q}$ heat transfer rate (BTU/ft^2-sec)

r   radius (in)

Re   unit Reynolds number (1/ft)

t   time (sec)

T   temperature (°F)

AoA = angle of attack

C_m = pitching moment

D = leading edge diameter

H   enthalpy (BTU/lb$_m$)

h = heat transfer coefficient, W/m^2/K

h   Heat transfer coefficient (lb$_m$/ft^2-sec) ($\dfrac{\dot{q}}{H - H_w}$)

h$_{ref}$ reference heat-transfer coefficient using Fay-Riddell

k = roughness height

L = reference length, 0.861 m

M = Mach number

Re = Reynolds number

$\overline{R}$ = Reynolds number based on reference length scale and spanwise velocity, $v_e \eta / v_e$

$\overline{R}^*$ = Reynolds number based on reference length scale η at reference temperature T^*, $v_e \eta^* / v_e^*$

s = chordwise coordinate along swept cylinder

T^* = reference temperature, Ref. 48

U = freestream velocity

u = chordwise velocity

v   = velocity tangential to attachment line on swept cylinder

x = coordinate along model long axis (Figure 4)

y = coordinate along model semi-minor axis (Figure 4)

z = coordinate along model semi-major axis (Figure 4)

ϕ = angular model coordinate (Figure 4)

$\delta*$ = boundary layer displacement thickness

θ = boundary layer momentum thickness

η = length scale, $\sqrt{v_e/(du_e/ds)}$

v = kinematic viscosity

Subscripts

∞ = freestream, upstream of the model bow shock

L = based on model reference length

e = boundary layer edge conditions

ref = reference value for heat transfer, Fay-Riddell heating for 0.64 mm radius hemisphere

Superscripts

$*$ = evaluated at reference temperature $T*$

References

[1] Dolvin, D. "Hypersonic International Flight Research and Experimentation (HIFiRE) Fundamental Science and Technology Development Strategy," AIAA Paper 2008-2581, April 2008.

[2] Dolvin, D. J., "Hypersonic International Flight Research and Experimentation Technology Development and Flight Certification Strategy," AIAA paper 2009-7228, October 2009.

[3] Kimmel, R. L., Adamczak, D., Gaitonde, D., Rougeux, A., Hayes, J. R., "HIFiRE-1 Boundary Layer Transition Experiment Design," AIAA paper 2007-0534, January 2007.

[4] Wadhams, T. P., MacLean, M. G., Holden, M.S., and Mundy, E., "Pre-Flight Ground Testing of the Full-Scale FRESH FX-1 at Fully Duplicated Flight Conditions," AIAA paper 2007-4488, June 2007.

[5] Johnson, H. B., Alba, C. R., Candler, G. V., MacLean, M., Wadhams, T, and Holden, M. "Boundary Layer Stability Analysis of the Hypersonic International Flight Research Transition Experiments," AIAA Journal of Spacecraft and Rockets, vol. 45, no. 2, March-April 2008.

[6] Holden, M. S., Wadhams, T. P., MacLean, M., "Experimental Studies in the LENS Supersonic and Hypersonic Tunnels for Hypervelocity Vehicle Performance and Code Validation," AIAA paper 2008-2505, April 2008.

[7] Kimmel, R. L., "Aerothermal Design for the HIFiRE-1 Flight Vehicle," AIAA paper 2008-4034, June 2008.

[8] Casper, K. M., Wheaton, B. M., Johnson, H. B., and Schneider, S. P., "Effect of Freestream Noise on Roughness-Induced Transition at Mach 6," AIAA paper 2008-4291 June 2008.

[9] Kimmel, R. L., "Roughness Considerations for the HIFiRE-1 Vehicle," AIAA Paper 2008-4293, June 2008.

[10] Alba, C. R., Johnson, H. B., Bartkowicz, M. D., Candler, G. V., and Berger, K. T. "Boundary-Layer Stability Calculations for the HIFiRE-1 Transition Experiment," *AIAA Journal of Spacecraft and Rockets*, vol. 45, no. 6, November-December 2008, pp. 1125-1133.

[11] Wadhams, T. P., Mundy, E., MacLean, M. G., and Holden, M. S., "Ground Test Studies of the HIFiRE-1 Transition Experiment Part1: Experimental Results," *AIAA Journal of Spacecraft and Rockets*, vol. 45, no. 6, November-December 2008, pp. 1134-1148.

[12] MacLean, M., Wadhams, T., Holden, M., and Johnson, H., "Ground Test Studies of the HIFiRE-1 Transition Experiment Part 2: Computational Analysis," *AIAA Journal of Spacecraft and Rockets*, vol. 45, no. 6, November-December 2008, pp. 1149-1164.

[13] Berger, K. T., Greene, F. A., Kimmel, R. L., Alba, C., and Johnson, H., "Erratum on Aerothermodynamic Testing and Boundary-Layer Trip Sizing of the HIFiRE Flight 1 Vehicle," AIAA Journal of Spacecraft and Rockets, vol. 46, no., 2, March-April, 2009, pp. 473-480.

[14] Adamczak, D., Alesi, H., Frost, M., "HIFiRE-1: Payload Design, Manufacture, Ground Test, and Lessons Learned," AIAA paper 2009-7294, October 2009.

[15] Reed, H. L., Kimmel, R. L., Schneider, S., Arnal, D., and Saric, W., "Drag Prediction and Transition in Hypersonic Flow," AGARD Paper C-15, Symposium on Sustained Hypersonic Flight, AGARD Conference on Future Aerospace Technology in the Service of the Alliance, 14-17 April 1997, Ecole Polytechnique, Palaiseau, France.

[16] Whitehead, A., "NASP Aerodynamics," AIAA paper 89-5013, July 1989.

[17] Kimmel, R. L., and Poggie, J., "Transition on an Elliptic Cone at Mach 8," American Society of Mechanical Engineers ASME FEDSM97-3111, June 1997.

[18] Kimmel, R. L., and Poggie, J., "Three-Dimensional Hypersonic Boundary Layer Stability and Transition," Air Force Research Laboratory Technical Report, WL-TR-97-3111, December 1997, Wright-Patterson Air Force Base, Ohio.

[19] Kimmel, R. L., and Poggie, J., Schwoerke, S. N., "Laminar-Turbulent Transition in a Mach 8 Elliptic Cone Flow," AIAA Journal, vol. 37, no. 9, Sep. 1999, pp. 1080-1087.

[20] Schmisseur, J. D., "Receptivity of the Boundary Layer on a Mach-4 Elliptic Cone to Laser-Generated Localized Freestream Perturbations," Doctoral Dissertation, Purdue University Aerospace Sciences Laboratory, December 1997.

[21] Holden, M., "Experimental Studies of Laminar, Transitional, and Turbulent Hypersonic Flows Over Elliptic Cones at Angle of Attack," Air Force Office of Scientific Research Technical Report AFRL-SR-BL-TR-98- 0142, Bolling Air Force Base, DC, 1998.

[22] Schmisseur, J. D., Schneider, S. P., and Collicott, S. H., "Receptivity of the Mach 4 Boundary Layer on an Elliptic Cone to Laser-Generated Localized Freestream Perturbations," AIAA paper 1998-0532, January 1998.

[23] Schmisseur, J. D., Schneider, S. P., and Collicott, S. H., "Response of the Mach 4 boundary layer on an elliptic cone to laser-generated freestream perturbations," AIAA paper 1999-0410, January 1999.

[24] Lyttle, I. J., and Reed, H. L., "Use of Transition Correlations for Three-Dimensional Boundary Layers Within Hypersonic Flows," AIAA-95-2293, June 1995.

[25] Kimmel, R. L., Klein, M. A., and Schwoerke, S. N., "Three-Dimensional Hypersonic Laminar Boundary Layer Computations for Transition Experiment Design," *AIAA Journal of Spacecraft and Rockets*, vol. 34, no. 4, July- August 1997

[26] Kimmel, R. L., "Aspects of Hypersonic Boundary Layer Transition Control," AIAA Paper 2003-0772, January 2003.

[27] Stetson, K. F., Thompson, E. R., Donaldson, J. C., and Siler, L. G., "Laminar Boundary Layer StabilityExperiments on a Cone at Mach 8, Part 5: Tests with a Cooled Model," AIAA 89-1895, June 1989.

[28] Malik, M. R., Li, F., Choudhari, M., "Analysis of Crossflow Transition Flight Experiment aboard the Pegasus Launch Vehicle," AIAA paper 2007-4487, June 2007.

[29] Palmerio, A. F.; Peres da Silva, J. P. C.; Turner, P.; Jung, W., "The development of the VSB-30 sounding rocket vehicle," in 16th ESA Symposium on European Rocket and Balloon Programmes and Related Research, 2 - 5 June 2003. Ed.: Barbara Warmbein. ESA SP-530, Noordwijk: ESA Publications Division, 2003, p. 137 – 140.

[30] "NASA Sounding Rocket Program Handbook," 810-HB-SRP, Sounding Rockets Program Office, Suborbital & Special Orbital Projects Directorate, Goddard Space Flight Center, Wallops Island Flight Facility, June 2005.

[31] Odam, J., Paull, A., Alesi, H., Hunt, D., Paull, R., Pietsch, R., "HIFiRE 0 Flight Test Data," AIAA paper 2009-7293, October 2009.

[32] McDonnell Douglas Astronautics Company, "The USAF Stability and Control Digital Datcom Volume II, Implementation of Datcom Methods," Air Force Flight Dynamics Laboratory Technical Report AFFDL-TR-79-3032, Wright-Patterson Air Force Base, Ohio, April 1979.

[33] Auman, L., Doyle, J., Rosema, C., Underwood, M., and Blake, W., "Missile Datcom User's Manual – 2008 Revision," Air Force Research Laboratory AFRL-RB-WP-TR-2009-3015, Wright-Patterson Air Force Base, Ohio, August 2008

[34] Aftosmis, M. J., Berger, M. J., and Alonso, J. J., "Applications of a Cartesian Mesh Boundary-Layer Approach for Complex Configurations," AIAA paper 2006-0652, January 2006.

[35] Engel, C. D., and Praharaj, S. C., "MINIVER Upgrade for the AVID System. Volume I: LANMIN User's Manual," NASA Contractor Report 172212, August 1983.

[36] Carter, M. L., Kuruvila, G., Woo, Y., Lau, K. Y., and Bowcutt, K. G., "Hypersonic Engineering Aerothermodynamic Trajectory Tool Kit (Heat-TK)," Air Force Research Laboratory technical report AFRL-VA-WP-TR 2005-3120, Wright-Patterson Air Force Base Ohio, January 2005

[37] Horvath, T. J., et al, "Shuttle Damage/Repair from the Perspective of Hypersonic Boundary Layer Transition - Experimental Results," AIAA 2006-2919, June 2006

[38] Micol, J. R., "Langley aerothermodynamics facilities complex: enhancements and testing capabilities," AIAA Paper 98-0147, Jan 1998.

[39] Buck, G. M., "Automated thermal mapping techniques using chromatic image analysis," NASA TM 101554, April 1989.

[40] Merski, N. R., "Reduction and analysis of phosphor thermography data with iheat software package," AIAA-98-0712, Jan 1998.

[41] Merski, N. R., "Global aeroheating wind-tunnel measurements using improved two-color phosphor thermography model," *Journal of Spacecraft and Rockets*, Vol., 36, No., 2, 1998, pp. 160-170.

[42] Fay, J. A., and Riddell, F. R., "Theory of Stagnation Point Heat Transfer in Dissociated Air," Journal of Aeronautical Sciences, Vol. 25, No. 2, 1958, pp. 73-85.

[43] Choudhari, M., Chang, C., Li, F., McGinley, C., Berger, K., Candler, G., Kimmel, R., "Transition Analysis forthe HIFiRE-5 Vehicle," AIAA-2009-4056, June 2009.

[44] Holden, M. S., Wadhams, T. P., MacLean, M. Mundy, E., "Review of Studies of Boundary Layer Transition in Hypersonic Flows Over Axisymmetric and Elliptic Cones Conducted in the CUBRC Shock Tunnels, AIAA paper 2009-0782, January 2009.

[45] Horvath, T. J., Berry, S. A., Hollis, B. R., Liechty, D. S., Hamilton, H. H., Merski, N. R., "X-33 Experimental Aeroheating at Mach 6 Using Phosphor Thermography," *AIAA Journal of Spacecraft and Rockets*, vol. 38, no. 5, 2001, pp. 634-645

[46] Schneider, S. P., "Effects of High-Speed Tunnel Noise on Laminar-Turbulent Transition," *Journal of Spacecraft and Rockets*, vol. 38, no. 3, May-June 2001, pp. 323-333.

[47] Berger, K. T., Rufer, S.J., Kimmel, R., and Adamczak, D., "Aerothermodynamic Characteristics of Boundary Layer Transition and Trip Effectiveness of the HIFiRE Flight 5 Vehicle," AIAA paper 2009-4055, June 2009.

[48] Poll, D. I. A., "The Development of Intermittent Turbulence on a Swept Attachment Line Including the Effects of Compressibility*," The Aeronautical Quarterly*, vol. XXXIV, Feb. 83, pp. 1-23.

[49] Creel, T. R., Beckwith, I. E., and Chen, F. J., "Transition on Swept Leading Edges at Mach 3.5," AIAA J. Aircraft, vol. 24, no. 10, Oct. 1987, pp. 710-717.

[50] Schneider, S. P., "Effects of Roughness on Hypersonic Boundary Layer Transition," *AIAA Journal of Spacecraft and Rockets*, vol. 45, no. 2, March-April 2008.

[51] Murakami, A., Stanewsky, E., and Krogman, P., "Boundary Layer Transition on Swept Cylinders at Hypersonic Speeds," *AIAA Journal*, vol. 34, no. 4, April 1996, pp. 649-654.

[52] Benard, E., Gaillard, L., Alziary de Roquefort, A., "Influence of roughness on attachment line boundary-layer transition in hypersonic flow," Experiments in Fluids, vol. 22, no. 4, February 1997, pp. 286-291.

[53] Choudhari, M., Chang, C. L., Jentink, T., Li, F., Berger, K., Candler, G., Kimmel, R., "Transition Analysis for the HIFiRE-5 Vehicle," AIAA-2009-4056, June 2009.

[54] Johnson, H., Candler, G., "Hypersonic Boundary Layer Stability Analysis Using PSE-Chem," AIAA-2005-5023.

[55] Nompelis, I., Drayna, T., Candler, G., "A Parallel Unstructured Implicit Solver for Hypersonic Reacting Flow Simulation," AIAA-2005-4867.

[56] Park, C., Nonequilibrium Hypersonic Aerothermodynamics, John Wiley and Sons, NY, 1990.

[57] Blottner, F. G., Johnson, M., and Ellis, M., "Chemically Reacting Viscous Flow Program for Multi-component Gas Mixtures," Sandia Laboratories Report No. SC-RR-70-754, Albuquerque, New Mexico, 1971.